Optical Properties of Nd-Doped Si-based thin films : towards an optical amplifier

Chuan-Hui Liang

To cite this version:

Chuan-Hui Liang. Optical Properties of Nd-Doped Si-based thin films : towards an optical amplifier. Materials Science [cond-mat.mtrl-sci]. Université de Caen, 2013. English. NNT : . tel-00926053

HAL Id: tel-00926053
https://theses.hal.science/tel-00926053

Submitted on 9 Jan 2014

Université de Caen Basse-Normandie

Ecole doctorale *SIMEM*

Thèse de doctorat

présentée et soutenue le : *28/11/2013*

par

Chuan-hui LIANG

pour obtenir le

Doctorat de l'Université de Caen Basse-Normandie

Spécialité : *Milieux denses, matériaux et composants*

Propriétés optiques des films minces à base de Si dopé Nd :

Vers un amplificateur optique

Directeur de thèse : *Fabrice Gourbilleau*

Jury

M. Bruno Masenelli	Professeur des Universités, INSA Lyon-INL (Villeurbanne) (*rapporteur*)**.**
M. Hervé Rinnert	Professeur des Universités, Université de Lorraine- Institut Jean Lamour (Nancy) (*rapporteur*)
Mme. Marie-Paule Besland	Directrice de Recherche CNRS, IMN (Nantes) (*Examinatrice*)
M. Julien Cardin	Ingénieur de Recherche, CIMAP (Caen) (co-*directeur de thèse*)
M. Fabrice Gourbilleau	Directeur de Recherche CNRS, CIMAP (Caen) (*directeur de thèse*)

Contents

List of Figures

Chapter 1

Chapter 2

Chapter 3

Chapter 4

Chapter 5

List of Tables

List of Abbreviations

- AD - As-deposited
- ASS - Atomic Scale Sensitizers
- BEMA - Bruggeman Effective Medium Approximation
- CA - Classical Annealing
- CCD -
- c-Si - Crystalline Silicon
- DC - Direct Current
- EDWA - Erbium-doped Waveguide Amplifier
- EMA - Effective Medium Approximation
- FG - Forming Gas
- FTIR - Fourier Transform Infrared Spectroscopy
- FWHM - Full Width at Half Maximum
- LCs - Luminescence Centers
- LEDs - Light Emitting Diodes
- LDOS - Local Density of States
- LO - Longitudinal Optical Mode
- MBE - Molecular Beam Epitaxy
- NBOHCs - Non-Bridging Oxygen Hole Centers
- ODCs - Oxygen-Deficient Centers
- OPO - Optical Parametric Oscillator
- PECVD - Plasma Enhanced Chemical Vapor Deposition
- PL - Photoluminescence
- PLE - Photoluminescence Excitation
- p_{pls} - Plasma Pressure
- QCE - Quantum Confinement Effect
- RBS - Rutherford Backscattering Spectroscopy
- RE - Rare Earth
- RF - Radio Frequency
- RFP_{SiO2} - RF power density applied onto SiO_2 cathode
- RFP_{Si} - RF power density applied onto Si cathode
- RFP_{Nd2O3} - RF power density applied onto Nd_2O_3 cathode

- r_H - Hydrogen rate
- $\mathrm{r_N}$ - Nitrogen Rate
- RTA - Rapid Thermal Annealing
- SE - Signal Enhancement
- Si-nps - Silicon nanoparticles
- SiN_x - Silicon rich Silicon Nitride
- SiO_x - Silicon rich Silicon Oxide
- SRSN - Silicon rich Silicon Nitride
- SRSO - Silicon rich Silicon Oxide
- $\mathrm{T_A}$ - Annealing Temperature
- $\mathrm{t_A}$ - Annealing Time
- $\mathrm{T_s}$ - Substrate Temperature
- TEM - Transmission Electron Microscopy
- UV - Ultraviolet

General Introduction

(a) State of the art

The last decades of the 20th century witnessed the emergence of Information Era occurring of data exchange across the world. Such phenomenon has significantly promoted the industrial development of information technology. This “digital explosion” is the result of the invention of internet and computer, whose development is closely connected to the microelectronic technology. Since several decades, the microelectronic industry is striving for further reduction in the size of transistor, following the famous Moore’s law. However, these highly miniaturized devices are now facing the so called electronic bottleneck. Because the electronics have significant challenges to meet the increasing requirements on information transmission of high speeds, large capability, and low noise. The decreasing of feature sizes and increasing clock frequencies among inter-chips or extra-chips would beat the physical limitation of electrical signaling[1]. Moreover, the dissipation of electric power limits the efficiency of complementary metal-oxide semiconductors microelectronics.

To overcome these issues, one viable solution lies in the monolithic integration of photonics with semiconductor microelectronics to ensure effective and fast connection of inter-chips or extra-chips. Integrated optics is capable of signal modulating, wavelength multiplexing, switching and amplification. The photonics could bring new functionalities to electronic components such as a higher bandwidth due to higher frequency provide by the carrier optical wave signal, and immunity to electromagnetic perturbations.

One of the critical issues to achieve complete integrated optic system is the lack of integrated light sources. Si-based light source would be one of the most promising candidates for that purpose. Since the Si-based optoelectronic circuit is compatible with CMOS technology, providing the possibility to achieve a compact Si-based device combining the two “electronic and photonic” functions.

In the last 20 years, the research community has taken great interest in the rare earth (RE) ions and Si nanoparticles (Si-nps) coupled system, which is a promising candidate for the achievement integrated Si-based light source. Since the RE ions are benefited from the higher absorption cross section of Si-nps (about 10^{-16} cm^2[2] with respect to 10^{-20} cm^2 for RE ions in SiO_2[3]). In this regard, the most addressed is Er^{3+} ion due to its attractive application for optical communication[4] in C band. However, evidence of the achievement of net gain from Si-nps : Er^{3+} ions in such system has been reported only once[5]. This is mainly due to the three-level nature of the Er^{3+} ions which lead to a threshold pump power to get population inversion. The possibility of re-absorption of emitted photon by the neighboring Er^{3+} ions is also a potential drawback of using such ions. Since the wide applications for medicine and communication technologies (O band), the Nd^{3+} ion has aroused great interest. Contrarily to the Er^{3+} ion, Nd^{3+} ion emits in four-level configuration (1.06 µm) and does not have a threshold pump power for inversing population and has a weak probability of re-absorption of the emitted light at 1.06 µm. Consequently, net gain seems to be achievable with Nd^{3+} ion in an easier manner than with Er^{3+} ion.

However, there are some limitations to achieve sufficient gain of Nd^{3+} luminescence. The Si-nps with small size are favorable to effectively sensitize the Nd^{3+} ions, while a high Si excess incorporated would leads to grow large Si-nps. The rather low solubility of Nd within silica[6] leading to the formation of Nd_2O_3 cluster at the expense of Nd^{3+} density is another limiting factor. Such cluster may favor energy migration and cross relaxation leading to a quench of Nd^{3+} emission. As a result, Debieu et al.[7] have found that the Nd^{3+} PL decreases dramatically when Nd content increases from 0.08 to 0.27 at.%. Furthermore, the Nd^{3+} PL decay time is in the order of µs, and may decrease with increasing Si atom excess. Nevertheless, the improvement of the layers microstructure and of Si-nps and Nd^{3+} ions densities may result in a larger Nd^{3+} population inversion and a higher gain.

(b) Major objectives of this thesis

For an achievement of Si-based Nd^{3+} laser, this thesis focuses on four major issues which are:

Material growth technique: Both classical and reactive co-sputtering approaches are concerned for the layers grown in our laboratory. One main factor governing the material and device properties is the layer composition, which is closely dependant on the deposition conditions. Therefore, the first major objective of this thesis is to find a suitable deposition approach and then to optimize the parameters (such as Si and or Nd_2O_3 cathode power density) to fabricate two typical systems Nd-doped Si-rich silicon oxide (Nd-SRSO) and silicon nitride (Nd-SRSN).

Annealing treatments: Annealing is necessary to improve the quality of the host matrix and form the sensitizers. But a too high temperature and/or too long duration are supposed to result in formation of RE ions clusters as well as overgrowth of Si-nps, which are detrimental to the sample emission intensity. Therefore, the second major objective of this work is to optimize annealing conditions (temperature, duration, and gas atmosphere) involving the classical annealing and rapid thermal annealing.

Material properties: Photoluminescence (PL) measurements help one to select the optimal sample which provides the most possibility to obtain net gain. Achieving significant Nd^{3+} PL is a challenge, and understanding the mechanisms of energy transfer from sensitizers becomes the next important challenge. Therefore, the third major objective of this work is to analyze the microstructural properties of the materials, to correlate such microstructure with the PL properties, and to understand the nature of sensitizers towards Nd^{3+} ions in SRSO and SRSN host matrices.

Device properties: The optimized films were used to fabricate optical waveguides. The possibility of achievement of net gain in such structure would have a large impact towards the realization of a Si-based Nd^{3+} laser. Therefore, the last major objective is to carry out the investigation of waveguide properties such as losses, guided PL and the signal enhancement measurement.

(c) Sketch of this thesis

There are five chapters in this thesis.

Chapter 1 describes the current research state of Si nanostructure and its coupling with RE ions (Er^{3+} and Nd^{3+} ions). This chapter presents the samples fabrication and the optical properties concerning two kinds of host matrices SRSO and SRSN. We focus on the correlations between film composition, microstructure and PL properties.

Chapter 2 shows the principle and the working method of various experimental techniques employed in this thesis for the layer deposition and characterization.

Chapter 3 focuses on the optimization process for Nd-SRSO films. We detail the effects of Si excess and Nd content on structural and optical properties of samples deposited by reactive and classical co-sputtering approaches. The best sample obtained from the latter approach is used to study the influence of annealing conditions. Both classical annealing and rapid thermal annealing are employed with monitoring the temperature, duration, and gas atmosphere. The structural and optical properties of samples are analyzed. With achieving the remarkable Nd^{3+} PL, the energy transfer mechanism is investigated by comparison to the PL properties of undoped SRSO film.

Chapter 4 is devoted to the study on Nd-SRSN films deposited only by reactive co-sputtering method. The incorporated Si excess is controlled by the nitrogen ratio to the argon gas used in the plasma, while Nd content by the power density applied on Nd_2O_3 cathode. We correlate the films optical properties to the sample composition. The optimal film receives classical annealing and rapid thermal annealing with various temperatures and durations. Then the annealed samples are analyzed for structural and optical properties. The PL excitation measurements are performed to study the energy transfer mechanism.

Chapter 5 presents the fabrication of waveguide devices and investigation of the devices optical properties. Optical losses, guided PL, and pump and probe measurements are studied on both kinds of devices made of Nd-SRSO and Nd-SRSN materials. We finish with a summary of this thesis and future perspectives for such Nd-doped Si-based materials.

Bibliography

---

[1] G. T. Reed, A. P. Knights, Silicon Photonics: An Introduction, Spinger-Verlag, Berlin, 2004

[2] P. G. Kik, M. L. Brongersma, A. Polman, Appl. Phys. Lett. **76** (2000) 2325

[3] M. Lipson, Guiding, Modulating, and Emitting Light on Silicon-Challenges and Opportunities, J. Lightwave Technol. **23** (2005) 4222

[4] M. Wojdak, M. Klik, M. Forcales, O. B. Gusev, T. Gregorkiewicz, D. Pacifici, G. Franzò, F. Priolo, F. Iacona, Phys. Rev. B **69** (2004) 233315

[5] H. S. Han, S. Y. Seo, J. H. Shin, Appl. Phys. Lett. **79** (2001) 4568

[6] A. J. Kenyon, Prog. Quant. Eletron. **26** (2002) 225

[7] O. Debieu, D. Breard, A. Podhorodecki, G. Zatryb, J. Misiewicz, C. Labbe, J. Cardin, F. Gourbilleau, J. Appl. Phys. **108** (2010) 113114

Chapter 1: Rare earth Si-based layers

This chapter provides a detailed description of optical properties of Si nanostructures alone or coupled with rare earth ions such as Er and Nd. Our goal is to show an overview of the main achievements in this topic and present the theory foundation for positioning the work done in this thesis.

1.1 Si Nanostructure

A tremendous result was obtained in 1990 by L. T. Canham[1], who observed with the naked eye and at room temperature a remarkable intense photoluminescence (PL) from Si nanostructure. Since this result would have promising applications in optical communication, optical storage, image, lighting, and optical sensors, it has attracted huge efforts of a wide scientific community on this domain called Silicon Photonics.

1.1.1 Comparison with Si bulk

Si bulk is an indirect band gap material, due to conservation of momentum, the excited electron can only recombine with a hole by emitting or absorbing a phonon[2] leading to poor emission efficiency. This limits its application in optical light source[2]. Consequently, the non-radiative recombination, such as free carrier absorption and Auger recombination, are dominant.

In the case of Si nanostructure, the quantum confinement effect (QCE) modifies the band gap structure:

- Due to localization of exciton in the nanoparticle, an overlapping between the electron and hole wave-function occurs increasing the probability of direct recombination of exciton[3].
- At low dimensions, the electron-hole pairs (excitons) are confined in the nanoparticles leading to a behavior of a "particle in a box" model[4]. It implies that the nanoparticles band gap energy involves inversely with their diameter.

The change of band-gap properties becomes pronounced below a critical size of Si nanoparticles (Si-nps), typically less than 10 nm equal to the exciton Bohr radius[5]. The band gap is dependent on Si-nps size following equation (1.1)[6]:

$$E(eV) = E_{bulk} + C / D^2 \tag{1.1}$$

where E (eV) and E_{bulk} are band gap of Si-nps and Si bulk, respectively, D is the Si-nps diameter and C is the confinement parameter. Therefore, the Si-nps band gap can be carefully engineered by tuning its size.

1.1.2 Fabrication

The evidence of room temperature photoluminescence emission has been published in the 1990s by L. T. Canham[1] in porous Si structure. Since this discovery, numerous techniques have been employed to grow Si-nps embedded within different matrices such as SiO_2, and Si_3N_4. The most used are evaporation[7] [8], laser ablation[9], Si implantation[10], molecular beam epitaxy (MBE)[11], plasma enhanced chemical vapor deposition (PECVD)[12] [13] [14], and magnetron sputtering[15] [16]. These techniques are followed by a post-annealing treatment aiming at agglomerating the excess of Si atoms. The deposited films are classically named SRSO in case of Si-rich SiO_2, and SRSN for Si-rich Si_3N_4.

The microstructure of deposited film is controlled through fabrication parameters and/or post-annealing conditions such as cathode power density for magnetron sputtering[17], the ratio of gas precursors in PECVD[18], annealing temperature and duration[19]. They allow to monitor the size and density of Si-nps and to optimize the optical properties of condensed system[12] [20] [21] [22] [23] [24]. For example, Iacona et al. produced a SRSO film containing 19.1 at.% Si excess by PECVD. They obtained a density of Si-nps of 8×10^{17} $at\cdot cm^{-3}$ for a radius of about 1.5 nm after a 1hour-1100°C-annealing[25].

1.1.3 Optical properties

The absorption coefficient of SRSO films is in general estimated by optical transmission[26] or by photo-thermal deflection[24] experiments. It increases from 10^2 to 10^5 cm^{-1} with photon energy (2-5 eV) and depends on the film composition and annealing conditions. From absorption coefficient, knowing the density of Si-nps, the optical absorption cross section of Si-nps can be estimated and is in the order of 10^{-16} cm^2 at 488 nm, while it increases more than two orders of magnitude at about 350 nm[27].

(a) Photoluminescence

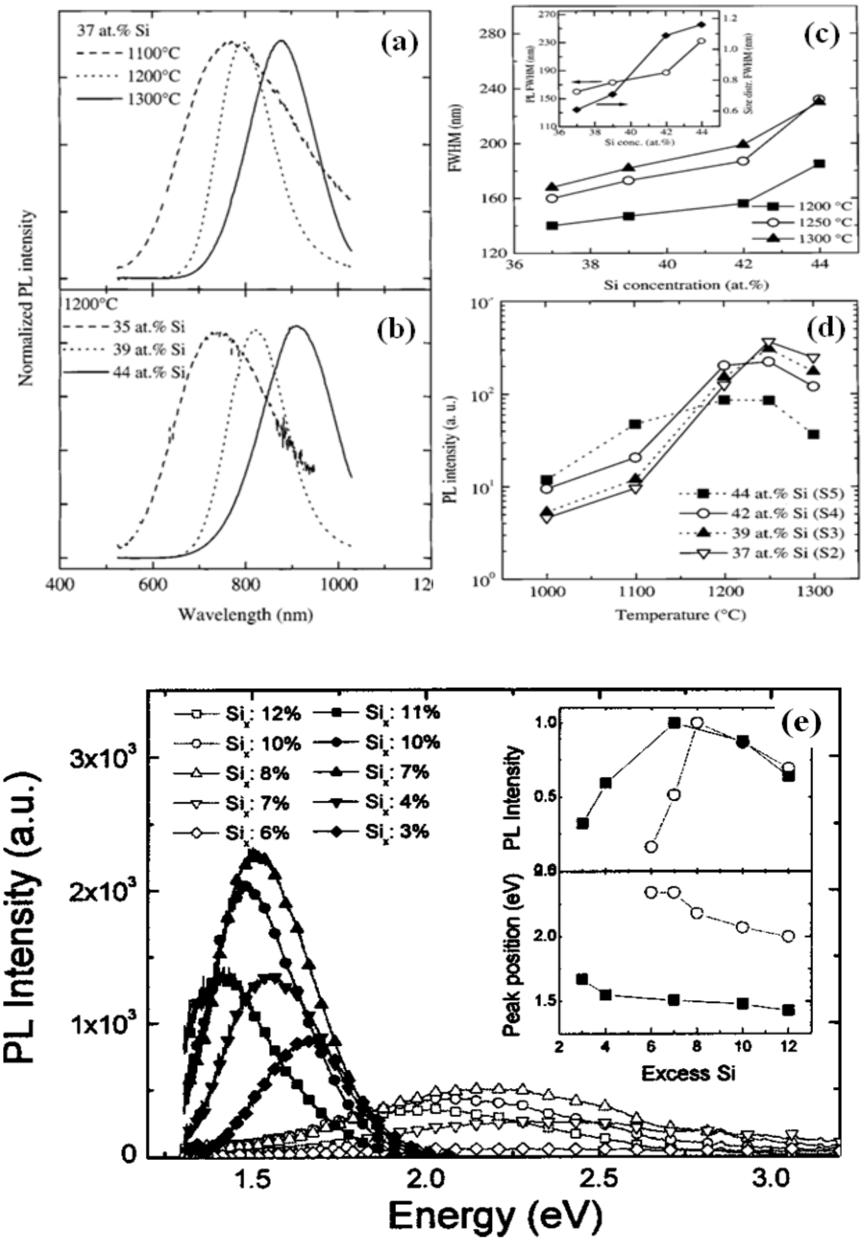

Figure 1.1: (a)-(d) correspond to SRSO samples, (a) PL spectra of 5.6 at.% Si excess samples annealed at indicative temperatures, (b) PL spectra of different Si excess samples annealed at 1200°C, (c) the full width at half maximum of PL peak vs Si excess, and (d) PL intensity vs annealing temperature[12], while (e) comparison of PL spectra of SRSO (closed symbols) and SRSN (open symbols) films[29].

A lot of work has been performed on the study of PL properties of Si-nps embedded in Si-based insulating matrix. For example, Iacona et al.[12] have investigated the effects of annealing temperature on the PL properties of SRSO films fabricated by PECVD (Fig. 1.1(a)-(d)). These authors have seen that (i) both the PL peak position and its full width at half maximum increase with Si content and/or annealing temperature, and (ii) the maximum PL intensity has been achieved for Si excess of 5.6 at.% after an annealing treatment performed at 1250°C during one hour. Depending on the fabrication conditions, the peak position has been recorded from about 500 to 1000 nm[28]. In the case of SRSN layer, a visible PL has also been achieved, which is reported to be blueshifted by 0.6 eV when compared to Si-nps in SiO_2 (Fig. 1.1(e))[29]. Mercaldo et al.[30] report an evolution of PL peak position ranging from 500 to 700 nm with the increasing of Si-nps diameter. In contrast, Kistner et al.[31] do not observe any c-Si-nps but remarkable PL is recorded from these nitride layers. The authors ascribed the emission observed to band-tail state.

In spite of the abounding studies on SRSO material, the physical origin of its photoluminescence (PL) is still under debate. On one hand, Iacona et al.[12] observed that the visible emission gradually red shifts with the increasing of Si-nps size. The authors have attributed such emission to the band-to-band recombination of electron-hole pairs within Si-nps. On the other hand, the PL is proposed to originate from recombination in various defects such as oxygen vacancies or non-bridging oxygen hole centers[32]. The characteristic of defects emission is an invariable peak position with Si-nps size. Fang et al.[33] demonstrated that in a single SRSO film the PL is dominated by defects recombination when the annealing temperatures are below 900°C. For temperature above 1000°C, the emission has another component originating from QCE. Wang et al.[34] have similar results attributing the PL emission to surface states recombination or quantum confinement effects (QCE) depending on the annealing treatment.

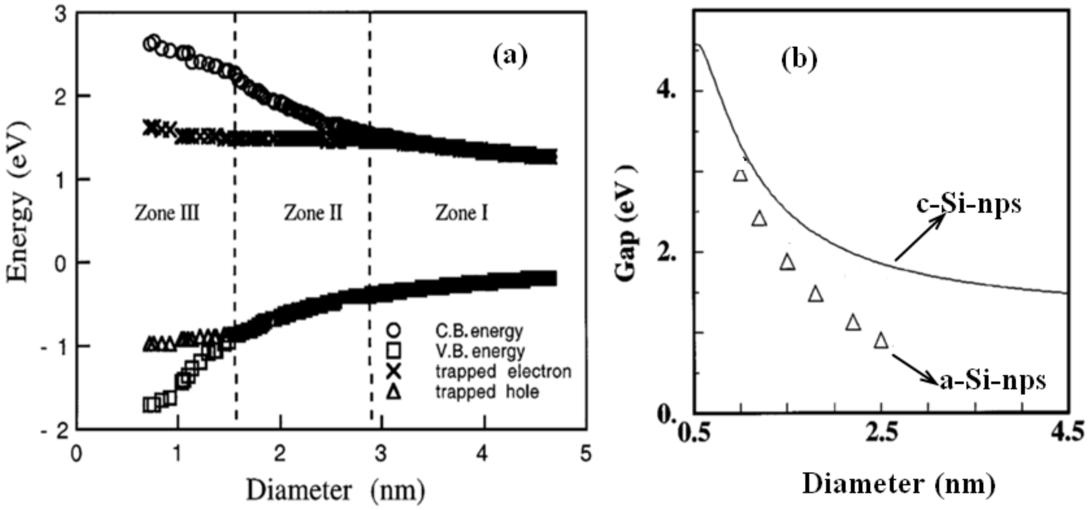

Figure 1.2: (a) Electronic states in crystalline Si-nps vs their diameter[35]*, and (b) average HOMO-LUMO band gap of amorphous Si-nps (a-Si-nps) compared to that of crystalline Si-nps (c-Si-nps)*[36]*.*

The PL red shift has also been noticed by Wolkin el al. in porous Si[35]. As shown in figure 1.2 (a) they observed a gradual extending of the band gap with the decreasing size of crystalline Si-nps (c-Si-nps) (Zone I to Zone III). In Zone III, when the Si-nps decreases, a surface state related energy level appears leading to an emission at a fixed energy which is size independent. In the case of amorphous Si-nps (a-Si-nps), the presence of band tails lowers the band gap leading to the red shift of PL emission by comparison to that of c-Si-nps (Fig. 1.2(b))[36].

(b) Decay time

The photoluminescence decay is of particular interest for getting information about excitation-deexcitation mechanisms in emitting system. In the case of SRSO systems, stretched exponential function behaviors have been widely observed on the PL decay trace[37] [38] [39], given by the following relationship:

$$I(t) = I(0)\exp[(-t/\tau_{PL})^{\beta}] \tag{1.2}$$

In this equation, I(t) and I(0) are the PL intensities recorded as a function of time and t = 0, respectively; τ_{PL} is the decay time and β is the a stretch factor ranging from 0 to 1. The value of β is a signature of the interaction between neighboring nanocrystals or/and between nanocrystals and defect states[40]. A room temperature PL lifetime measured at an emission wavelength of 700 nm is found to be about 12 µs with β = 0.6 in an 1100°C-annealed sample containing 16.1 at.% Si excess[40]. After a post-annealing at 1000°C under flowing O_2 gas, an increase lifetime up to 43 μs with β=0.79 has been demonstrated. These authors attribute this increase to the achievement of stoichiometric SiO_2 in the surrounding of nanocrystal. The disorder of the matrix also plays a role in emission properties. Thus for a decreasing disorder, it has been observed a variation of the lifetime from 36 to 70 μs (Fig. 1.3(a)), and an increase of the stretch factor β from 0.55 to 0.68[37]. The effect of measurement temperature on lifetime has also been investigated by Dovrat et al.[38] as seen in figure 1.3(b). The PL lifetimes vary from about 30-100 μs at room temperature to about 1.0 ms at 10 K for sample containing 18 at.% Si excess. This demonstrates the increasing role of non-radiative channels in the decay time with increasing measurement temperature. In the case of SRSN layers, the PL decay shows a shorter lifetime of a few nanoseconds. The decay traces were fitted by Dal Negro et al.[41] considering a double exponential model characterized by a fast decay constant of approximately 1 ns, and a longer decay component in the range of 5-10 ns. Wang et al.[42] found that the lifetime is inversely proportional to the emission energy, such as 7.6 ns at 2.99 eV, 8.1 ns at 2.61 eV, and 11.0 ns at 2.16 eV. The shortening of the SRSN decay time compared to SRSO one is attributed to the origin of the emission, band tail for the former and nanocrystal with QCE for the latter.

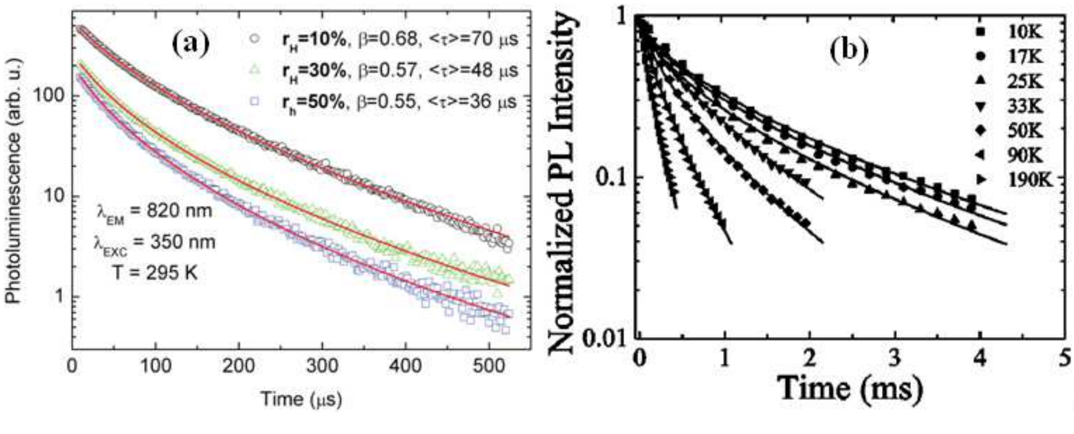

Figure 1.3: Non-single exponential PL decays measured (a) at room temperature for samples fabricated by reactive magnetron sputtering[37]; and (b) at the indicative temperatures for sample containing 18 at.% Si excess[38].

1.1.4 Devices

The main advantage of using Si-nps is to integrate light source and/or amplifier within CMOS photonics platform. In 2000, L. Pavesi et al.[43] reported stimulated emission and optical gain in c-Si-nps using the variable stripe length method. The gain coefficient at about 800 nm wavelength reaches a value as high as 100 cm^{-1}. These findings opened a route towards the realization of a Si-based laser. Thereafter in October 2004, the first silicon Raman laser was announced[44], while in January 2005 the first all-continuous wave CW silicon Raman laser was reported[45].

1.2 Er and Si nanostructure

1.2.1 Introduction

In 1994 J. Kenyon et al.[46] have evidenced the great enhancement of Er^{3+} PL intensity when Si-nps are present in the matrix. This PL enhancement is attributed to a sensitization effect which consists in an efficient energy transfer from Si-nps towards Er^{3+} ions. Thus, rare earth ions benefit from the high absorption cross section of Si-nps (about 10^{-16} cm^2[47] with respect to 10^{-20} for rare earth ions in SiO_2[48]).

Er^{3+} ions are essentially used in telecommunications because of the radiative $^4I_{3/2}\rightarrow{}^4I_{15/2}$ transition at 1.54 μm that corresponds to the minimum absorption of standard silica optical fibers[49]. As a consequence, tremendous interest from all over the world turns to the study on interaction between Si-nps and Er^{3+} ions.

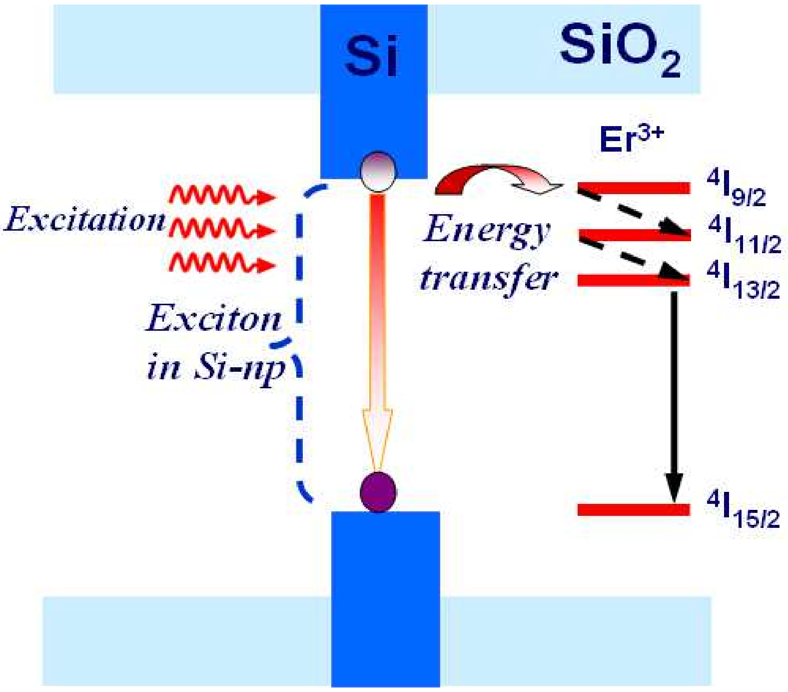

Figure 1.4: Illustration of energy transfer from Si-nps to Er^{3+} ions.

The interaction mechanism can be described as shown in figure 1.4. The recombination of exciton in the Si-nps is at the origin of the excitation of the Er^{3+} ions. The energy transfer occurring from the Si-nps towards the Er^{3+} ions leads to the excitation of the 4f electrons from the ground level of the Er ($^4I_{15/2}$) to the excited states ($^4I_{13/2}$, $^4I_{11/2}$, and $^4I_{9/2}$). Then two deexcitation steps, $^4I_{9/2} \rightarrow {}^4I_{11/2}$ and $^4I_{11/2} \rightarrow {}^4I_{13/2}$, occurs in a non-radiative way and in characteristic times[50] of about few 100 ns. And finally the excitons in $^4I_{13/2}$ level recombine radiatively to the ground level emitting a photon at 0.98 and 1.54 μm corresponding to the transitions $^4I_{11/2} \rightarrow {}^4I_{15/2}$ and $^4I_{13/2} \rightarrow {}^4I_{15/2}$, respectively.

1.2.2 Fabrication

The fabrication of Si-based films co-doped by Si-nps and Er ions concerns many technologies. For examples, ion implantation of fused silica[47] [51] [52] allows obtaining SRSO layers having a Si excess ranging from 5 to 15 at.%. These films are then annealed to form and grow Si-nps in host matrix. This step is followed by Er implantation with different Er ion contents ranging from 2×10^{19} to 6×10^{20} cm^{-3}. Some works carry out only one step of Er implantation into the SRSO films, which are deposited by PECVD[53] [54]. A more direct approach is a co-incorporation of both Er ions and Si excess during the deposition of Si-based layer as shown in the case of PECVD[55], co-evaporation[56] or magnetron co-sputtering[57] techniques. The PECVD method consists in plasma dissociation of silane, nitrous oxide and a volatile erbium organic chelate in a parallel-plate plasma chamber. The film stoichiometry is controlled by varying the relative flow rates of the reacting gases, and by monitoring both the temperature of organic precursor and the flow rate of the gas. The co-evaporation method is based on simultaneous evaporation of SiO powder from a thermal cell, SiO_2 powder from an electron beam gun, and Er from an effusion cell. The power of the evaporation sources is adjusted accordingly to obtain the desired sample composition. The magnetron co-sputtering technique consists in sputtering simultaneously Si, SiO_2, and Er_2O_3 targets in pure Ar plasma. The RF power applied on each cathode allows controlling the Si excess and Er content incorporated in the growing layer. This deposition technique permits also to grow Er-doped nitride layer by co-sputtering Si and Er_2O_3 targets in Nitrogen-rich plasma[17]. Magnetron sputtering deposition has been used in this thesis work and will be described in detail in the chapter 2.

1.2.3 Optical properties

(a) Photoluminescence

The demonstration of the efficient energy transfer from Si-nps to Er^{3+} ions is shown in figure 1.5(a). With the increasing of Er content incorporated into the SiO_2 matrix, the PL peak intensity of Si-nps gradually decreases while the 1.54µm-Er PL peak increases[58]. The characteristic distance for effective interaction between Si-nps and Er^{3+} ions is less than about 0.5 nm[59] [60], and the interaction coefficient is a decreasing exponential with increasing Si-np:Er^{3+} distance[61]. Consequently, the critical points to achieve an intense IR emission are the Si-nps density and the Er^{3+} ions concentration. Hijazi et al.[62] have optimized the coupling between Si-based sensitizers and Er^{3+} ions via tuning both the Er content and Si excess incorporated in SRSO matrix. They achieved the maximum Er^{3+} PL intensity corresponding to the films containing 3.5×10^{20} cm^{-3} Er atoms and 9 at.% Si excess. Numerous works[63] [64] [65] focus on samples annealed at low temperatures (in the 700-900°C range), because higher temperature would result in a coalescence phenomenon of sensitizers and/or

Er^{3+} ions. Moreover, these low annealing temperature processes have allowed to demonstrate that the physics of transfer mechanism does not depend on the Si-np nature (crystalline or amorphous)[61]. For low annealing temperature, other kinds of sensitizers have been reported:

- the luminescence centers (LCs)[66]
- the atomic scale Si sensitizers[67]
- the Si oxygen deficient centers (SiODCs)[68].

In the case of SRSN host matrix, similar Er^{3+} PL intensities are observed by Yerci et al[69] across a large range of Si concentration from 0 to 12.5 at.%. The Er^{3+} PL emission has been optimized after an annealing treatment at 800°C during 200 seconds. Some results support the quantum confined Si-nps acting as sensitizer for Er^{3+} ions[70], whereas some others claim that the band tail states are at the origin of the sensitization of Er^{3+} ions[71] [72].

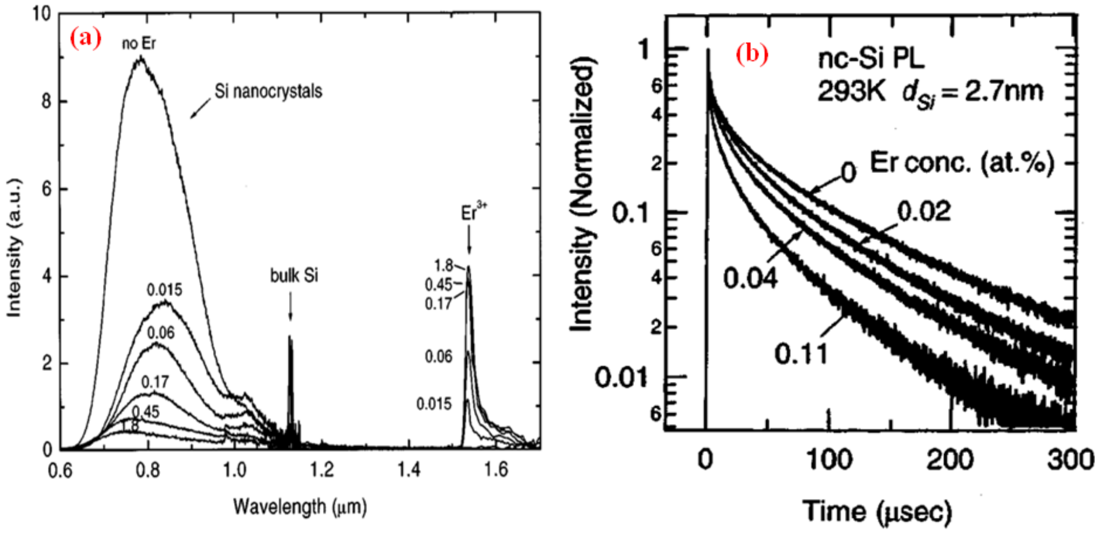

Figure 1.5: (a) PL spectra of Si nanocrystal-doped SiO_2 containing different Er content in the range of 0-1.8 at.%[58], and (b) decay curves of Si nanocrystal dependence on Er content[60].

(b) Decay time

With increasing Er content, Watanable et al.[60] have evidenced a shortening of the Si-nps radiative decay time (Fig. 1.5(b)) which is a signature of the increasing number of Er ions coupled to Si-nps. Depending on the nature of the matrix (silicon oxide or nitride), the fabrication process and annealing step, the lifetime of the

$I_{13/2}$-$I_{15/2}$ transition is ranging from about 1 ms[54] up to 9 ms[5]. In the case of SRSO matrix, its value shows a drastic reduction from 3.7 to 1.5 ms as the Si excess is increased from 3 to 4 at.%[73]. The same trend has been reported in the case of increasing Er content[74]. In contrast, longer annealing duration up to 1 hour at 800°C favors longer Er^{3+} lifetime[75]. In the case of SRSN host matrix, similar evolution of Er^{3+} lifetime is reported with a decrease from 3.2 to 1.4 ms when Si excess is varying from 0 to 17 at.%[73]. Recently, Steveler et al.[76] show that the Er^{3+} lifetime varies from about 0.9 to 1.4 ms when annealing temperature is ranging from 600 to 1100°C.

Optimum luminescence properties, i.e. strong luminescence intensity and decay time close to maximum theoretical limit, are the result of two compromises. First, the silicon excess should be important but below a threshold above which the amount of defects created induces too many non-radiative de-excitation pathways. Second, a significant content of rare earth ions is needed but it should be below a threshold beyond which cross relaxations begin, decreasing the global luminescence efficiency.

1.2.4 Devices

The indirect excitation of Er^{3+} ions by Si-nps in Si-based films provides promising potential as an active medium for compact and low cost devices, such as optical amplifier, light emitting diodes (LEDs), or laser. The most advanced demonstration highlighting the advantage of Si-nps sensitizing for Er^{3+} ions is a rid waveguide amplifier based on the Si-based film, which is pumped by low-cost LEDs as shown in figure 1.6[77]. As the Si-based films are transparent and have higher refractive index than that of SiO_2, light can be confined and transmitted along the film acting as a core of waveguide. The pumping light is absorbed by Si-nps which transfer their energy to Er^{3+} ions. The signal propagating in such a waveguide is amplified through stimulated emission of Er^{3+} ions.

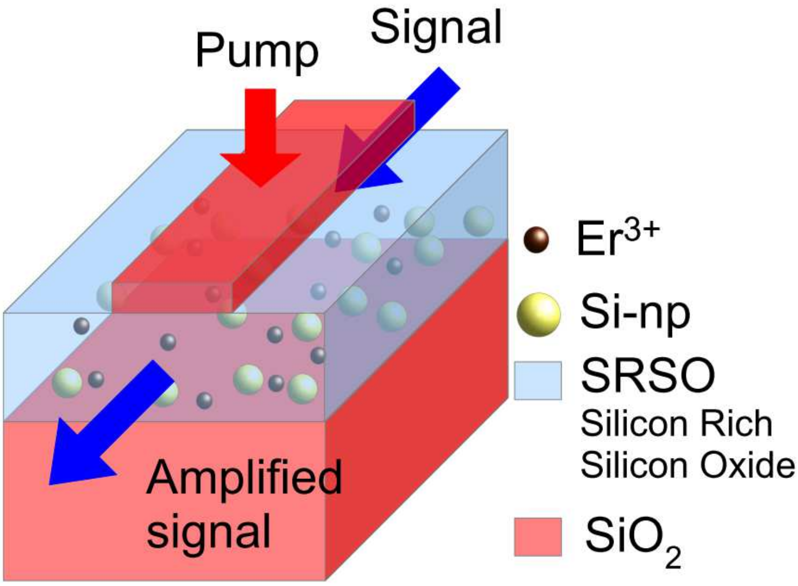

Figure 1.6: Waveguide amplifier based on co-doped of Si-nps and Er in Si-based film adopting vertical pump sources supplied by low-cost LEDs.

Nevertheless, there are many processes that can compete with the transfer mechanism between Si-nps and Er^{3+} ions, generating extra pump power dependent losses or increasing the pump threshold necessary for population inversion of Er^{3+} ions. For Si-nps, the exciton recombination rate is increased through Auger process[78] while carrier absorption phenomenon leads to a decrease of excitons available for energy transfer to rare earth ions[79]. In the case of Er^{3+} ions, several processes are responsible of Er^{3+} emission quenching: (i) excited state absorption in an Er^{3+} ion[80], (ii) energy migration and cross relaxation between Er^{3+} ions[81], (iii) cooperative up-conversion between excited Er^{3+} ions[82], and (iv) the energy back transfer from Er^{3+} ions to Si-nps[83]. These issues really prevent the achievement of net gain and the realization of effective light source of Er-doped Si-based materials[84].

1.3 Nd and Si nanostructure

1.3.1 Introduction

Nd^{3+} ion has also a resonant energy level with the bottom of the conduction band of the Si-nps and therefore has been the subject of some interest[85]. This ion has two interesting emission wavelengths as shown in figure 1.7:

- The 1.064 µm emission which has been widely used for laser when Nd ions are incorporated in a YAG crystal. The application domains are etching, cleaning (matrices, art objects) or medicine fields (elimination of the membranes, treatment of skin cancers and removing of lithiases in body).
- The 1.3 µm emission which is slightly absorbed by the silica fiber (~0.3 dB.km^{-1}) and therefore is interesting for optical telecommunication in O-band.

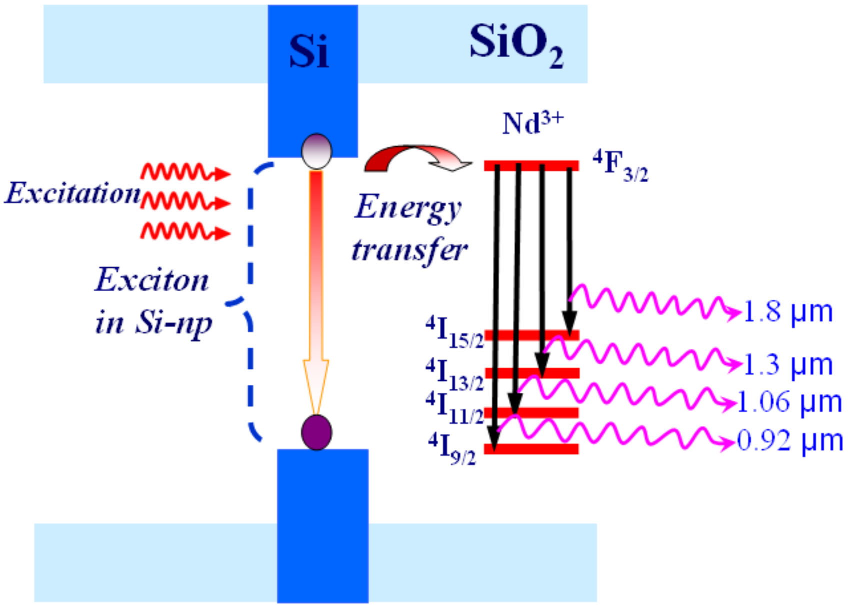

Figure 1.7: Illustration of energy transfer from Si-nps to Nd^{3+} ions.

In Si-Nd^{3+} system, the same interaction process described in the case of Er^{3+} ions (cf section §1.2.1) occurs. The exciton generated inside the Si-nps by the absorption of a photon recombines non-radiatively by exciting a Nd^{3+} ion in $^4F_{3/2}$ level via a dipole-dipole interaction (seen Fig. 1.7). From $^4F_{3/2}$ level four radiative transitions occurs leading to four emission wavelengths at 1.8, 1.3, 1.06, and 0.92 µm corresponding to the $^4F_{3/2} \rightarrow {}^4I_{15/2}$, $^4F_{3/2} \rightarrow {}^4I_{13/2}$, $^4F_{3/2} \rightarrow {}^4I_{11/2}$, and $^4F_{3/2} \rightarrow {}^4I_{9/2}$ deexcitation, respectively. Their relative emission intensities vary and are described by the different transition rates which are about 10, 300, 1460, and 1280 s^{-1}, respectively[86] [87] [88].

As in the case of Er^{3+} ions, the energy transfer time is very short (about 150 ns)[89], which favors the excitons within Si-nps to preferably sensitize Nd^{3+} ions rather than to radiatively recombine. Size of Si-nps plays an important role in the sensitization process. Thus, Watanable et al.[90] have demonstrated that the increase in the Si-nps size from 2.7 to 3.8 nm results in a decreasing of Nd^{3+} PL intensity. They concluded that only small Si-nps can excite the $^4F_{3/2}$ level of Nd^{3+} ions.

1.3.2 Nd-doped Matrices

(a) SiO_x matrix

A SiO_x or called also SRSO (Si-rich Silicon Oxide) is a non-stoichiometric material, which can be considered as an oxygen- deficient SiO_2. The co-incorporation of Si excess and Nd ion allows the formation of Si-np that can be optically coupled to Nd^{3+}. In order to optimize such coupling, two main ways have been investigated:

- The film composition engineered by the deposition conditions. Nd content is one important factor. MacDonald et al.[89] have varied the Nd content from 0.19 to 1.29 at.% in co-evaporated films and obtained a maximum PL intensity corresponding to the 0.29 at.%. In reactive sputtered layers, this maximum value has been found to be lower than 0.1 at.%[91]. They both demonstrated that the high Nd content would decrease the amount of optically active Nd^{3+} ions and/or form Nd_2O_3 clusters leading to cross relaxation between Nd ions. Si excess is the other key parameter to maximize the Si-np:Nd^{3+} coupling number. High Si-nps density is needed but a high Si excess favors the non-radiative pathways as detailed in the case of the Er ions. For example, the maximum PL intensity of Nd^{3+} ions at 1.064 μm corresponds to 5.6 at.% Si excess reported by S-Y. Seo et al.[92].
- The film microstructure monitored by the post-annealing process. During annealing treatment, a phase separation occurs allowing the growth of Si-nps[93]. The duration and temperature have to be controlled to permit an optimized distribution of Si-nps and therefore a high sensitizer density. Concerning the Nd ions, this step is of importance too because it favors the optical activation of Nd^{3+} ions but a too high temperature may induce the formation of Nd clusters[94]. Bréard et al.[95] have evidenced the presence of two decay times in their PL experiments (Fig. 1.8): (i) a fast decay component in the range of 5 to 50 μs attributed to Nd_2O_3 clusters

and (ii) a slow decay component ranging from 50 to 170 μs originating from isolated Nd^{3+} ions.

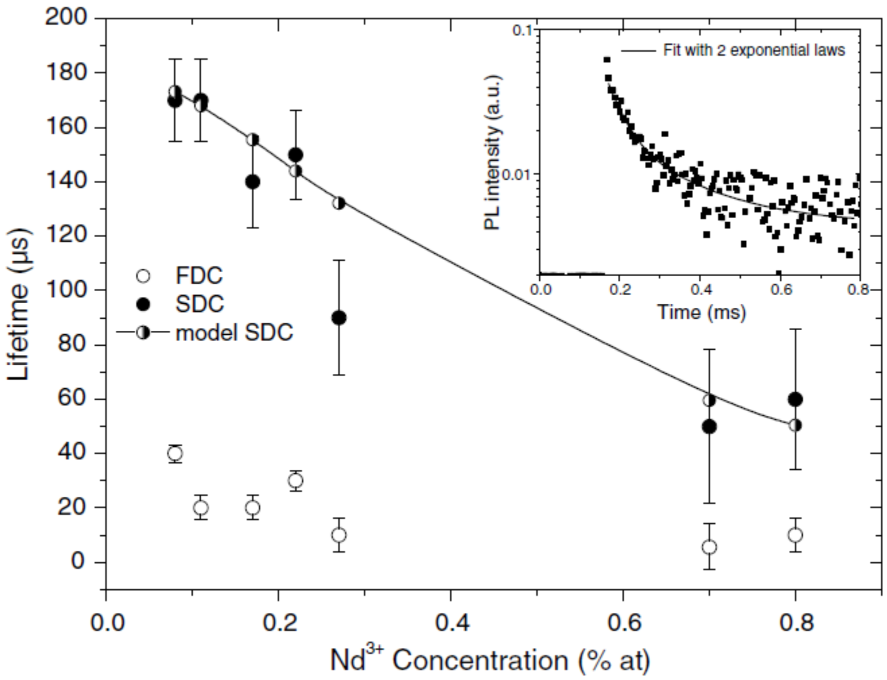

Figure 1.8: Nd^{3+} concentration dependence of lifetimes[95] both for 0. 92-μm-Nd^{3+} PL fitted by two exponential laws. The inset shows its typical decay curve with fitting line.

(b) SiN_x matrix

SiN_x matrix is derivate from stoichiometric Si nitride (Si_3N_4) in which x=1.33. When x<1.33 Si atoms are incorporated into Si_3N_4 and the matrix is generally called Si-rich Silicon Nitride (SRSN).

Contrarily to the Er doped nitride system, only a few papers report optical properties of Nd-SRSN system one. Li et al.[94] have studied the evolution of Nd^{3+} PL intensity as a function Si excess (x ranging from 1.27 to 1.04). They have evidenced a dramatic decrease of Nd^{3+} emission with the increasing Si excess. Such an evolution is explained by the decrease of band gap as well as the density of localized defects states that act as sensitizers towards the Nd^{3+} ions. For larger Si excess (x=0.6), Biggemann et al.[96] observed the maximum Nd^{3+} PL efficiency corresponding to matrix band gap, which is twice the $^4F_{3/2} \rightarrow {}^4I_{9/2}$ transition energy. These authors evidenced an efficient sensitization of the Nd^{3+} ions by the presence of localized defect state in the band gap. The maximum Nd^{3+} PL intensity has been achieved for a concentration of 3×10^{20} at.cm^{-3}[94]. As in the case of SiO_x matrix, higher Nd content leads to the formation of Nd_2O_3 clusters. The $^4F_{3/2} \rightarrow {}^4I_{11/2}$ decay time of Nd^{3+} PL in this SRSN matrix has a two exponential feature with a fast (50 μs) and slow (140 μs) lifetimes[94].

1.3.3 Devices

Once effective light emission in optical fiber was achieved from Nd^{3+} ions doped in Si-based materials, this provided an alternative way to solve limiting factors previously mentioned in the case of Er^{3+} doping. Several results have been found to inspire and motivate researchers. In the case of SiO_x matrix, Rebohle et al.[97] have clearly observed the electroluminescence peak from Nd^{3+} ions. In the case of SiN_x matrix, an optical gain of 270 cm^{-1} at 1130 nm has been determined from the planar waveguides excited by non-resonant wavelength with Nd^{3+} transitions[98]. And Li et al.[94] have fabricated an active micro-disk resonator radiatively emitting 1.1 μm by stimulation mechanism.

1.4 Conclusion:

A review of Si-based light emission has been performed in this chapter concluding that the important potential applications of Si photonics have driven an increasing interest on the Si-based materials doped by Er^{3+} rare earth ions. An achievement of net gain from Er^{3+} ions has been hampered as mentioned above by several critically limited factors such as excited state absorption, energy migration, cross relaxation, and cooperative up-conversion. Moreover, the nature of the three-level electronic 4f structure of Er^{3+} ions is a detrimental feature which leads to the re-absorption of the 1.54 μm emitted light. In contrast, Nd^{3+} ions have four-level structure, for the emission at 1.06μm, favoring the achievement of a large population inversion. Consequently, such a system could be promising for the fabrication of a net gain Si-based amplifier.

Nevertheless, Nd-doped Si-based system presents some limitations that can be detrimental for getting an efficient device. To enhance the PL properties of Nd-doped layers, Nd content and Si excess should be optimized. On one hand, a high Nd concentration favors the energy migration and cross relaxation, as well as formation Nd_2O_3 clusters. One the other hand, a high Si-nps density required for decreasing the

Si:Nd distance, would lead to the decrease of the Nd^{3+} decay time (the order of μs). These different limiting factors are serious drawbacks for sensitization of rare earth ions by Si-nps in Nd-doped Si-based films and thus the breakthroughs are required for the achievement of Si photonics devices.

This is the objective of this work. We proposed to improve by a fine tuning of the fabrication and/or annealing conditions, the microstructure of the layers and to maximize of both Si-nps and Nd^{3+} ions density, to reach Nd^{3+} population inversion and gain. The PhD work has been done within the ANR DAPHNES project (ANR-08-NANO-005).

Bibliography

---

[1] L. T. Canham, Appl. Phys. Lett. **57** 1046 (1990)

[2] B. Jalali, http://www.aps.org/publications/apsnews/200603/forefronts.cfm,

[3] U. Gnutzmann , K. Clausecker, Appl. Phys. **3** (1974) 9

[4] L. E. Brus, J. Chem. Phys. **79** (1983) 5566

[5] J. P. Wilcoxon, G. A. Samara, P. N. Provencio, Phys. Rev. B **60** (1999) 2704

[6] N. M. Park, C. J. Choi, T. Y. Seong, S. J. Park, Phys. Rev. Lett. **86** (2001) 1355

[7] H. Rinnert, M. Vergnat, G. Marchal, A. Burneau, J. Lumin. **80** (1999) 445

[8] M. Zacharias, J. Heitmann, R. Scholz, U. Kahler, M. Schmidt, J. Blasing, Appl. Phys. Lett. **80** (2002) 661

[9] X.Y. Chen, Y.F. Lu, Y.H. Wu, B.J. Cho, W.D. Song, D.Y. Dai, J. Appl. Phys. **96**, (2004) 3180

[10] S. Guha, M. D. Pace, D. N. Dunn, I. L. Singer, Appl. Phys. Lett. **70** (1997) 1207

[11] Z. H. Lu, D. J. Lockwood, J.M. Baribeau, Nature, **378** (1995) 258

[12] F. Iacona, G. Franzò, and C. Spinella, J. Appl. Phys. **87** (2000)1295

[13] L. Y. Chen, W. H. Chen, and F.C. N. Hong, Appl. Phys. Lett. **86** (2005)193506

[14] L. B. Ma, R. Song, Y. M. Miao, C. R. Li, Y. Q. Wang, Z. X. Cao, Appl. Phys. Lett. **88** (2006) 093102

[15] L. F. Bian, C. G. Zhang, W. D. Chen, C. C. Hsu, Y. H. Qu, D. S. Jiang, J. Appl. Phys. **99** (2006) 094302

[16] R. Nalini, L. Khomenkova, O. Debieu, J. Cardin, C. Dufour, M. Carrada, F. Gourbilleau, Nanoscale Res. Lett. 7 (2012)124

[17] S. Cueff, C. Labbé, L. Khomenkova, O. Jambois, P. Pellegrino, B. Garrido, C. Frilay, R. Rizk, Mater. Sci. Eng. B **177** (2012) 725

[18] M. Wang, D. Li, Z. Yuan, D. Yang, D. Que, Appl. Phys. Lett. **90** (2007) 131903

[19] L. Khomenkova, F. Gourbilleau, J. Cardin, O. Jambois, B. Garrido, R. Rizk, J. Lumin. **129** (2009) 1519

[20] W. Pan, R. G. Dunn, M. S. Carroll, J. C. Banks, L. N. Brewer, J.Non-Cryst. Solids **354** (2008) 975

[21] R. Pratibha Nalini, C. Dufour, J. Cardin, F. Gourbilleau, Nanoscale Res. Lett. **6** (2011) 156

[22] E. Quiroga-González, W. Bensch, M. Aceves-Mijares, Z. Yu, R. López-Estopier, K. Monfil-Leyva, Thin Solid Films, **519** (2011) 8030

[23] B. G. Fernandez, M. Lopez, C. Garcia, A. Perez-Rodriguez, J. R. Morante, C. Bonafos, M. Carrada, A. Claverie, J. Appl. Phys. **91** (2002) 798

[24] I. Stenger, B. Gallas, L. Siozade, C. C. Kao, S. Chenot, S. Fisson, G. Vuye, J. Rivory, J. Appl. Phys. **103** (2008) 114303

---

[25] P. R. Wilson, T. Roschuk, K. Dunn, E. N. Normand, E. Chelomentsev, O. H. Zalloum, J. Wojcik, P. Mascher, Nanoscale Res. Lett. **6** (2011) 168

[26] T. Inokuma, Y. Wakayama, T. Muramoto, R. Aoki, Y. Kurata, S. Hasegawa, J. Appl. Phys. **83** (1998) 2228

[27] D. Kovalev, J. Diener, H. Heckler, G. Polisski, N. Künzner, F. Koch, Phys. Rev. B **61**, (2000) 4485

[28] C. Lecerf, Elaboration et caractérisations de films d'oxyde de gallium dopés terres rares, PhD thesis, Universite de caen/Basse-Normandie, (2011)

[29] M. S. Yang, K. S. Cho, J. H. Jhe, S. Y. Seo, J. H. Shin, K. J. Kim, D. W. Moon, Appl. Phys. Lett. **85** 3408 (2004)

[30] L.V. Mercaldo, P.D. Veneri, E. Esposito, E. Massera, I. Usatii, C. Privato, Mater. Sci. Eng. B **159** (2009) 77

[31] J. Kistner, X. Chen, Y. Weng, H.P. Strunk, M.B. Schubert, J. H. Werner, J. Appl. Phys. **110** (2011) 023520

[32] G. R. Lin, C. J. Lin, J. Appl. Phys. **95** (2004) 8484

[33] Y. C. Fang, Z. J. Zhang, M. Lu, J. Lumin. **126** (2007) 145

[34] M. Wang, D. Yang, D. Li, Z. Yuan, D. Que, J. Appl. Phys. **101** (2007) 103504

[35] M. V. Wolkin, J. Jorne, P. M. Fauchet, G. Allan, C. Delerue, Phys. Rev. Lett. **82** (1999) 197.

[36] G. Allan, C. Delerue, M. Lannoo, Phys. Rev. Lett.**78** (1997) 3161

[37] G. Zatryb, A. Podhorodecki, J. Misiewicz, J. Cardin, F. Gourbilleau, Nanoscale Res. Lett. **6** (2011) 106

[38] M. Dovrat, Y. Goshen, J. Jedrzejewski, I. Balberg, A. Sa’ar, Phys. Rev. B **69** (2004) 155311

[39] R. J. Walters, J. Kalkman, A. Polman, H. A. Atwater, M. J.A. de Dood, Phys. Rev. B **73** (2006) 132302

[40] M.L. Brongersma, A. Polman, K.S. Min, E. Boer, T. Tambo, H.A. Atwater, Appl. Phys. Lett. **72** (1998) 2577

[41] L. Dal Negro, J. H. Yi, L. C. Kimerling, S. Hamel, A. Williamson, and G. Galli, Appl. Phys. Lett. **88** 183103 (2006)

[42] M. Wang, M. Xie, L. Ferraioli, Z. Yuan, D. Li, D. Yang, and L. Pavesi, J. Appl. Phys. **104** 083504 (2008)

[43] L. Pavesi, L. D. Negro, C. Mazzoleni, G. Franzo, F. Priolo, Nature **408** (2000) 440

[44] O. Boyraz, B. Jalali, Opt. Express **12** (2004) 5269.

[45] H. Rong, A. Liu, R. Jones, O. Cohen, D. Hak, R. Nicolaescu, A. Fang, M. Paniccia, Nature **433** (2005) 292.

[46] A.J. Kenyon, P.F. Trwoga, M. Federighi, C.W. Pitt, J. Phys.: Condens. Matter **6** (1994) L319

[47] P. G. Kik, M.L. Brongersma, A. Polman, Appl. Phys. Lett. **76** (2000) 2325

[48] M. Lipson, Guiding, J. Lightwave Technol. **23** (2005) 4222

[49] E. Desurvire, Physics Today **47** (1994) 20

[50] D. Pacifici, G. Franzò, F. Priolo, F. Iacona, L. Dal Negro, Phys. Rev. B 67 (2003) 245301

[51] P. Pellegrino, B. Garrido, J. Arbiol, C. Garcia, Y. Lebour, J. R. Morante, Appl. Phys. Lett. **88** (2006) 121915

[52] C. E. Chryssou, A. J. Kenyon, T. S. Iwayama, C. W. Pitt, D. E. Hole, Appl. Phys. Lett. **75** (1999) 2011

[53] G. Franzò, D. Pacifici, V. Vinciguerra, F. Priolo, F. Iacona, Appl. Phys. Lett. **76** (2000) 2167

[54] F. Priolo, G. Franzò, D. Pacifici, V. Vinciguerra, F. Iacona, A. Irrera, J. Appl. Phys. **89** (2001) 264

[55] A. J. Kenyon, C. E. Chryssou, C.W. Pitt, T. Shimizu-Iwayama, D. E. Hole, N. Sharma, C. J. Humphreys, J. Appl. Phys. **91** (2002) 367

[56] G. W. Adeola, H. Rinnert, M. Vergnat, Physica E **41** (2009) 1059

[57] M. Fujii, M. Yoshida, Y. Kanzawa, S. Hayashi, K. Yamamoto, Appl. Phys. Lett. **71** (1997) 1198

[58] P. G. Kik, A. Polman, J. Appl. Phys. **88** (2000) 1992

[59] F. Gourbilleau, C. Dufour, R. Madelon, and R. Rizk, J. Lumin. **126** (2007) 581

[60] K. Watanabe, M. Fujii, S. Hayashi, J. Appl. Phys. **90** (2001) 4761

[61] A. Pitanti, D. Navarro-Urrios, N. Prtljaga, N. Daldosso, F. Gourbilleau, R. Rizk, B. Garrido, L. Pavesi, J. Appl. Phys. **108** (2010) 053518

[62] K. Hijazi, R. Rizk, J. Cardin, L. Khomenkova, F. Gourbilleau, J. Appl. Phys. **106**, (2009) 024311

[63] G. W. Adeola, H. Rinnert, P. Miska, M. Vergnat, J. Appl. Phys. **102** (2007) 053515

[64] F. Gourbilleau, M. Levalois, C. Dufour, J. Vicens, R. Rizk, J. Appl. Phys. **95** (2004) 3717

[65] A. Polman, D. C. Jacobson, D. J. Eaglesham, R. C. Kistler, J. M. Poate, J. Appl. Phys. **70** (1991) 3778

[66] O. Savchyn, F. R. Ruhge, P. G. Kik, R. M. Todi, K. R. Coffey, H. Nukala, H. Heinrich, Phys. Rev. B **76** (2007) 195419

[67] K. Hijazi, R. Rizk, J. Cardin, L. Khomenkova, F. Gourbilleau, J. Appl. Phys. **106** (2009) 024311

[68] S. Cueff, C. Labbe, B. Dierre, F. Fabbri, T. Sekiguchi, X. Portier, R. Rizk, J. Appl. Phys. **108** (2010) 113504

[69] S. Yerci, R. Li, S. O. Kucheyev, T. van Buuren, S. N. Basu, L. D. Negro, Appl. Phys. Lett. **95** (2009) 031107

[70] L. F. Bian, C. G. Zhang, W. D. Chen, C. C. Hsu, L. B. Ma, R. Song, and Z. X. Cao, Opt. Mater. **29** (2007) 1071

---

[71] S. Yerci, R. Li, S. O. Kucheyev, T. van Buuren, S. N. Basu, N. Soumendra, L. D. Negro, *IEEE* J. Sel. Topics Quantum Electron. **16** (2010) 114

[72] E. Steveler, H. Rinnert, X. Devaux, M. Dossot, M. Vergnat, Appl. Phys. Lett. **97** (2010) 221902

[73] J. S. Chang, K. Suh, M. S. Yang, and J. H. Shin, Silicon Photonics II: Components and Integration, Lockwood，P. Lorenzo (Eds.) XVI, (2011) 95

[74] K. Hijazi, R. Rizk, J. Cardin, L. Khomenkova, and F. Gourbilleau, J. Appl. Phys. **106**, 024311 (2009)

[75] L. Khomenkova, F. Gourbilleau, J. Cardin, R. Rizk, Physica E, **41**, (2009), 1048

[76] E. Steveler, H. Rinnert, X. Devaux, M. Dossot, M. Vergnat, Appl. Phys. Lett. **97**, (2010) 221902

[77] J. Lee, J. H. Shin, N. Park, J. Lightwave Technol. **23** (2005) 19.

[78] J. Palm, F. Gan, B. Zheng, J. Michel, L. C. Kimerling, Phys. Rev. B **54** (1996) 17603

[79] D. Navarro-Urrios, A. Pitanti, N. Daldosso, F. Gourbilleau, R. Rizk, G. Pucker, and L. Pavesi, Appl. Phys. Lett. **92**, (2008) 051101 (2008)

[80] C. J. Oton, W. H. Loh, A. J. Kenyon, Appl. Phys. Lett. **89** (2006) 031116

[81] A. J. Kenyon, Prog. Quant. Eletron. **26** (2002) 225

[82] D. Pacifici, G. Franzò, F. Priolo, F. Iacona, L. Dal Negro, Phys. Rev. B **67** (2003) 245301

[83] A. Polman, J. Appl. Phys. **82** (1997) 1

[84] N. Daldosso, D. Navarro-Urrios, M. Melchiorri, C. Garcia, P. Pellegrino, B. Garrido, C. Sada, G. Battaglin, F. Gourbilleau, R. Rizk, L. Pavesi, *IEEE* J. Sel. Topics Quantum Electron. **12** (2006)1067

[85] A. N. MacDonald, A. Hryciw, Q. Li, A. Meldrum, Opt. Mater. **28** (2006) 820

[86] L. R. P. Kassab, S. Tatumi, C. M. S. Mendes, L. C. Courrol, N. U. Wetter, Opt. Express **6** (2000)104

[87] V. Mehta, G. Aka, A. L. Dawar, A. Mansingh, Opt. Mater. **12** (1999) 53

[88] E.O. Serqueira, A. F. G. Monte, P. C. Morais, N.O. Dantas, J.Non-Cryst. Solids **352** (2006) 3642

[89] A. N. MacDonald, A. Hryciw, F. Lenz, A. Meldrum, Appl. Phys. Lett. **89** (2006) 173132

[90] K. Watanabe, H. Tamaoka, M. Fujii, K. Moriwaki, S. Hayashi, Physica E **13** (2002) 1038

[91] O. Debieu, D. Bréard, A. Podhorodecki, G. Zatryb, J. Misiewicz, C. Labbé, J. Cardin, F. Gourbilleau, J. Appl. Phys. **108** (2010) 113114

[92] S.-Y. Seo, M.-J. Kim, J.H. Shin, Appl. Phys. Lett. **83** (2003) 2778

[93]M. Roussel, E. Talbot, R. Pratibha Nalini, F. Gourbilleau, P. Pareige, Ultramicroscopy **132** (2013) 290

---

[94] R. Li, S. Yerci, S. O. Kucheyev, T. van Buuren, L. Dal Negro, Opt. Express **19** (2011) 5379

[95] F. Gourbilleau, D. Bréard, C. Dufour, R. Rizk, Opt. Mater. **31** (2009) 479

[96] D. Biggemann, L.R. Tessler, Mater. Sci. Eng. B **105** (2003) 188

[97] L. Rebohle, J. Lehmann, S. Prucnal, M. Helm, W. Skorupa, J. Lumin. **132** (2012) 3151

[98] L. R. Tessler, D. Biggemann, Opt. Mater. **27** (2005) 769

Chapter 2 Experimental techniques and analytical methods

The NIMPH team has a recognized expertise in thin layers grown by Radio-frequency (RF) magnetron sputtering. In this work, undoped- and doped- SiO_x and SiN_x single layers have been fabricated and studied. This chapter describes the deposition technique as well as the characterization experiments used for analyzing the layers investigated.

2.1 Thin film fabrication

2.1.1 RF Magnetron Sputtering

RF magnetron sputtering was used to deposit Si-based thin films. This technique can be performed on both conducting and non-conducting targets, while the direct current (DC) magnetron sputtering concerns only conducting material. The targets used in this work are SiO_2, Si and Nd_2O_3.

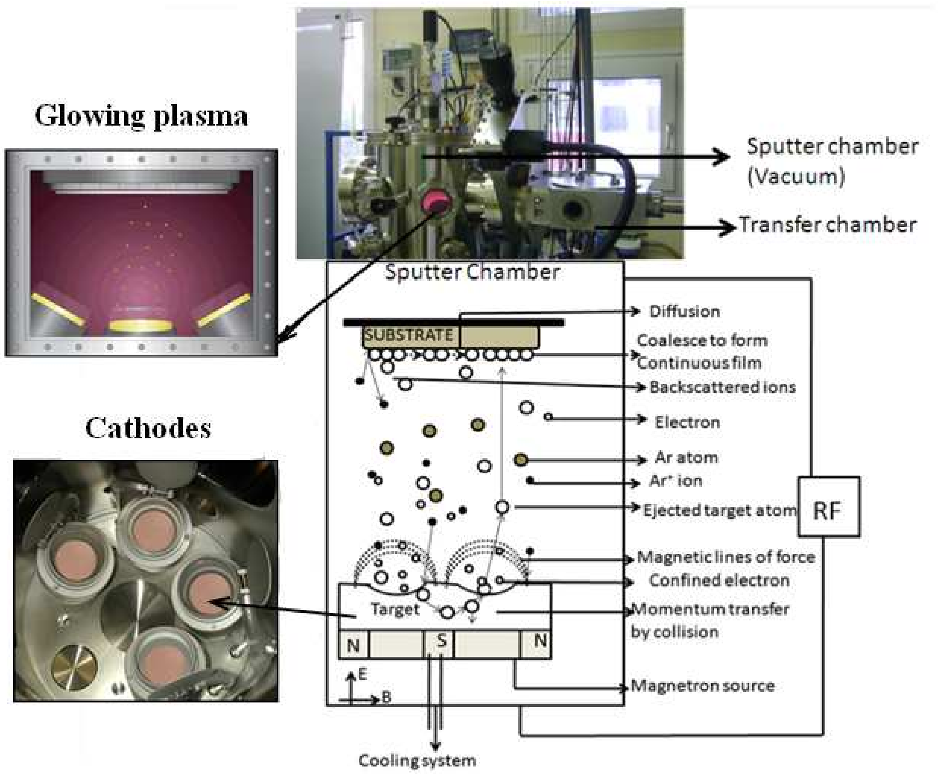

Figure 2.1: Diagram of the AJA Sputtering chamber with cathodes, glowing plasma, and the diagrammatic representation of various processes during sputtering.

(a) Principle

The phenomena of sputtering consist of striking the source material (the target) with ions from ionized gas such as Ar ions. Since these ions are in motion in the plasma, they are able to transfer a part of their momentum to the target species (eg. electron, atoms, molecular) and consequently ejected out some of them. The positive ions of the plasma are accelerated towards the negatively charged target and collide on its surface. Some of the bombarding ions are reflected back and are neutralized, while some have sufficient energy to reach the substrate and are back scattered. Electrons are trapped by magnetic field above the targets surface as shown in figure 2.1. These trapped electrons enhance the probability of ionizing a neutral gas (Ar) molecule by several orders of magnitude, and thus significantly increase the rate at which targets materials are stricken. Moreover, secondary electrons are also emitted and may lead to further ionization of the neutralized species. Due to the law of conservation of energy, when these electrons return to ground state, the energy gained by the neutral gas atom is released as photons which keep the plasma glowing. The main goal of sputtering is to direct the ejected species towards the substrate with sufficient energy and mobility. Indeed, if they collide with other atoms in the plasma, the energy is diminished and their path is then modified. Some incident species join other species at the substrate interface, diffuse and/or coalesce to form a continuous film[1]. The mobility of the incident atoms arriving at the substrate is highly dependent on sputtering parameters such as the RF power density applied, plasma pressure, substrate temperature, distance between the target and the substrate etc...

(b) Experimental conditions

The used deposition setup is AJA Orion 5 UHV sputtering unit from AJA international[2] which has multiple magnetron sputtering sources. Such sources are arranged in a specific circular pattern and their axis of symmetry is converging at the same common focal point (confocal sputtering). The magnetron sources of materials are called targets and are located separately in the chamber (four cathodes as shown in Fig. 2.1). Various RF power densities with a maximum of 15.2 W.cm^{-2} are applied independently to the targets in order to tune the composition of the deposited layer. Si and/or transparent silica used as substrate are fixed on a sample holder located at the focus position and rotate to grow a homogeneous film. By means of two halogen lamps placed on the rear side of this holder, substrate can be heated from ambient to

850°C during the deposition. The pressure in the chamber is maintained as low as 10^{-7}-10^{-8} mTorr using the couple primary-turbomolecular pumps. To launch the plasma, a higher pressure of about 30 mTorr as well as a minimum RF power density of 3 W.cm^{-2} is required during few seconds. Pure Ar gas is used for the classical sputtering process while for reactive approach, reactive gas(es) such as H_2, N_2 and/or O_2 is(are) added in the plasma.

- *Reactive co-sputtering*

We name reactive co-sputtering approach when the chemical nature of the growing film is different from the one of the target.

In this work, the total gas flow is fixed at 10 standard cubic cm/min (sccm) while the ratio of the gas flow between the reactive gas and Ar is varied. The reactive gas rate (r_g) can thus be defined (equation 2.1):

$$r_g(\%) = [p_g / (p_g + p_{Ar})] \times 100\% \qquad (2.1)$$

where p_g and p_{Ar} are the partial pressures achieved for reactive and Ar gases, respectively. Such an approach permits to tune easily the composition of the layer by simply varying r_g.

- Nd-doped SRSO films

Nd-doped SRSO films are obtained by sputtering SiO_2 and Nd_2O_3 targets in a reactive Ar/H_2 plasma. H_2 gas has the ability to reduce the oxygen-rich species coming from the sputtering of oxide targets. As a consequence, the increase of the hydrogen rate (r_H) would enhance the Si excess incorporated into the layers but to the detriment of the deposition rate[3]. This has been attributed to an etching process of the deposited layer by the hydrogen species present in the plasma. Considering the previous work performed with this deposition setup on similar layers (Er-SRSO)[4], the fabrication parameters such as plasma pressure (p_{pls}), substrate temperature (T_s), substrate rotation speed, and the RF power density applied onto SiO_2 (RFP_{SiO2}) and Nd_2O_3 (RFP_{Nd2O3}) cathodes were fixed at 3 mTorr, 100°C, 20 rev.min^{-1}, 7.4 and 0.45 W.cm^{-2}, respectively. We decide to vary the r_H parameter in the 40-80% range by step of 10%.

- Nd-doped SRSN films

In the case of Nd-doped SRSN films, Si and Nd_2O_3 targets have been sputtered in Ar/N_2 plasma. Contrarily to the previous case, there is no reduction process in the plasma, but a reaction of N_2 gas with Si species to form the silicon nitride film. The RF power density applied on the Si target (RFP_{Si}) and the nitrogen rate (r_N) permit to tune the Si excess. According to the works done on SRSN films deposited in our group[5], the p_{pls}, T_s, substrate rotation speed, and RFP_{Si} were set at 2 mTorr, 200°C, 20 $rev.min^{-1}$, 4.5 $W.cm^{-2}$, respectively, while RFP_{Nd2O3} was varied from 0.30 to 0.60 $W.cm^{-2}$. The r_N value was adjusted between 7.0 and 13.3% to engineer the layer composition. Note that due to the oxide target of rare earth used, Rutherford Backscattering Spectroscopy (RBS) experiment evidences the presence of oxygen in the deposited layer.

➢ Classical co-sputtering

For this approach, only pure Ar plasma is used. The composition of the layer is dependent on the RF power density applied on each target.

- Nd-doped SRSO films

The Nd-doped SRSO films were deposited by simultaneously sputtering SiO_2, Si and Nd_2O_3 targets. On the basis of investigations performed on a similar Er-SRSO system in our group[6], p_{pls}, T_s and rotation speed were chosen at 3 mTorr, 500°C, and 20 $rev.min^{-1}$, respectively. RFP_{SiO2} was kept at 8.88 $W.cm^{-2}$, while RFP_{Si} and RFP_{Nd2O3} were varied in the range of 0.89-1.78 $W.cm^{-2}$ and 0.30-0.90 $W.cm^{-2}$, respectively.

- Nd-doped SRSN films

The Nd-doped SRSN films were deposited by simultaneously sputtering Si_3N_4, Si and Nd_2O_3 targets. p_{pls}, T_s, substrate rotation speed, and RFP_{Si3N4} and RFP_{Nd2O3} were fixed at 3 mTorr, 500°C, 20 $rev.min^{-1}$, 7.4 and 0.45 $W.cm^{-2}$, respectively, while RFP_{Si} was varied in the range of 0.45-1.78 $W.cm^{-2}$. Since we have not observed any emission from Nd^{3+} ions in the films grown, such an approach will not be presented in the following.

2.1.2 Annealing

The objectives of the annealing process are to (i) favor the phase separation between Si and either SiO_2 or Si_3N_4 in the SiO_x and SiN_x films, respectively, (ii) provide the required energy to form and grow Si-nps in these matrices, and (iii) recover the non-radiative defects (vacancy, dangling bonds) that could quench the photoluminescence of our samples. In this work, two annealing approaches will be concerned: classical annealing (CA) and rapid thermal annealing (RTA). Both can be described by a four steps S1 to S4 time process (Fig. 2.2) detailed in table 2.1.

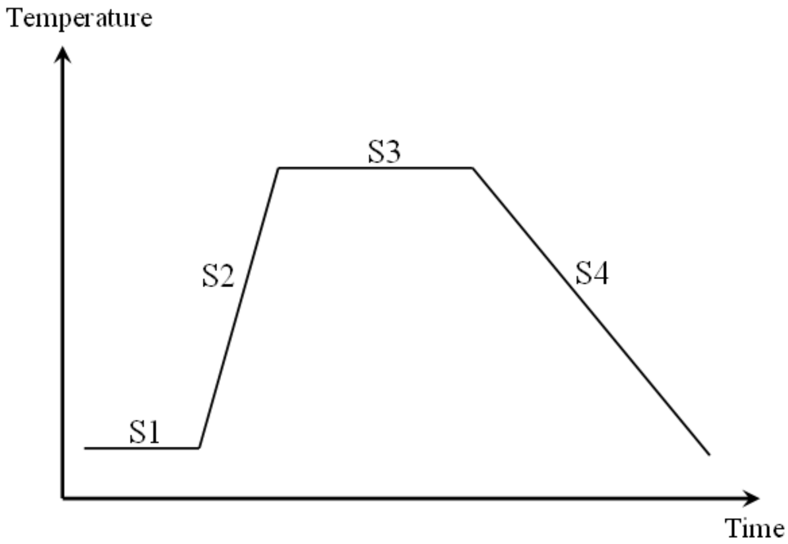

Figure 2.2: Schematic diagram of the annealing process.

	S1		S2		S3			S4
	P (mTorr)	Gas	Rising time	Rising rate	T_A (°C)	t_A	Pressure	
CA	15	N_2 flow during 15 min	90 s	2-12°C.s^{-1}	200-1100	1 h	P=37 mTorr	Natural cooling
			N_2 gas flow					
RTA	15	3 times alternating pumping and N_2 flow	Depending on T_A	45°C.s^{-1}	200-1200	1 min	Room pressure	Forced cooling (water system)
			N_2 gas (zero flow)					

Table 2.1: Parameters of CA and RTA in four steps.

For CA approach, the furnace is firstly heated to the required annealing temperature (T_A) in the S1 step under 15 mTorr pressure by primary pump. Then, a N_2 flow is applied during 15 min to lower the oxygen content in the furnace. In the S2 part, the samples are transferred into the heating area. This transfer time is fixed by the motorization of the system and takes 90 s. This leads to a rising rate in range of 2-12°C.s^{-1} depending on the fixed T_A. In S3 step, the samples undergo annealing process during 1 hour under 37 mTorr at T_A ranging from 200 to 1100°C. In S4 step, the samples are moved out and naturally cooled under N_2. All along the process, the 48 sccm N_2 gas is continuously flowing under a primary pumping.

In the case of RTA approach, in S1 step, the samples are firstly put into the furnace at room temperature. Then the furnace is pumped to about 15 mTorr pressure followed by inserting N_2 gas till the pressure rises up to room pressure. This step is repeated three times to lower the oxygen content from the furnace chamber. In S2 part, the heating lamps are switch on with a temperature rising rate of 45°C.s^{-1}. In S3 step, the samples stay at the temperature during 1 min duration. In S4 step, the lamp is turned off and the furnace chamber is cooled by water flow. Consequently, samples staying inside are submitted to a forced cooling. The temperature cooling rate is faster than that of CA method. During the S2, S3, and S4 steps, the N_2 gas is not renewed to avoid any inhomogeneous annealing effect due to the gas flow on the surface of the samples.

2.2 Sample characterization

2.2.1 Fourier transform infrared spectroscopy

(a) Principle

Fourier transform infrared (FTIR) spectroscopy is a characterization tool allowing to investigate the chemical bonds present in molecule. This technique relies on the principle that the vibrations of chemical bonds absorb specific frequency of electromagnetic waves ranging from 10 to 12000 cm^{-1}. These unique frequency absorptions result in a characteristic spectral profile for a given molecule. The bond vibration can be categorized in: stretching (symmetric and asymmetric), wagging, rocking, twisting, and scissoring modes as shown in figure 2.3.

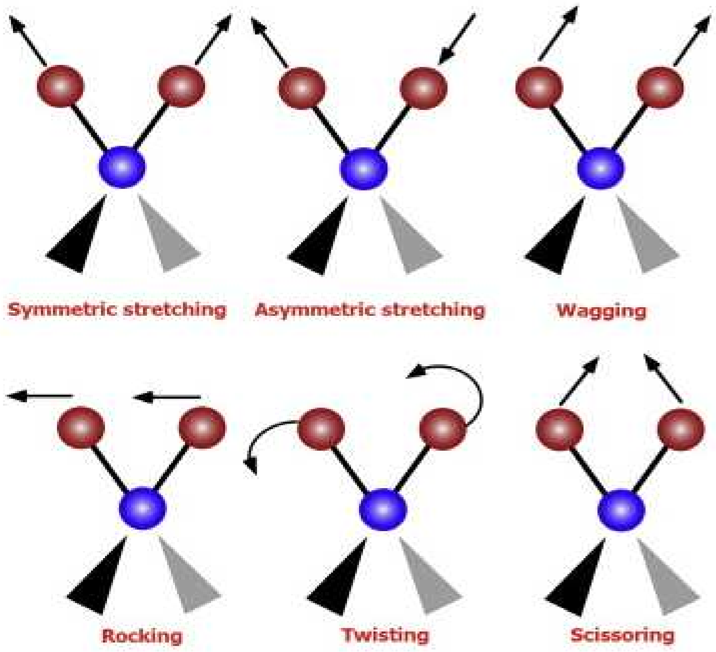

Figure 2.3: Different vibration types for chemical bonds.

(b) Experimental conditions

The setup named Thermo Nicolet Nexus 750 was used to record the FTIR spectra in 400-4000 cm^{-1} range with a resolution of 1 cm^{-1} at room temperature. The apparatus is equipped with two light sources: He-Ne laser (633 nm) used for alignment and a tungsten lamp generating light between 2.5-25 μm which interacts with the sample inserted in a Michelson's interferometer. By moving one mirror of the interferometer, the optical path is changed leading to an interferogram of transmitted intensity versus optical path (in m). Its Fourier transform leads to an interferogram into the spatial frequency domain (in cm^{-1}). The FTIR spectrum of the sample is obtained after subtracting the contribution of reference substrate and atmosphere components such as CO_2 and H_2O. After placing the sample on the angle-controlled sample holder, the chamber is closed and purged continuously with N_2.

(c) Determination of the Si excess

- In SiO_2

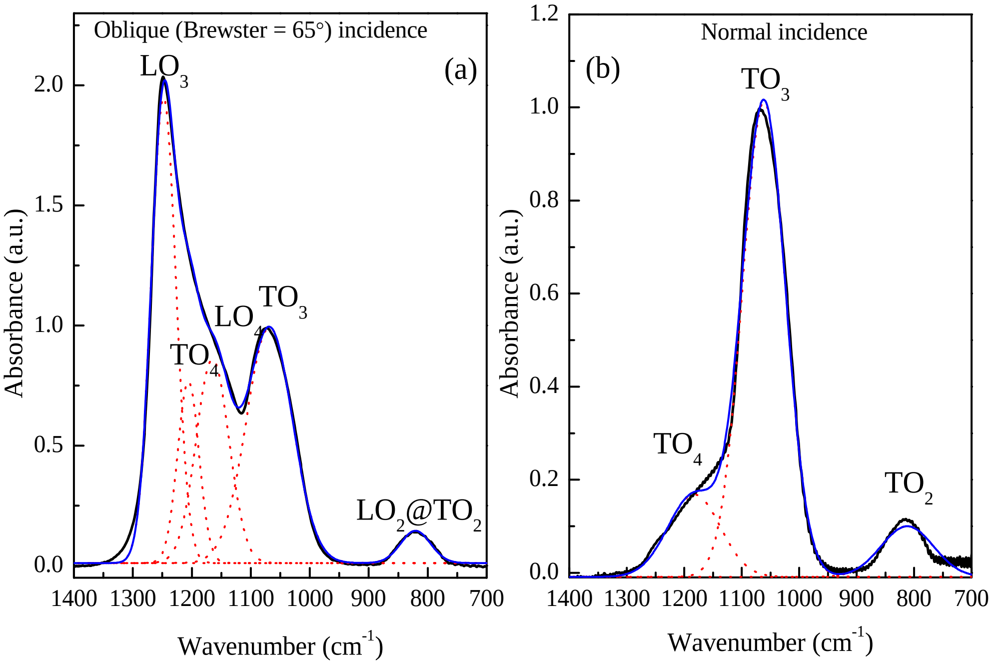

Figure 2.4: FTIR spectra of as-deposited SiO2 film which are decomposed into six Gaussians at Brewster incidence (a) and three Gaussians at normal incidence (b). Black line is experimental curve, and blue line is the result of superimposition of the Gaussian curves.

Two kinds of spectra are recorded (Fig. 2.4): at the Brewster angle (65°) or at the normal incidence. For the former, p-polarized light is totally transmitted through the film while s-polarized light is totally reflected[7]. This measurement is sensitive to both vibration components, the transverse optical mode (parallel) and the longitudinal optical mode (perpendicular) to the thin film surface. For the latter, light is transmitted through the layer with an electric field vector parallel to the film surface resulting in the selective excitation of the transverse optical mode (TO), the longitudinal optical mode (LO) remaining unexcited. Taking the as-deposited SiO_2 film as an example, the FTIR spectra in Brewster and normal incidence are shown in figure 2.4 (a) and (b), respectively. As observed, the Brewster incidence spectrum includes both LO and TO mode with total six Gaussians peaks from the vibration of Si-O bonds, while only TO mode with three Gaussians peaks are present in normal incidence spectrum. The LO_4, LO_3, LO_2 are located at about 1170, 1256, and 820 cm^{-1} while TO_4, TO_3, TO_2 at 1200, 1060, and 820 cm^{-1}, respectively.

The positions of the vibration modes are influenced by the composition of the layer. For example in SRSO layers, the position of TO_3 peak blue shifts proportionally with the increase of Si excess. Consequently, the Si/O ratio (x) can be estimated by the TO_3 wave-number (w_{TO3}) according to the equation[8] :

$$x = 0.02 w_{TO_3} - 19.3 . \tag{2.2}$$

Using the obtained x value, the atomic percentage of Si excess is estimated via the formulae:

$$Si_{ex}(at\%) = [(2-x)/(2+2x)]\times 100\% . \tag{2.3}$$

- In Si_3N_4

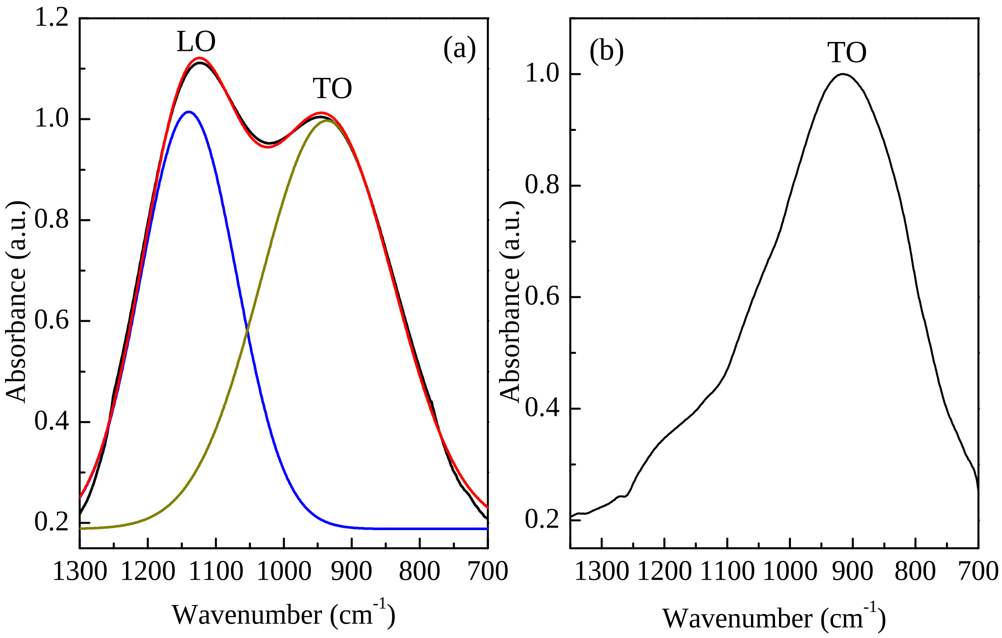

Figure 2.5: FTIR spectra of as-deposited silicon nitride film measured (a) with an incidence angle of 65° and (b) with a normal incidence. Black line is experiment curve, and red line is the result of superimposition of the Gaussian curves.

Similarly to the case of SiO_2, two kinds of spectra are obtained in figure 2.5 for silicon nitride film when measuring with an incidence angle of 65° and with a normal incidence. For the former, one can observe two absorption bands centered at about 1140 and 930 cm^{-1}. They are respectively assigned to the longitudinal (LO) and transverse (TO) modes of the Si-N stretching vibration[9]. For the latter, several bands are observed but their maxima can not be separate easily. We consider only single absorption band, as seen, which is centered at about 930 cm^{-1}. This is comparable to the position of TO mode for Si-N vibration.

It has been well demonstrated that a model based on linear combination of weighted bonding density may explained the FTIR peak position and consequently allow one to determine the layer composition [10]. The TO peak, as mentioned by Debieu et al.[5], is less sensitivity to the change of SRSN layer composition, while the LO band (w_{LO}) is a better indicator of N/Si ratio (x). Its relationship is denoted below:[5]

$$w_{LO} = 323.4(x - 4/3) + 1197 . \tag{2.4}$$

And the Si excess is calculated:

$$Si_{ex}(at\%) = [(4-3x)/(4+4x)] \times 100\% . \tag{2.5}$$

It is worth to note that the Si excess obtained from FTIR would not contain the Si atoms that have started nucleating or agglomerating during the deposition process. This is due to the inactivity to IR radiations for homopolar bonds. Therefore, the Si excess obtained from FTIR is an underestimation of the total excess present in the material.

The intensity of bond vibration could also be used for having information on layer composition. In SRSO films, the Si-np density can be reflected from the intensity of LO_3 peak attributed to the Si-O-Si bonds at 180° at SiO_x/Si-np interface[11]. In SRSN case, Debieu et al.[5] have observed a gradual decrease of Si-N LO band intensity with increasing Si excess. In both kinds of layers, the intensities of overlap between LO and TO are related to the layer ordering degree: a lower intensity means a more ordered microstructure.

2.2.2 Spectroscopic ellipsometry

(a) Principle

Spectroscopic ellipsometry is a fast, sensitive, and non-destructive tool to characterize the dielectric properties of thin film having a thickness ranging from nanometers to about 50 μm taking into account that the accuracy decreases with the thickness. The electric field E_i of the incident light can be split into two components (Fig. 2.6): one p-polarized light parallel to the incident plane (E_{ip}) and the other s-polarized perpendicular (E_{is}). The reflected fields of s- and p- components (E_{rp} and E_{rs}) are recorded after interacting with the sample. The reflection coefficients can be deduced from equation 2.6:

$$\mathrm{r}_p = E_{rp}/E_{ip}\,;\mathrm{r}_s = E_{rs}/E_{is}\ . \tag{2.6}$$

The reflection coefficients are mainly dependant on the film thickness and optical constants (refractive index, n, and extinction coefficient, k). Their ratio, known as ellipsometric function, is conventionally written as:

$$r_p/r_s = (\tan\Psi)\times\exp(i\Delta) \tag{2.7}$$

where ψ and Δ are the ellipsometric angles (Fig. 2.6). Since the refractive index is the square root of the relative permittivity which governs the interaction between light and the material under investigation. This index evolves with light energy witnessing the different features of light matter interaction (absorption, transmission, wave velocity, band gap…). Thus one can deduce from the measurements the film thickness, optical dielectric constants as a function of energy. The surface roughness and porosity of the film can also be estimated.

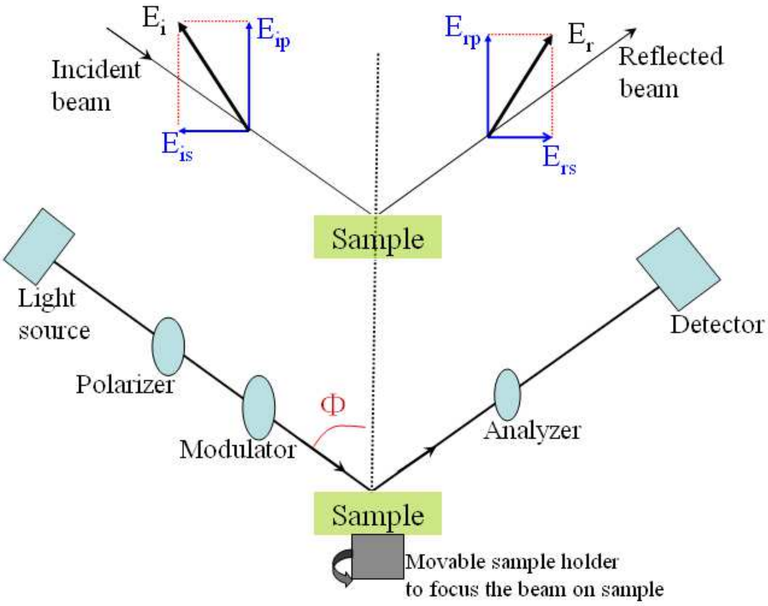

Figure 2.6: Schematic diagram of the principle and experimental setup for an ellipsometer.

(b) Experimental conditions

The experimental measurements are performed on Jobin-Yvon ellipsometer. The ellipsometry setup as shown in figure 2.6 contains:

- an unpolarized light source with a broad spectral range (Xenon lamp),
- a polarizer,
- a phase modulator which dephases the parallel and perpendicular components of the electric field,
- the sample holder,
- an analyzer and a detector consisting of monochromator and a photomultiplier tube.

The incident light is emitted from the Xenon lamp. When passing through the polarizer operated at a fixed angle of 45º, the light is linearly polarized with both polarization components s and p approximately equal. A quartz modulator fixed at normal incidence, phase modulates the linearly polarized beam. At an incidence angle of Φ=66.2°, this beam in 1.5-4.5 eV range with a resolution of 0.01 eV interacts with the sample (Si substrate with the dielectric layer, in our case). After reaching the layer, the light is reflected with a reflected angle equal to incidence one and passes through a rotating analyzer operating at 45°. This latter transmits the s and p polarization reflected wave to the photodetector which records the intensity of each of them. The incoming wave is phase modulated at 50 kHz allowing the use of lock-in detection system for increasing signal/noise ratio and to have reflectance measurements amplitude independent to wavelengths. At each wavelength the complex reflectance ratio $\rho=r_p/r_s=\tan(\psi)e^{(i\Delta)}$ is recorded. Those ellipsometric angles ψ and Δ are used in the modeling method in order to determine the complex refractive index dispersion and thickness of sample. It is to note that the ellipsometer is controlled by ELLI42 program provided by Horiba Jobin-Yvon SAS Company.

(c) Spectra modeling

The film thickness, optical dielectric constants, the surface roughness... can not directly be obtained from the recorded spectra. It requires a use of a modeling process which performs fitting, provides dispersion models and samples structural model. In our system, one of the most used dispersion model of refractive index (n) and extinction coefficient (*k*) is the New Amorphous or Forouhi-Bloomer formula[12] given in the following relations:

$$n(\omega) = n_{\infty} + (B(\omega-\omega_j)+C)\big/((\omega-\omega_j)^2+\Gamma_j^2)\,, \tag{2.8}$$

$$k(\omega) = (f(\omega-\omega_g)^2)\big/((\omega-\omega_j)^2+\Gamma_j^2)\,, \tag{2.9}$$

$$k(\omega) = 0 \text{ if } \omega \le \omega_j\,, \tag{2.10}$$

where $B = (f_j/\Gamma_j)(\Gamma_J^2-(\omega-\omega_j)^2)\,,$ (2.11)

$$C = 2f_j\Gamma_j(\omega-\omega_j)\,, \tag{2.12}$$

where n_∞ is the refractive index when energy tends to infinite, ω is the wave energy in eV, f_j is the oscillator strength (the fraction of electrons that oscillate at resonant energy ω_j), Γ_j is the damping coefficient that gives rise to the phenomena of optical absorption. From the extinction coefficient (*k*) one can obtain the absorption coefficient (α) by the following relation:

$$\alpha = 4\pi k/\lambda = 4\pi kw/hc\,, \tag{2.13}$$

where h is the Planck's constant and c the light velocity.

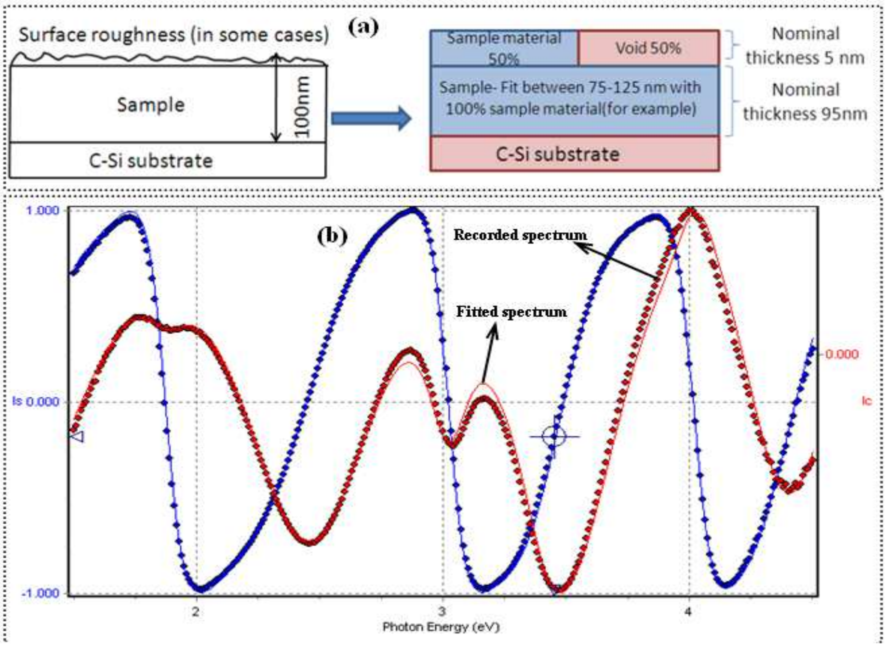

Figure 2.7: (a) Schematic illustration of the film structure and (b) the recorded spectra (square) with their fitting curves (line).

After choosing dispersion law for film and substrate, a sample structural model is required to before performing the fitting process (Fig. 2.7 (a)). Such a model takes into account the use of crystalline Si substrate, the possible roughness on layer surface, the presence of porosity in the film, interface roughness of substrate/film, ...

Thereafter, the recorded spectra (Fig. 2.7 (b)) were fitted through DeltaPsi software provided by Horiba Jobin-Yvon SAS Company and resulting fitted spectra were obtained by least-square method. One can thus deduce the optical constants (Fig. 2.8) including the layer thickness.

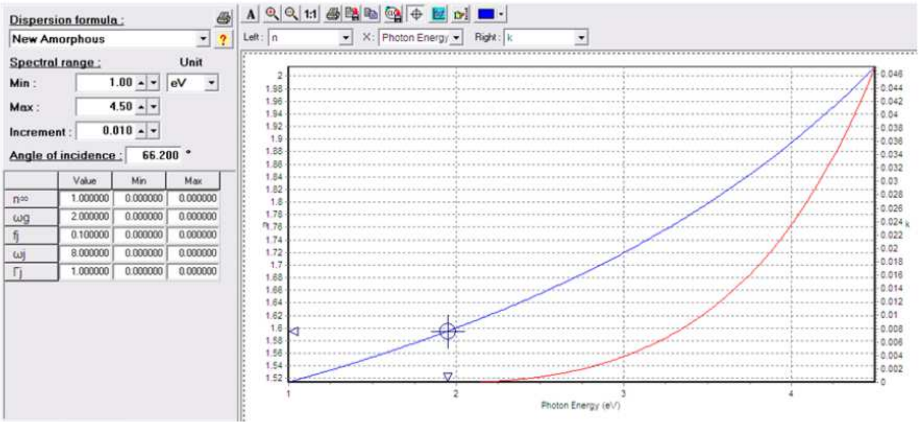

Dispersion formula : New Amorphous

Spectral range : Unit eV

Min : 1.00

Max : 4.50

Increment : 0.010

Angle of incidence : 66.200 °

	Value	Min	Max
$n\infty$	1.000000	0.000000	0.000000
ωg	2.000000	0.000000	0.000000
fj	0.100000	0.000000	0.000000
ωj	8.000000	0.000000	0.000000
Γj	1.000000	0.000000	0.000000

Left : n

X : Photon Energy

Right : k

Figure 2.8: Optical properties versus incident photon energy.

(d) Determination of the Si excess

In order to determine the fraction of Si excess in the layers, the effective medium approximation (EMA) is used assuming that the studied film is a homogeneous medium with respect to the wavelength size. The EMA model can be performed by the used of several models, such as Bruggeman model[13], Maxwell-Garnet model[14]. EMA is a mean field theory assuming that "light" sees an effective medium constituted of media with different permittivities. It succeeds to predict optical properties of multiphase medium in a low concentration regime (below the percolation threshold)[15]. The Bruggeman effective medium approximation (BEMA) used in this work is defined by the following two equations:

$$\sum_i v_i((\varepsilon_i - \varepsilon)/(\varepsilon_i + 2\varepsilon)) = 0\,, \tag{2.14}$$

$$\sum_i v_i = 1\,, \tag{2.15}$$

where ε_i and v_i are the complex optical dielectric function and volume fraction for the i component, respectively. ε is the effective dielectric function corresponding to the measured value for the film. In the following parts, we describe the determination of Si component in both matrices: SiO_2 and Si_3N_4.

- In SiO_2

In SRSO materials, the effective dielectric function (ε_e) is a combination of the dielectric function of Si and SiO_2. The Bruggeman model gives a relationship of the effective medium as a volume fraction of two different materials as below:

$$f_{Si}((\varepsilon_{Si}-\varepsilon_e)/(\varepsilon_{Si}+2\varepsilon_e))+f_{SiO_2}((\varepsilon_{SiO_2}-\varepsilon_e)/(\varepsilon_{SiO_2}+2\varepsilon_e))=0\,. \tag{2.16}$$

where, ε_e is the relative permittivity of the effective medium, ε_{Si} and ε_{SiO2} are the relative permittivities of Si and SiO_2 respectively, and f_{Si} and f_{SiO2} their volume fractions (f_{Si} + f_{SiO2} = 1). Furthermore, the permittivity equals to the square of complex refractive index: $\varepsilon=\tilde{n}^2=(n-ik)^2$, where n is the refractive index measured by ellipsometry at 1.95 eV. At this energy, the values of the absorption coefficient k are negligible whatever the composition of the layer. Thus, the O/Si ratio (x) can be estimated by knowing the refractive index from ellipsometry, concentration and volume fractions of the chemical species. The concentration of an element in a material can be estimated from the density d, molar mass M, and Avogadro number N. This leads to the following expression, which results in the values indicated in table 2.2:

$$[Si]_{Si}=N\,d_{Si}/M_{Si}\,,[Si]_{SiO_2}=N\,d_{SiO_2}/M_{SiO_2}\,,[O]_{SiO_2}=2N\,d_{SiO_2}/M_{SiO_2}\,. \tag{2.17}$$

Element x	Matrix y	Density d (g.cm^{-3})	Molar Mass M (g)	$[x]_y$ (cm^{-3})
Si	Si	2.59	28.09	5.0×10^{22}
Si	SiO_2	2.27	60.09	2.25×10^{22}
O	SiO_2	2.27	60.09	4.5×10^{22}

Table 2.2: Estimation of atomic concentration in SRSO materials.

Then the O/Si ratio (x) can be deduced by using the following equation:

$$x=(f_{SiO_2}[O]_{SiO_2})/(f_{Si}[Si]_{Si}+f_{SiO_2}[O]_{SiO_2})\,. \tag{2.18}$$

The values of n_{SiO2} and n_{Si} given at 1.95 eV are 1.457 ± 0.002 and 4.498 ± 0.002. Finally, following the equation (2.15) and (2.17), the O/Si ratio is obtained as a function of refractive index:

$$x=(-36n^4+691n^2+773)/(22n^4+665n^2-472)\,. \tag{2.19}$$

One can deduce the atomic percentage of Si excess using the formulae 2.3 as described in FTIR section.

- In Si_3N_4

In the case of SRSN layers, one also can consider the materials as a heterogeneous medium formed by a mixture of amorphous Si and Si_3N_4. In the same way as SRSO films, the concentration of an element in a material can be obtained and described in table 2.3[16]:

Element x	Matrix y	Density d ($g.cm^{-3}$)	Molar Mass M (g)	$[x]_y$ (cm^{-3})
Si	Si	2.59	28.09	5.0×10^{22}
Si	Si_3N_4	2.80	140.28	3.6×10^{22}
N	Si_3N_4	2.80	140.28	4.8×10^{22}

Table 2.3: Estimation of atomic concentration in SRSN materials.

The N/Si ratio (*x*) is achieved through the following function:

$$x = (-9.6n^4 + 177.6n^2 + 332.2)\big/(2.8n^4 + 200.2n^2 - 96.6)\cdot \tag{2.20}$$

Apart from this Bruggeman model, there is another approach concerned in this thesis to estimate the layer composition. Numerous groups[17], [18] have proposed that the refractive index n can be represented as the bonding-density-weighted linear combination with the N/Si ratio (*x*). Debieu et al.[5] have obtained a progressive increase of *x* value with increasing either p_{Ar}/p_{N2} or RFP_{Si}/RFP_{Si3N4} to deposit SRSN layers. They noticed that such an increase is also consistent with that of refractive index. Accordingly, these results support the empirical relation:

$$x = 4(n_{Si} - n_{SRSN})\big/3(n_{SRSN} + n_{Si} - 2n_{Si_3N_4}), \tag{2.21}$$

where the values of n_{Si} and n_{Si3N4} given at 1.95 eV are 4.498 ± 0.002 and 1.850 ± 0.002, respectively. Then, the Si excess can be calculated by the formulae 2.5 as described in FTIR section.

As a consequence, via ellipsometric experiments one can extract the information including (i) the refractive index of the layer from which the composition in terms of Si excess is estimated, (ii) the thickness of the film with an accuracy of high than 95%, and (iii) the absorption coefficient of the sample. It is worth to note that the Bruggeman calculations only account for the nucleated Si-nps, but do not consider the fraction of free unbounded Si atoms.

2.2.3 Raman spectroscopy

(a) Principle

Raman spectroscopy is a spectroscopic technique relied on light scattering by molecular vibration and phonons. This scattering is classified into two parts: elastic (Rayleigh) and inelastic (Raman and Brillouin) scattering. The re-radiative elastic part is eliminated because the corresponding wavelength is at the same wavelength than that of the excitation source. The inelastic scattering is due to interaction with optical and acoustical phonons, called Raman and Brillouin scattering respectively. This inelastic part would result in the down- (Stokes) or up- (anti-Stokes) shift in energy of a few photons. This technique is more sensitive to homopolar bonds.

(b) Experimental conditions

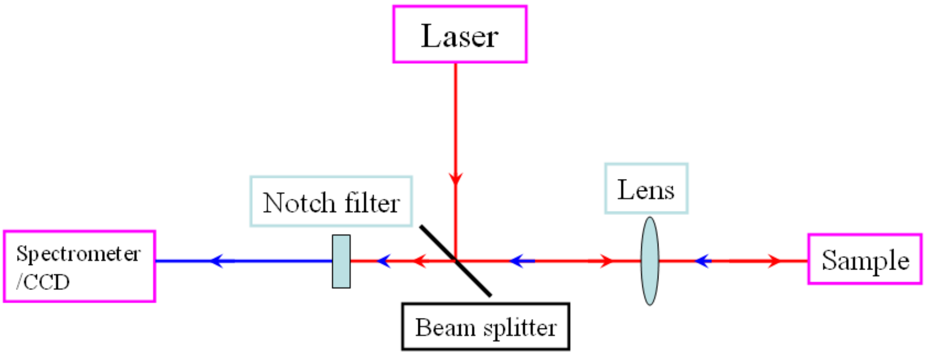

Figure 2.9: Schematic representation of Raman spectrometer.

A Raman system typically consists of several major components as shown in figure 2.9:

- Excitation source installed with two lasers: 532 and 632 nm,
- Beam splitter splitting a laser beam in two,
- Lens for focusing optics,
- Notch Filter,
- Monochromator plus detector (CCD).

The sample under investigation is illuminated with a laser beam. The elastic and inelastic scattering lights are collected with a lens and are sent through the beamsplitter. The notch filter will remove the elastic scattering light. The inelastic scattering light is dispersed through a Monochromator before being collected by CCD camera. The incident laser beam used for this work is the 532 nm line with a power density that can be tuned from 0.14 to 1.4 MW.cm^{-2}. The films were deposited on quartz substrate to permit RAMAN peak at 521 cm^{-1} observation. The figure 2.10 displays three typical Raman spectra of (i) amorphous Si-nps (orange curve), (ii) crystalline Si-nps (orange square), (iii) Si bulk (black curve). For the orange curve, two Raman peaks were recorded at about 150 and 480 cm^{-1} and are attributed to transverse acoustic (TA), and transverse optical (TO) phonon frequencies of amorphous Si-nps, respectively. The comparison between the black and the orange square curves evidences a vibration mode peaking at about 521 cm^{-1}. This is, for the orange square curve, the signature of the presence of crystalline Si-nps. One can notice that the background of Raman spectra is higher than the one of the Si wafer, due to the occurrence of photoluminescence from the layer. These emissions are centered at about 700 nm but with a broad shoulder. Similar PL emitting from 400 to 900 nm has been observed by Savchyn et al.[19] and have been attributing to luminescence centers (LCs). The authors have shown that the LCs peak intensity decreased after annealing at 1100°C. We also notice such a decrease after annealing (Fig. 2.10).

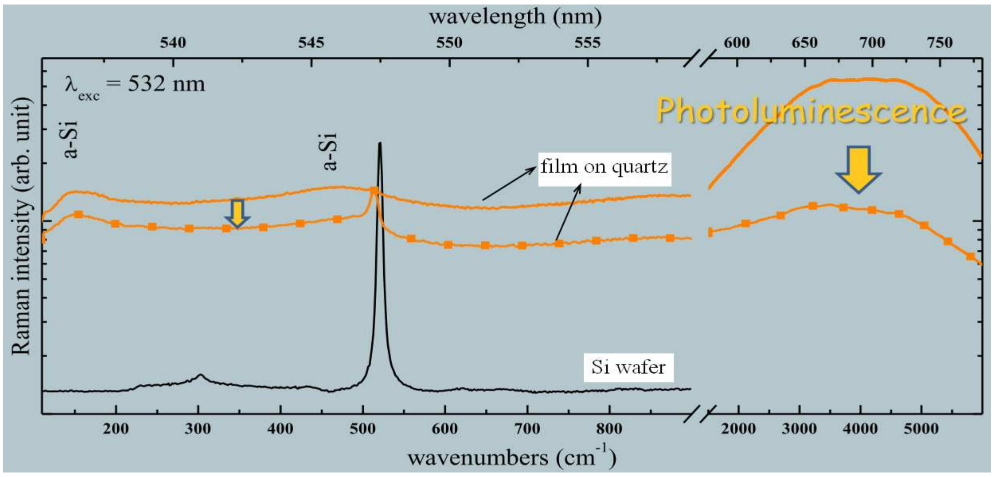

Figure 2.10: Raman spectra of Si wafer (black curve), 750°C-annealed (orange curve) and 1100°C-annealed (orange square) SRSN layers deposited on quartz.

Information extracted in this work contains: (i) the formation of some single phase witness by the presence of homopolar bonds; (ii) the change of peak intensity gives information on the volume of Si-nps phase.

2.2.4 Photoluminescence spectroscopy

(a) Principle

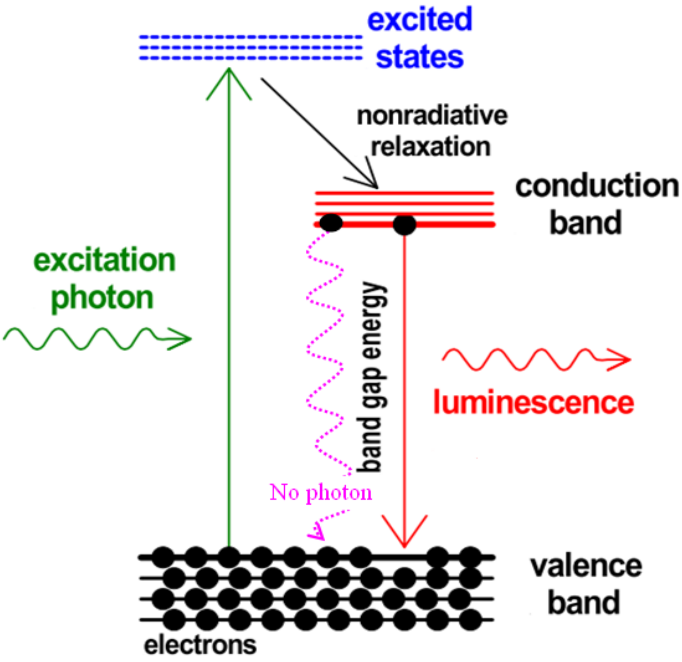

Figure 2.11: Illustration of excitation and de-excitation processes.

Photoluminescence spectroscopy is a non-destructive approach for the investigation on electronic structure of materials. It allows one to obtain important information about excitation, relaxation and emission mechanisms.

- Excitation mechanism: photons are absorbed by the materials leading to excite an electron from ground state to the allowed excited state. In the case of Si-nps, this excitation process occurs between the valence and the conduction bands. This step is characterized by a rise time (t_{rise}) which is photon flux and material dependant.
- Relaxation-emission mechanism: from this step, two processes can occur, i.e. a non-radiative or radiative relaxation. The former allows the electron to go back to the ground state by transferring its energy to the network of the materials by several processes (phonon, Auger…) while the latter is occurring with the emission of a photon. These two processes can be gathered as presented in figure 2.11. This step can be described by a decay time (t_{decay}) which takes into account the radiative and

non-radiative relaxations. The non-radiative process acts as a competition process to the PL one. It can be described as a sum of radiative rate (t_r^{-1}) and non-radiative (t_{nr}^{-1}) rates. The decay rate t_{decay}^{-1} of electrons from conduction to valence band can thus be expressed as

$$t_{decay}^{-1} = t_r^{-1} + t_{nr}^{-1}. \tag{2.22}$$

(b) Experimental conditions

Continuous Laser setup

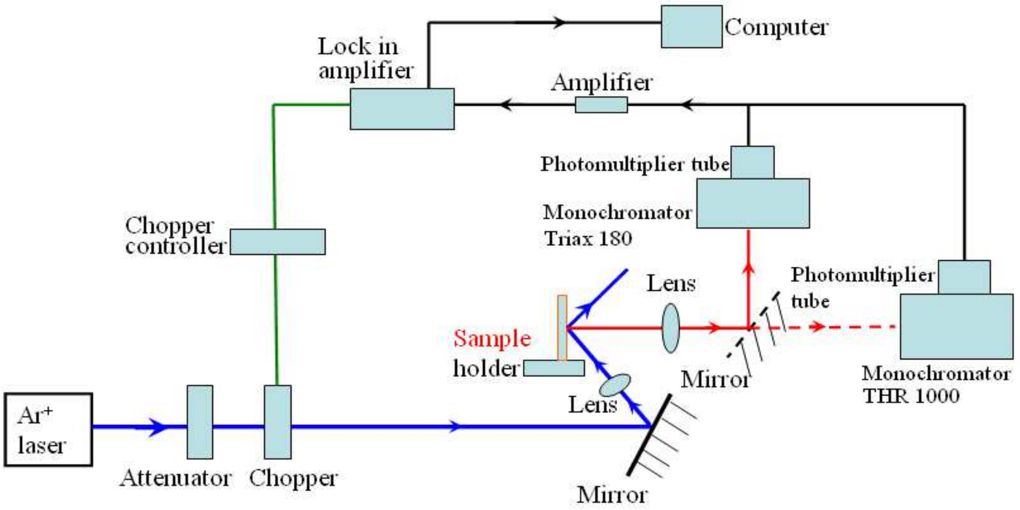

Figure 2.12: Schematic diagram of the continuous wave laser PL setup.

The schematic diagram of the PL setup used in our laboratory is shown in figure 2.12, which includes several components:

- Excitation light source using continuous wave Ar^+ laser,
- Optical tools such as attenuator, chopper, mirror, lens…
- Monochromator, and photomultiplier tube,
- Amplifier, and lock-in amplifier,
- Computer.

The wavelength of Ar^+ laser (INNOVA 90C) can be selected at 514, 488, 476, and 458 nm, while in this study, we used the wavelength of 488 nm which is non-resonant with Nd ions[20] to ensure that their excitation occurs indirectly via sensitizers. The laser beam was mechanically chopped at a fixed frequency (60 Hz). We used a sample holder that can accept five samples which are movable along an axis perpendicular to the optical axis of the detection system and parallel to the optical table. The laser beam is reflected and focused on the sample with an incident angle (45°) using appropriate optical mirrors and lenses. It has a fixed power 240 mW, and the focal spot surface (1.3 mm^2) on each sample remains the same. The light emitted by sample is partially collected through another set of lenses and is focused on the entrance slit of the monochromator. Two types of monochromators can be chosen: TRIAX 180 and THR 1000 from Horiba Jobin Yvon SAS. The collected light from sample is dispersed by the monochromator and detected by a photomultiplier tube. The TRIAX 180 is coupled to a visible wavelengths range sensitive detector sensitive to the wavelengths in visible range (HAMAMATSU R5108), while the THR 1000 is VIS-NIR connected to the extended photomultiplier tube for the visible to infrared range (HAMAMATSU R5509-72). Thereafter, the detected signal is amplified and converted into voltage by some transimpedance amplifier (Femto…). The signal consisting of all the detected frequencies is filtered by the lock-in amplifier, referenced to the chopper reference frequency. The selected signal is then recorded by computer as a function of monochromator selected wavelength to build a typical PL spectrum. With such a system, the minimum PL decay time measurable is about 1 ms. Considering that the Nd transition time is about 100 µs, we used pulsed-tunable laser setup suitable for the determination of this decay time in our films.

Pulsed tunable laser setup

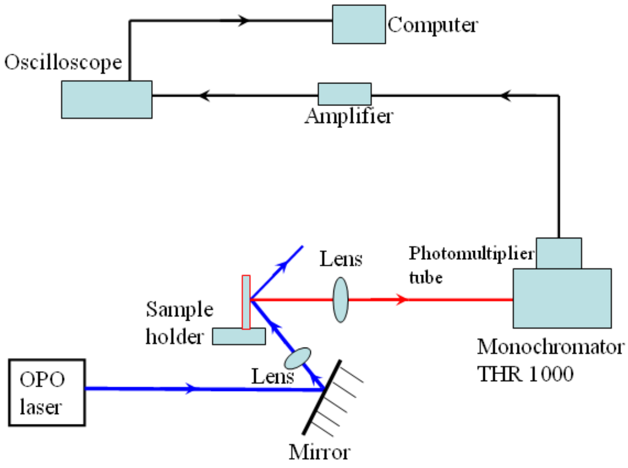

Figure 2.13: Schematic diagram of the pulsed tunable laser PL setup.

This PL setup shown in figure 2.13 includes several components:

- Excitation light source using optical parametric oscillator (OPO) laser,
- Optical tools such as mirror, lens…
- Monochromator, and photomultiplier tube,
- Amplifier, and oscilloscope,
- Computer.

The OPO laser (EKSPLA, NT340) used as excitation source has a pulse of 5 ns at full width at half maximum and a maximum repetition rate of 10 Hz for excitation wavelengths in 192-2600nm range. The 488nm-laser beam is focused on the sample with an incident angle (45°), a fixed energy of 15 mJ and a focal spot surface of 0.2 mm^2. The light emitted by sample is collected through a set of lenses and is focused on the entrance slit of the THR 1000 Horiba Jobin Yvon SAS monochromator. After being dispersed, the emitted light is detected by the VIS-NIR extended photomultiplier tube (HAMAMATSU R5509-72) and then amplified and converted into voltage. The full signal is acquired by an oscilloscope (TIEKTRONTCS TDS-3012B) having a bandwidth of 100 MHz (the time resolution is about some tenth of nanosecond) before being sent to the computer showing the PL decay curve as a function of time.

Bibliography

---

[1] A. Wagendristel and Y. Wang; in “An introduction to physics and technology of thin films” (World Scientific Publishing, Singapore), 1994

[2] http://www.ajaint.com

[3] C. Ternon, F. Gourbilleau, X. Portier, P. Voivenel, C. Dufour, Thin Solid Film, **419** (2002) 5

[4] L. Khomenkova, F. Gourbilleau, J. Cardin, R. Rizk, Physica E , **41** (2009) 1048

[5] O. Debieu, R. P. Nalini, J. Cardin, X. Portier, J. Perrière, F. Gourbilleau, Nanoscale Res. Lett. **8** (2013) 31

[6] S. Cueff, C. Labbé, J. Cardin, J. L. Doualan, L. Khomenkova, K. Hijazi, O. Debieu , B. Garrido, R. Rizk, J. Appl. Phys. **108** (2010) 113504.

[7] L. J. Webb, S. Rivillon, D. J. Michalak, Y.J. Chabal, N.S. Lewis, J. Phys. Chem. B **110** (2006) 7349

[8] B. J. Hinds, F. Wang, D. M. Wolfe, C. L. Hinkle, G. Lucovsky, J. Non-Cryst. Solids, **227** (1998) 507

[9] K. C. Lin, S. C. Lee, J. Appl. Phys. **72** (1992) 5474

[10] L. Huang, K.W. Hipps, J. T. Dickinson, U. Mazur, X. D. Wang, Thin solid films, **299** (1997) 104

[11] J. E. Olsen, F. Shimura, J. Appl. Phys. **66** (1989) 1353

[12] A. R. Forouhi, I. Bloomer, Phys. Rev. B **34** (1986) 7018

[13]http://www.mpiahd.mpg.de/homes/henning/Dust_opacities/Opacities/Ralf/Eff/rules.html

[14] http://en.wikipedia.org/wiki/Effective_medium_approximations

[15] L. Khomenkova, X. Portier, J. Cardin, F Gourbilleau, Nanotechnology **21** (2010) 285707

[16] E. Dehan, P. Temple-Boyer, R. Henda, J. J. Pedroviejo, E. Scheid, Thin Solid Films **266** (1995)14

[17] E. Bustarret, M. Besouda, S. C. Gujrthi, Phys. Rev. B **38** (1988) 8171

[18] S. Hasegawa, L. He, Y. Amano, T. Inokuma, Phys. Rev. B **48** (1993) 5315

[19] O. Savchyn, F. R. Ruhge, P. G. Kik, R. M. Todi, K. R. Coffey, H. Nukala, H. Heinrich, Phys. Rev. B **76** (2007) 195419

[20] D. Bréard, F. Gourbilleau, A. Belarouci, C. Dufour, R. Rizk, J. Lumin. **121** (2006) 209

Chapter 3: A study on Nd doped Si-rich silicon oxide films

3.1 Introduction

On the basis of the previous results achieved by Breard et al.[1], [2], the objectives of this chapter is to develop a confocal co-sputtering approach for growing Nd-doped SRSO films. Indeed, the technique used in this previous study was the co-sputtering of Nd_2O_3 chips placed on a pure SiO_2 target in a hydrogen-rich plasma. If relevant results were obtained during this prior work, the main drawback was the difficulty to control the Nd incorporation in the film. This is why in my work, one of the aims is to optimize the Nd^{3+} emission in Nd-SRSO films, i.e the coupling rate between Si-nps and Nd^{3+} ions, through an engineering of the films compositions in Si excess and Nd content. This optimization is limited by the presence of non-radiative channels in the layer. Consequently, a specific attention will be paid on the post-annealing treatment to ensure the quality of the surrounded host medium for significant decrease of the non-radiative channels contribution.

Two approaches have been investigated to reach these objectives. It concerns the reactive and classical co-sputtering processes. In the first case, we applied the parameters proposed by Khomenkova et al.[3] for the growth of similar films doped with Erbium ions for which an intense Er^{3+} PL emission at 1.54 μm has been obtained. The plasma pressure, substrate temperature and power densities applied onto SiO_2 and Nd_2O_3 cathodes were fixed at 3 mTorr, 100°C, 7.4 and 0.45 $W.cm^{-2}$, respectively. The incorporation of Si excess in the layers is based on the use of hydrogen-rich plasma in which hydrogen reduces the oxide species resulting from the sputtering of the targets. For the classical co-sputtering method, Hijazi et al.[4] have optimized the fabrication conditions for Er-doped layers using the three cathodes approach. The fixed parameters are the following: a plasma pressure of 3 mTorr, substrate temperature of 500°C, a RF power density (RFP_i) applied on SiO_2, Si, and Er_2O_3 cathodes of 8.88, 1.65 and 0.30 $W.cm^{-2}$, respectively. In the case of annealing treatment, rapid thermal annealing (RTA) and/or classical annealing (CA) have been carried out.

3.2 Effect of Si excess incorporated

Depending on the approaches, the Si excess has been monitored through:

- The hydrogen rate r_H varied from 40% to 80% in the case of the reactive deposition method,
- The RF power densities applied which have been studied in the 1.04-1.78 W.cm^{-2} range for the classical approach.

More details on these two deposition methods have been given in section 2.1.1 of chapter 2.

3.2.1 Fourier transform infrared spectroscopy

(a) Reactive co-sputtering approach

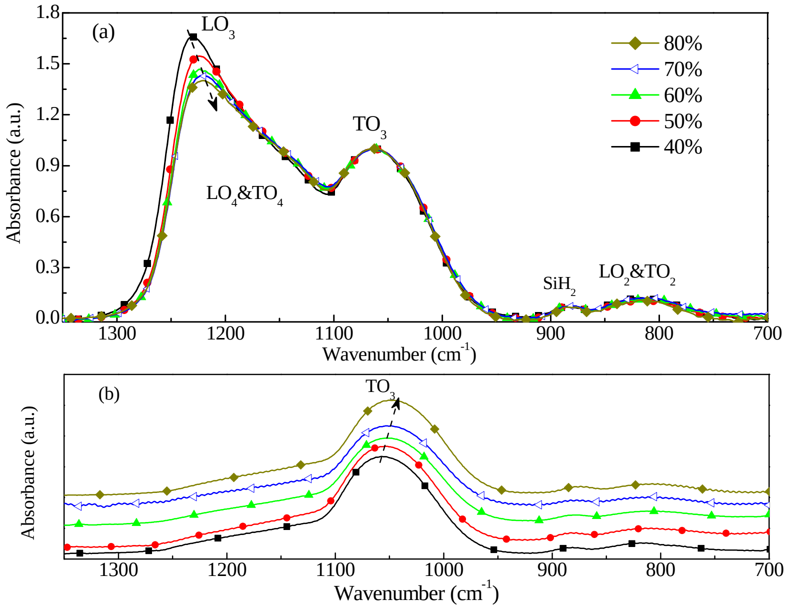

Figure 3.1: FTIR spectra of as-deposited Nd-SRSO layers recorded at (a) Brewster incidence and (b) normal incidence (all absorbance spectra are offset in perpendicular axis for clarity) – Effect of hydrogen rate r_H from 40% to 80% on the film structure.

Figure 3.1 shows the FTIR spectra of the as-deposited Nd-SRSO samples prepared by reactive sputtering by varying hydrogen rate r_H from 40% to 80%. These spectra have been recorded in (a) Brewster and (b) normal incidences. In figure 3.1(a), the spectra are normalized to the TO$_3$ band intensity. One can see that the intensity of

LO_3 peak in 1230-1220 cm^{-1} range gradually decreases with increasing r_H. Concomitantly, the peak position clearly shifts to low wavenumbers, similarly noticed by R. Nalini[5]. Considering that, LO_3 peak reflects the number of Si-O-Si bonds at 180° present at the Si/SiO_2 interface[6], the decrease of this longitudinal vibration mode intensity indicates a lowering of the total interface area with r_H. For the normal incidence acquired spectra (Fig. 3(b)), the TO_3 vibration mode shifts towards low wavenumbers with increasing r_H. This is a signature of the concomitant increase of Si incorporation allowing the achievement a Si excess ranging from 2.4 to 5.6 at.% as deduced from the TO_3 peak position (Sect. 2.2.1 Chap. 2). Thus, the evolution of the LO_3 mode with the hydrogen introduced in the plasma can be explained by the formation of larger Si-nps at the expense of their density. Moreover, this LO_3 peak evolution suggests that the Si-nps can be grown at 100°C during the deposition. The existence of the dihydride SiH_2 species is confirmed by the detection of its bending modes at around 885 cm^{-1}. This is the consequence of the use of hydrogen during the deposition process. These results demonstrate that the use of hydrogen rich plasma is an effective approach to monitor the Si excess.

(b) Classical co-sputtering approach

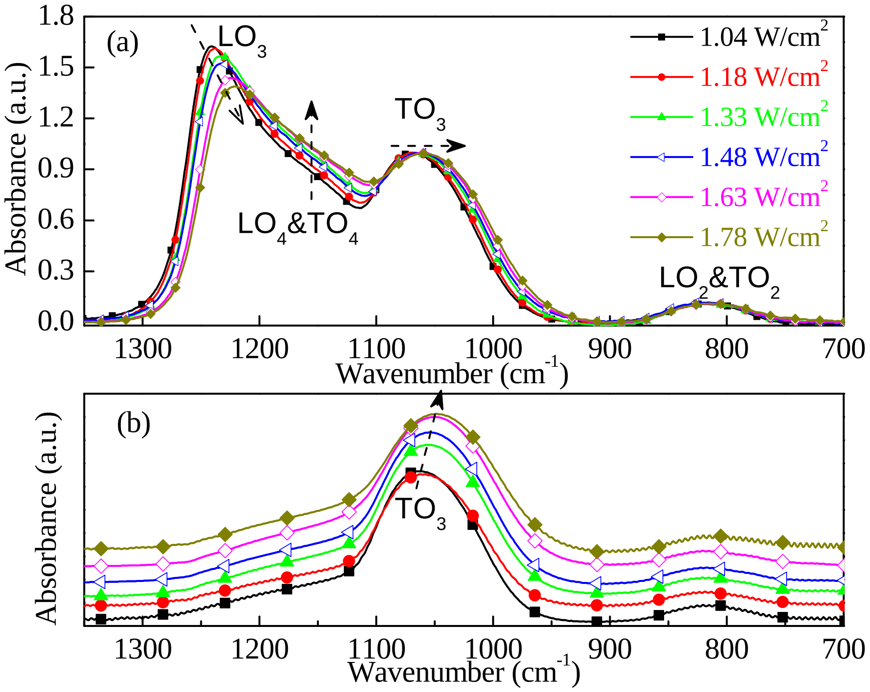

Figure 3.2: FTIR spectra of as-deposited samples recorded at (a) Brewster incidence and (b) normal incidence (all absorbance spectra are offset in perpendicular axis for clarity) – Effect of power density of Si cathode ranging from 1.04 to 1.78 W.cm^{-2} on the film structure.

Figures 3.2(a) and (b) show the FTIR graphs of the co-sputtered SRSO samples collected in Brewster and normal incidences respectively. In figure 3.2(a), all the spectra are normalized to the TO_3 band intensity. The increase of the RFP_{Si} leads to the decrease of the LO_3 peaks as well as to a shift towards low wavenumbers as denoted by the arrow. In addition, this evolution is followed by an increase of the disorder in the SiO_2 matrix (increase of the intensity of LO_4&TO_4 doublet). At normal incidence (Fig. 3.2(b)), the TO_3 peak position shifts towards low wavenumbers with increasing RFP_{Si}. The resulting Si excess determination reveals that this approach allows the incorporation of a higher Si content in the host matrix than in the reactive approach. Indeed, the values of Si excess are ranging from 1.4 to 6.8 at.% when RFP_{Si} is varying from 1.04 to 1.78 W.cm^{-2}. Considering the results described in the previous section, these observations are the signature of the formation of bigger Si-nps with increasing RFP_{Si}. Comparing to the first deposition method, the main difference in these spectra is the absence of the bending mode for Si-H bond at about 885 cm^{-1} since these samples were fabricated under pure Ar plasma.

3.2.2 Ellipsometry

(a) Reactive co-sputtering approach

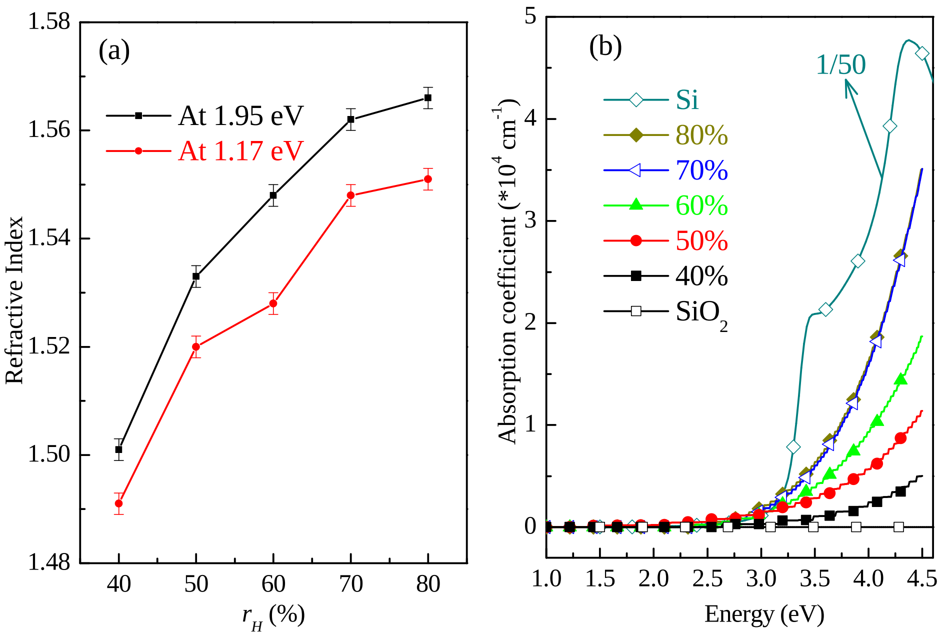

Figure 3.3: Evolutions of (a) refractive index with r_H and (b) absorption coefficient with energy for as-deposited layers for different r_H ranging from 40 to 80%.

The values of refractive index (n) and absorption coefficient (α) have been deduced from ellipsometry measurements (Sect. 2.2.2 Chap. 2). Figures 3.3(a) represents the refractive index evolution as a function of the hydrogen rate r_H for two energies, 1.17 and 1.95 eV. The value of n = 1.17 eV is here considered for the design of a single mode waveguide at the 1.06 μm wavelength (Sect. 5.2 Chap. 5). It is worth to note the raise of n with r_H until 70% and then the saturation of this refractive index when the hydrogen rate reaches about 80%. Such a result indicates that the maximum Si incorporation has been achieved by means of the fixed deposition parameters. Figure 3.3(b) displays the absorption coefficient of thin films versus energy from 1.0 to 4.5 eV for different hydrogen rates investigated, as well as for pure SiO_2 and Si. From 1.0 to 2.5 eV, α is lower than 10^3 cm^{-1} and increases from 10^3 to several 10^4 cm^{-1} for higher energies. All these curves are between those of SiO_2 and Si which is a confirmation of the increase of Si incorporation with r_H.

(b) Classical co-sputtering approach

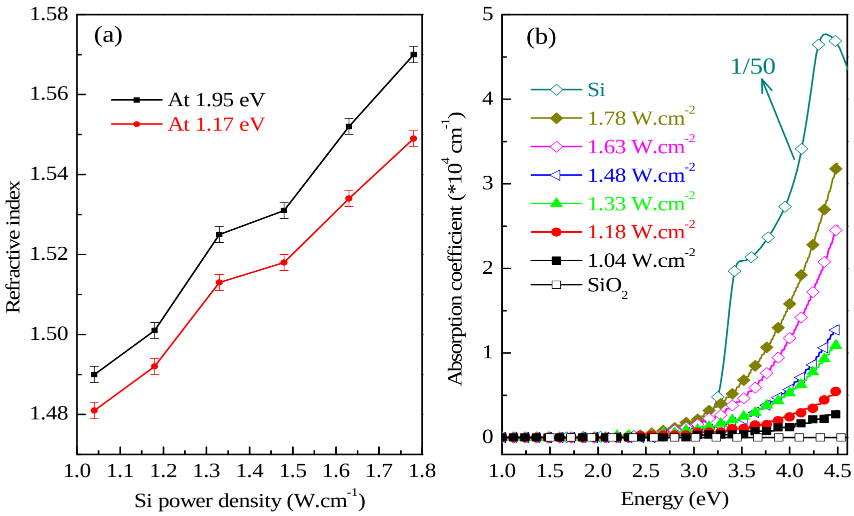

Figure 3.4: Evolutions of (a) refractive index with RFP_{Si} and (b) absorption coefficient with energy for as-grown films for different RFP_{Si} ranging from 1.04 to 1.78 W.cm^{-2}.

The refractive index and absorption coefficient are presented in figures 3.4(a) and (b), respectively, for films deposited by co-sputtering. As observed, the refractive indexes obtained at both energies (1.17 and 1.95 eV) gradually increase with RFP_{Si}. Contrarily to the reactive approach, no saturation of n value with RFP_{Si} has been found. Thus, such a method offers the possibility to incorporate higher Si excess by controlling the ratio of power densities applied on Si and SiO_2 cathodes. Figure 3.4(b) shows the absorption coefficient (α) for different RFP_{Si} as well as for pure SiO_2 and Si materials, as a function of energy in the 1.0-4.5 eV range. For all the samples, α is below 10^3 cm^{-1} in 1.0 to 2.5 eV range, while it can reach several 10^4 cm^{-1} for higher energies. In this region, α values of our films are between those of SiO_2 and Si materials, attesting the incorporation of Si excess with RFP_{Si}.

3.2.3 Estimation of Si excess

(a) From FTIR analysis

As mentioned in chapter 2 (sect. 2.2.1), the O/Si ratio (x) can be estimated from the FTIR spectra. The results are displayed in the left part of table 3.1. For reactive co-sputtering approach, x varies from 1.86 to 1.70 when r_H increases from 40 to 80% while, for the classical co-sputtering one, it ranges between 1.92 and 1.64 when RFP_{Si} varies from 1.04 to 1.78 $W.cm^{-2}$. As shown in table 3.1, the deduced Si excess is ranging from 2.4 to 5.6 at.% for the former, while for the latter, it is varying from 1.4 to 6.8 at.%.

Reactive co-sputtering						
	FTIR			Ellipsometry		
r_H (%)	W_{TO3} (cm^{-1})	x=O/Si	Si excess (at.%)	Refractive index at 1.95 eV	x=O/Si	Si excess (at.%)
40	1058	1.86	2.4	1.501	1.89	2.0
50	1054	1.78	3.9	1.533	1.81	3.3
60	1052	1.74	4.7	1.548	1.78	3.9
70	1051	1.72	5.1	1.562	1.75	4.5
80	1050	1.70	5.6	1.566	1.74	4.7
Classical co-sputtering						
	FTIR			Ellipsometry		
Si power density ($W.cm^{-2}$)	W_{TO3} (cm^{-1})	x=O/Si	Si excess (at.%)	Refractive index at 1.95 eV	x=O/Si	Si excess (at.%)
1.04	1061	1.92	1.4	1.490	1.91	1.5
1.18	1056	1.82	3.2	1.501	1.89	2.0
1.33	1053	1.76	4.3	1.525	1.83	3.0
1.48	1052	1.74	4.7	1.531	1.82	3.2
1.63	1049	1.68	6.0	1.552	1.77	4.1
1.78	1047	1.64	6.8	1.570	1.74	4.8

Table 3.1 Si excess estimated using FTIR experiments in left part and refractive index in right part for reactive (top) and classical (bottom) co-sputtered samples. The uncertainty of W_{TO3} value is 1 cm^{-1} while for n value is 0.002.

(b) From ellipsometric spectroscopy analysis

The O/Si ratio (*x*) can also be determined from the values of refractive index deduced from ellipsometric experiments (sect 2.2.2 chap.2). The *x* values obtained at 1.95 eV are shown in the right part of table 3.1. For reactive co-sputtered samples, the O/Si ratio is in the range 1.89 - 1.77 leading to a Si excess ranging from 2.0 to 4.7 at.%. For classical co-sputtered films, the deduced Si excess increases from 1.5 to 4.8 at.% with RFP_{Si}.

(c) Si excess error estimation

To compare the two determinations of the Si excess, the error estimations are discussed below.

- For FTIR approach,

as $x = 0.02W_{TO_3} - 19.3$, (see chap.2)

so $\Delta x = 0.02\Delta W_{TO_3}$.

(3.1)

where Δx is O/Si ratio error and ΔW_{TO3} is about 1 cm^{-1}.

- For ellipsometry approach,

as $x = \frac{-36n^4 + 691n^2 + 773}{22n^4 + 665n^2 - 472}$, (see chap.2)

so $$\left|\frac{\Delta x}{x}\right| = \left|\frac{(-144n^3 + 1382n)\times\Delta n}{-36n^4 + 691n^2 + 773}\right| + \left|\frac{(88n^3 + 1330n)\times\Delta n}{22n^4 + 665n^2 - 472}\right|, \quad (3.2)$$

where the Δn is about 0.002.

Since $Si_{ex}(at.\%) = y = \frac{2-x}{2+2x}\times 100\%$, (see chap.2)

we define the maximum and minimum values of Si excess achieved with an uncertainty Δx (eg. 3.1 and 3.2 depending on the techniques used):

$$y_{\max} = \frac{2-(x-\Delta x)}{2+2(x-\Delta x)}\times 100\%, \quad (3.3)$$

$$y_{\min} = \frac{2-(x+\Delta x)}{2+2(x+\Delta x)}\times 100\%, \quad (3.4)$$

The uncertainty Δy is determined by the absolute difference between y_{max} and y_{min} values. The obtained error values Δy plotted with the Si excess are shown in figure 3.5.

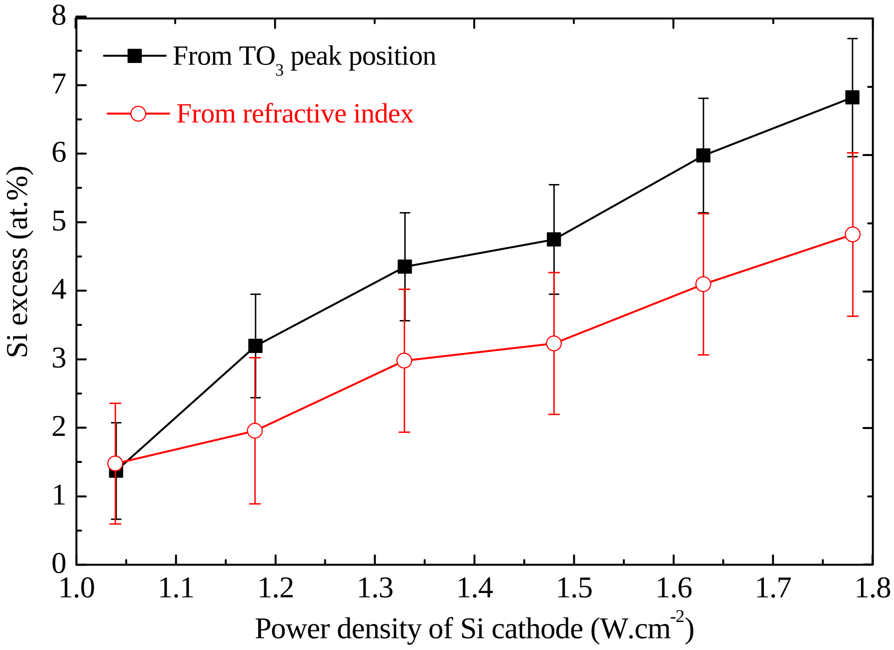

Figure 3.5: Si excess evolution with RFP$_{Si}$ with experimental error bars for classical co-sputtered samples analyzed by FTIR spectra and ellipsometry experiments.

One can see that, for this set of samples and both characterization techniques, the estimated Si excess has a comparable evolution trend showing an increase with *RFP*$_{Si}$. Indeed, the FTIR is sensitive to the free unbounded Si atoms, while ellipsometry method to the Si-nps "bulk" permittivity. Consequently, the two characterization methods are not describing the same "population" of excess of silicon. For this reason, the total Si excess may be obtained by the sum of excesses found by the two different methods. A third technique of chemical analysis (such as RBS) is required to could confirm this hypothesis.

3.2.4 Optimal Si content

The objective is to achieve the brightest emission intensity of the Nd^{3+}-doped layers under 488 nm non-resonant laser excitation. We have performed photoluminescence experiments on as-grown and 750°C-1min-annealed layers deposited either by reactive or classical magnetron co-sputtering. The following subsections will describe the PL emissions recorded for both approaches and will allows us to define the best deposition conditions for fabricating thin films that will be used for the annealing study.

(a) Reactive co-sputtering approach

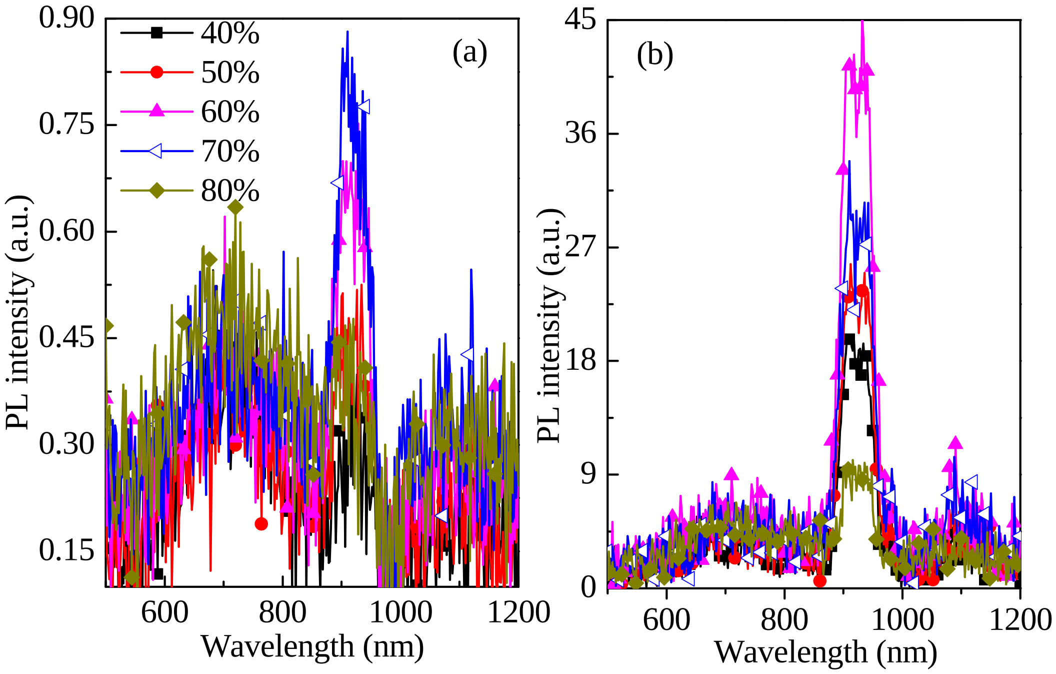

Figure 3.6: PL spectra for different hydrogen rate r_H (from 40% to 80%): (a) as-grown samples and (b) 750°C-1min-annealed samples excited at non-resonant wavelength for the Nd^{3+} ions (488 nm).

Figure 3.6 shows the PL spectra of samples deposited with different r_H values before (a) and after annealing at 750°C during 1 minute (b). The PL spectra in figure 3.6(a) show emission peaks clearly visible in the 600-800 nm range and at 920 nm from the as-deposited samples. The former could be ascribed to the presence of Si-nps and/or radiative defects[7] [8] while the latter is the results of the $^4F_{3/2}$-$^4I_{9/2}$ transition in the Nd^{3+} ions[9]. Such an emission achieved with a non-resonant excitation wavelength (488 nm) for the Nd^{3+} ions confirms the role of hydrogen for promoting the formation of sensitizers towards Nd^{3+} ions but also demonstrates the quality of the as-grown layers. One can notice that the increasing r_H enhances the emissions of Nd^{3+} ions. After an RTA annealing treatment, the PL intensity of the Nd^{3+} peak is increasing by one order of magnitude (see pink curve-r_H=60%) while the visible peak emission remains almost the same. The decrease of the PL observed for the r_H=70% deposited layer after annealing demonstrates the importance of monitoring the Si excess to achieve the highest sensitizers density and the lowest distance to Nd^{3+} ions. The optimal Si excess for this fabrication approach is obtained for r_H=60%.

(b) Classical co-sputtering approach

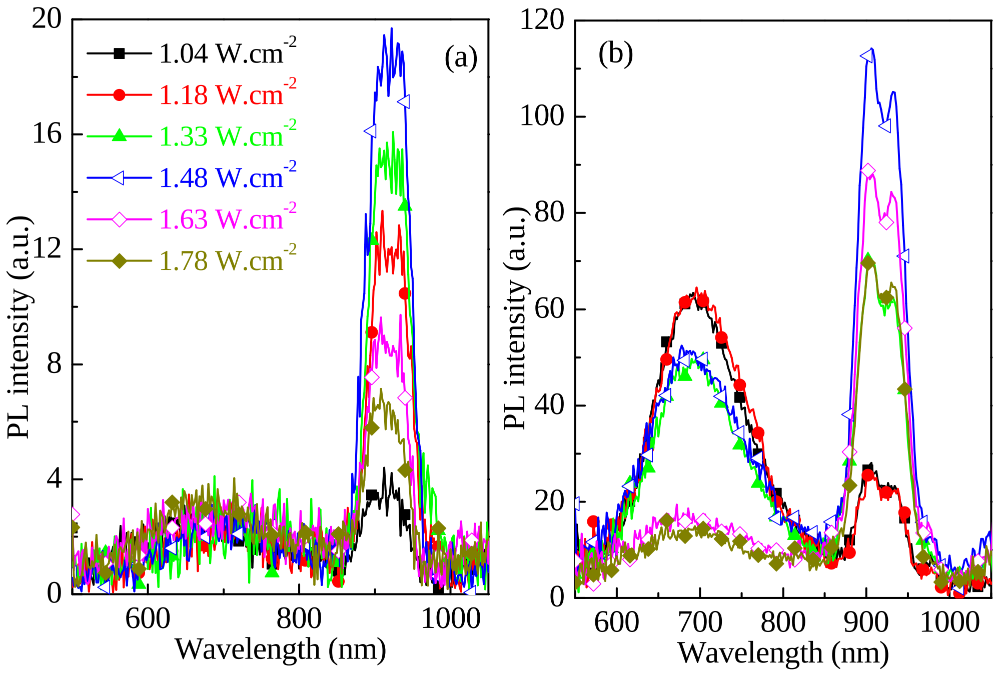

Figure 3.7: PL spectra of (a) as-deposited samples deposited at 500°C and (b) 750°C-1min-annealed samples used RFP$_{Si}$ ranging from 1.04 to 1.78 W.cm^{-2}. The excitation wavelength is 488 nm which is non-resonant for the Nd^{3+} ions.

The PL spectra for as-grown samples deposited at 500°C are shown in figure 3.7(a). One can clearly notice the emission at about 920 nm from Nd^{3+} ions. The intensity is quite higher than that of reactive sputtered samples, even after the annealing treatment (Fig. 3.6(a) and (b)). This is probably due to the higher deposition temperature 500°C with respect to 100°C for reactive sputtering method, which is supposed to improve the quality of the host matrix and thus begin to passivate the non-radiative channels. Moreover, the Nd^{3+} PL intensity shows first an increase with *RFP$_{Si}$*, up to a maximum corresponding to sample deposited with 1.48 W.cm^{-2} (4.7 at.% Si excess from FTIR experiments), and then decreases for higher power densities. After annealing, the same trend is conserved (Fig. 3.7(b)). This evolution may be explained by two reasons. On one hand, the first increase of power density is expected to enhance the density of Si-nps for an optimized Nd^{3+}:Si-nps interaction[10] [11]. Further increase of *RFP$_{Si}$* up to 1.78 W.cm^{-2} might lead to increasing the average size of the formed Si-nps at the expense of their density (as shown by FTIR) and then of their coupling with Nd^{3+} ions[12] [13]. On the other hand, the increasing Si incorporation may result in disorder in the host (as shown by FTIR), which will favor the non-radiative channels.

In the visible domain of figure 3.7(b), all the films show a broad band centered at fixed position about 700 nm. This PL band can be originating from amorphous Si-nps and/or from defects levels. One can notice that the PL intensity decreases with higher RFP_{Si} which can be attributed to the creation of concomitant non-radiative defects and/or to an efficient energy transfer from sensitizers to surrounded Nd^{3+} ions.

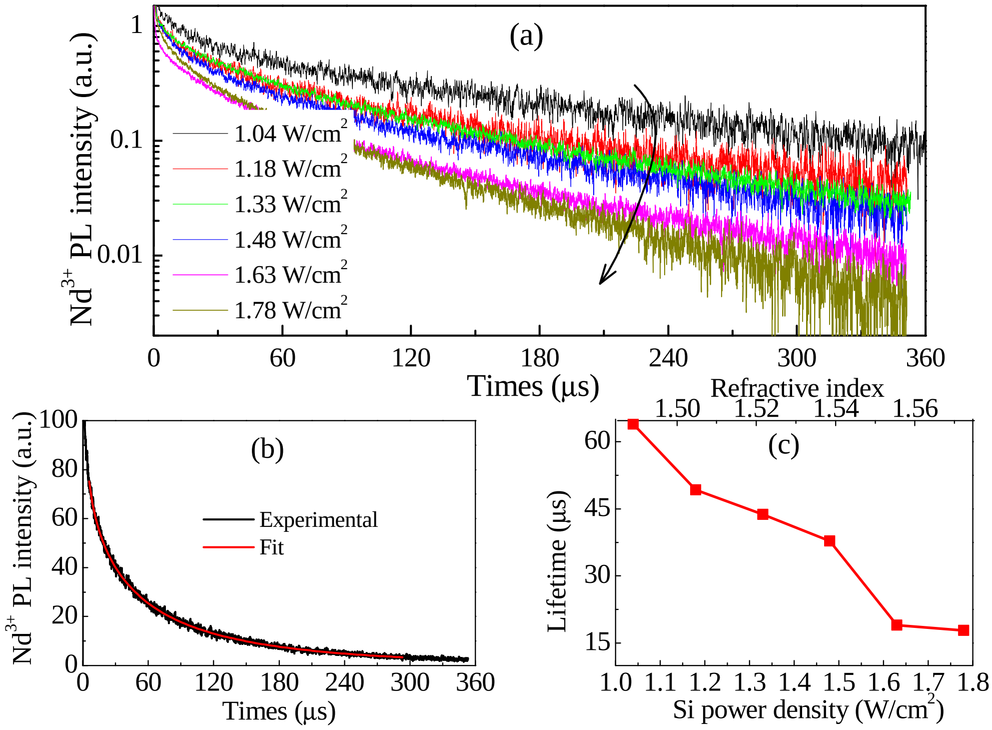

Figure 3.8: (a) Nd^{3+} PL decay curves of 750°C-1min-annealed films deposited with different RFP_{Si}, (b) a typical decay curve of Nd^{3+} PL with its fitting, (c) Evolution of the Nd^{3+} lifetimes with RFP_{Si} as well as refractive index. The excitation wavelength is 488 nm which is non-resonant for the Nd^{3+} ions.

To further study the influence of Si excess on 750°C-1min-annealed samples, decay time measurements were carried out on Nd^{3+} PL at 920 nm. As observed in figure 3.8(a), the curve decays faster with RFP_{Si} and presents a non-exponential nature. The recorded data were thus fitted by means of a stretched exponential function: $I(t)=A\exp[-(t/\tau)^{\beta}]$[14] as shown in figure 3.8(b). The obtained stretched exponent β remains constant about 0.6 for all films, and the lifetime τ is in the order of tens of µs, comparable to the values reported from other Nd-doped silica-based thin films[15]. τ decreases (Fig. 3.8(c)) from about 64 to 18 µs with the incorporation of Si, which is comparable to the lifetime evolution of Er^{3+} noticed in similar system[3]. This evolution can thus be explained by some increase in the average size of Si-nps at the expense of their density and their coupling with rare earth ions. Moreover, it is assumed that a concomitant increase of the disorder of the matrix results in an increase of the number of non-radiative channels.

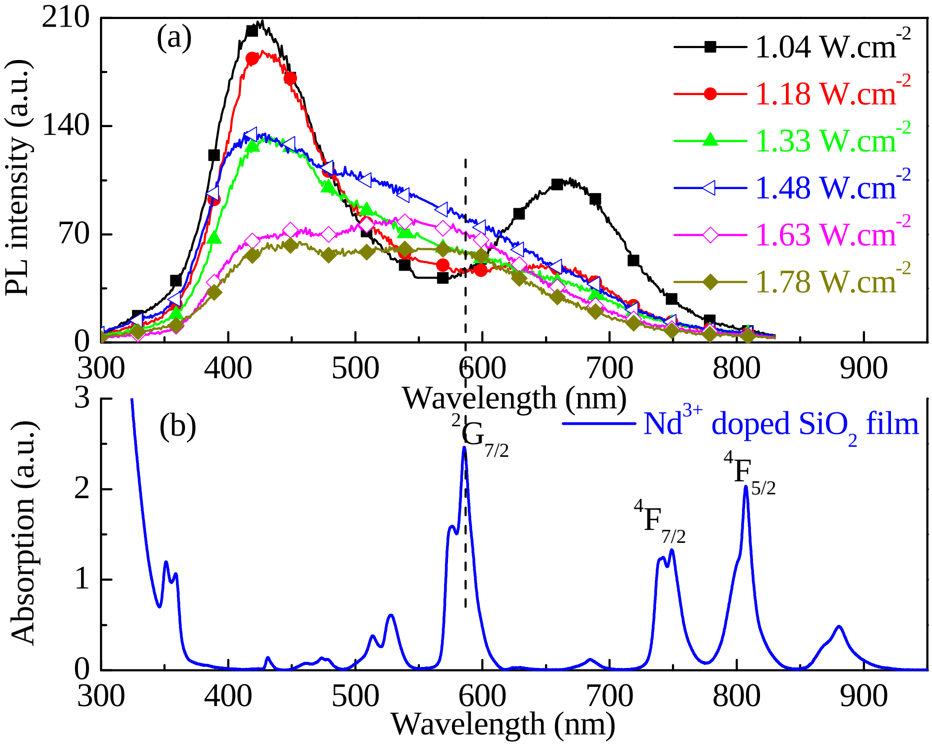

Figure 3.9: (a) Visible PL spectra for 750°C-1min-annealed samples deposited with various Si target power density. The excitation source is a 450 W Monochromatic xenon lamp at 280 nm. (b) Absorption spectrum for Nd^{3+} doped SiO_2 film.

This part aims at investigating the effect of Si excess on visible PL spectra using a 280 nm excitation wavelength. Higher energy excitation was performed on the layers in order to evidence the presence of emitters with larger recombination energy which can be used as efficient sensitizers for the excitation of Nd^{3+} ions. As observed from the obtained spectra in figure 3.9(a), two remarkable peaks centered at about 420 and 660 nm are present. The former is originating from the oxygen-deficient centers (ODCs) while the latter from the non-bridging oxygen hole centers (NBOHCs)[16], [17]. In fact, the various ODCs have a broad emission band ranging from about 400 to 600 nm as evidenced by cathodo-luminescence technique in similar layers doped with Er^{3+} ions[18]. In our films, the increasing RFP_{Si} leads to the decrease of 420-nm peak intensity while the 550 nm-ODCs peak gradually raises, reaching a maximum for the layer deposited with 1.48 W.cm^{-2} before decreasing for higher RFP_{Si} values. This evolution can be attributed to the increasing incorporation of Si, one on hand, leading to the change of ODCs structure and/or number. One the other hand, non-radiative paths are concomitantly formed due to a higher disorder that quenches the ODCs luminescence for higher Si excess. For the NBOHCs present in Si-rich silicon oxide film, they are attributed to some local atomic rearrangement that differs from the SiO_4 tetrahedron expected for a "perfect" silica matrix. The decrease of NBOHCs peak intensity, may be explained by the fact that more Si atoms are incorporated less non-bridging O atoms remain in the film.

To correlate these visible spectra with Nd^{3+} emission displayed in figure 3.7(b), the absorption spectrum[1] of a Si-free Nd^{3+} doped SiO_2 film is shown in figure 3.9(b). The comparison between figure 3.9(a) and (b) proves that:

- ODCs emitting at 420 nm cannot resonantly excite Nd^{3+} ions while those at 585 nm can directly transfer the energy to the $^2G_{7/2}$ level of Nd^{3+} ions present in the surrounding.
- The maximum intensity for 585 nm ODCs is obtained for the film deposited with an RFP_{Si} of 1.48 $W.cm^{-2}$, which concomitantly holds an optimal Nd^{3+} PL intensity (Fig. 3.7(b)).
- NBOHCs emitting at 660 nm do not match the energy levels of Nd^{3+} ions.

3.3 Effect of Nd content incorporated

3.3.1 Estimation of Nd content

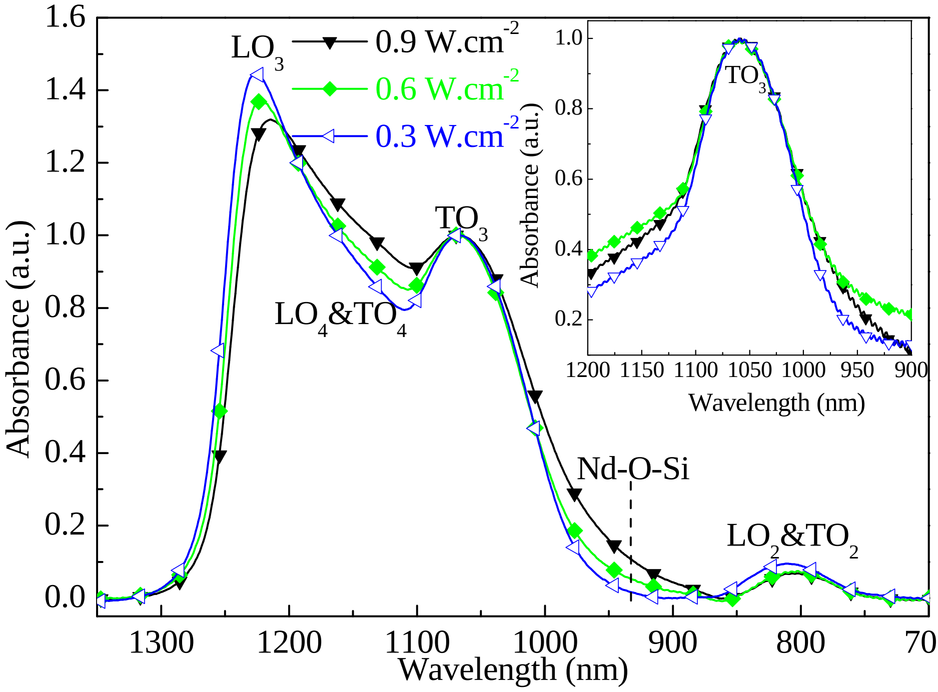

Figure 3.10: FTIR spectra recorded at Brewster incidence for samples deposited with the indicative RFP_{Nd2O3}, while the inset corresponds to normal incidence.

Apart from the Si excess, Nd content is another key parameters influencing the Si:Nd coupling. The Nd_2O_3 power density (RFP_{Nd2O3}) is a common way to monitor the Nd content, fixing the RFP_{SiO2} and RFP_{Si} at 8.88 and 1.48 $W.cm^{-2}$ respectively. These latter have been kept constant in classical co-sputtering approach for this specific study, which is only concerned in this section. As a first step, the samples deposited with RFP_{Nd2O3} ranging from 0.3 to 0.9 $W.cm^{-2}$ are studied by FTIR experiments whose resulting spectra are shown in figure 3.10. Two strong bands, LO_3 and TO_3, are presented, which are both due to Si-O bond vibrations. The position of TO_3 peak is independent of RFP_{Nd2O3}, as clearly seen from the inset of Fig. 3.10, which is a characteristic of a constant Si excess in these samples. The LO_4&TO_3 pair increases with RFP_{Nd2O3} due to the higher Nd content leading to a higher disorder degree. Moreover, a shoulder band at about 940 cm^{-1} whose intensity raises with RFP_{Nd2O3} is originating from Nd-O-Si vibration[19]. These results confirm that the Nd ions content can be tuned by the RFP_{Nd2O3}.

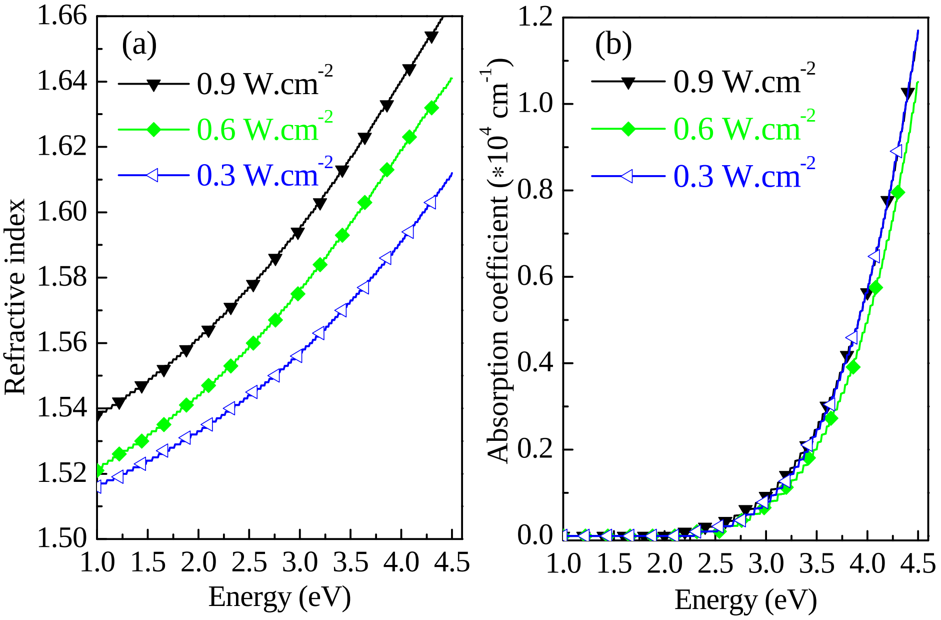

Figure 3.11: Evolutions of (a) refractive index and (b) absorption coefficient with the energy for samples deposited with the indicative RFP$_{Nd2O3}$.

The evolutions of refractive index and absorption coefficient with *RFP*$_{Nd2O3}$ are shown in figure 3.11. The refractive index increases significantly with *RFP*$_{Nd2O3}$ while the absorption coefficient remains invariable. The Si excess being constant, the increase of n attests the raise of Nd incorporation with *RFP*$_{Nd2O3}$.

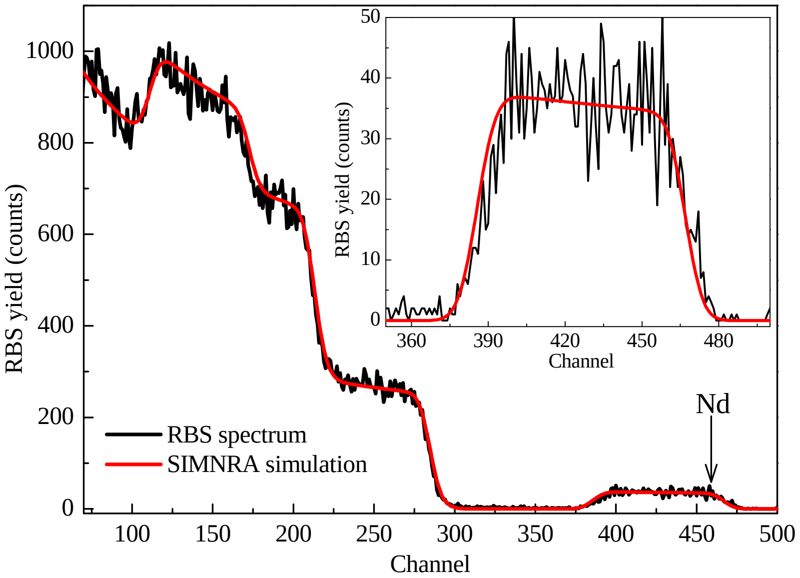

Figure 3.12: A typical RBS spectrum of film deposited with RFP$_{Nd2O3}$ *= 0.3 W.cm*$^{-2}$ *and RFP*$_{Si}$*= 1.48 W.cm*$^{-2}$*. The inset shows an enlargement in the 350-500 channels region.*

The estimation of Nd incorporated in our layers has been achieved by using Rutherford Backscattering Spectrometery (RBS). A typical recorded spectrum is shown in figure 3.12. The low-channel part, below 300 channels, corresponds to backscattering from Si and O atoms in the film and from Si atoms in the substrate. It is worth to note that both Si and O concentrations cannot be accurately extracted here probably due to a low sensitivity of RBS towards light elements. In the high-channel part, the RBS signal from about 380 to 480 channels is attributed to Nd atoms in the layer. As shown in the inset, the RBS yield remains constant for this high channels region. This witnesses the uniform distribution of Nd atoms through the as-deposited layer. According to the simulation using SIMNRA code, the Nd content is about 5.0×10^{19} at.cm^{-3} (applied RFP_{Nd2O3} = 0.3 W.cm^{-2} and RFP_{Si}= 1.48 W.cm^{-2}). Indeed, this value remains constant for RFP_{Si} varying between 1.3 to 1.78 W.cm^{-2}. While for a lower RFP_{Si} such as 1.04 W.cm^{-2}, the doped Nd concentration is decreased to almost 2.7×10^{19} at.cm^{-3} (for a same applied RFP_{Nd2O3} of 0.3 W.cm^{-2}). Thus, Nd incorporation is influenced by RFP_{Si} probably ascribed to the change of the mean free path of sputtered species from Nd_2O_3 target.

Concerning the Si excess determination, the RBS measurements can’t provide an unambiguous confirmation that the total Si excess can be the sum of Si excesses determined by FTIR and ellipsometry techniques. We thus consider Si excesses separately in the following manuscript by referring each time to the used characterization technique.

3.3.2 Photoluminescence properties

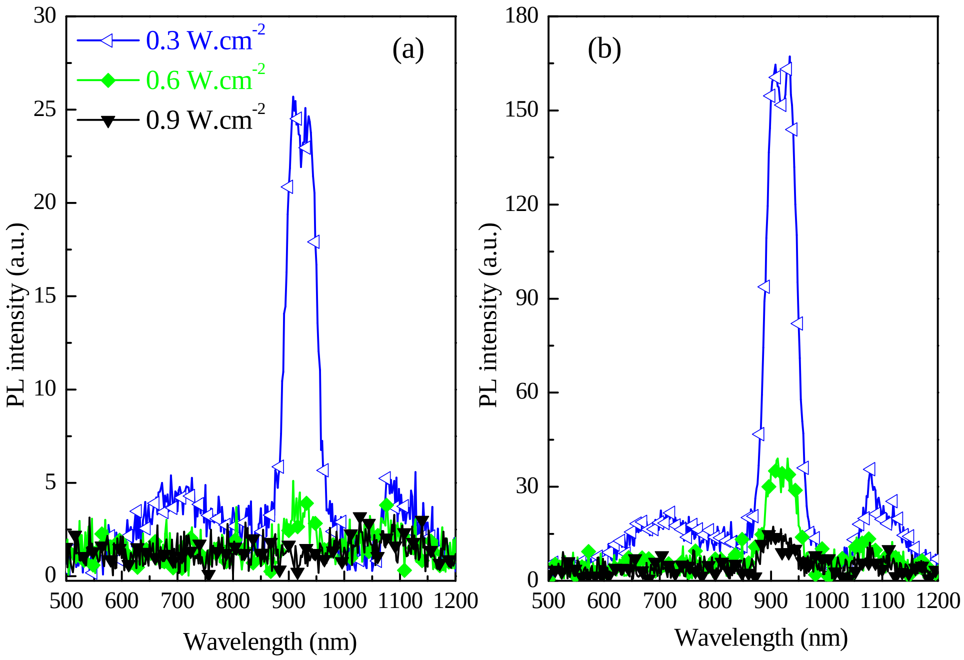

Figure 3.13: PL spectra of (a) as-deposited and (b) 750ºC-1hour-annealed samples deposited with RFP_{Si}*= 1.48 W.cm*$^{-2}$ *and for different* RFP_{Nd2O3} *in 0.3-0.9 W.cm*$^{-2}$ *range. The excitation wavelength is 488 nm which is non-resonant for the Nd*$^{3+}$ *ions.*

The PL spectra of samples deposited with various RFP_{Nd2O3} are shown in figure 3.13. As seen for both as-deposited and annealed layers, the intensities of Nd^{3+} emission at 920 nm dramatically fall when RFP_{Nd2O3} increases from 0.3 to 0.6 W.cm^{-2}. And it further attenuates for RFP_{Nd2O3}= 0.9 W.cm^{-2}. Such evolution often called “concentration quenching” is partly explained by cross relaxation processes between Nd^{3+} ions and/or Nd_2O_3 clusters as reported in glass matrix[20]. This is supported by the existence of Nd_2O_3 clusters in the highly doped Nd samples[21]. Besides, non-radiative channels inherent to disorder induced by the Nd incorporation (see FTIR spectra of Fig. 3.10) can be in competition with the ways of Nd^{3+} radiative recombination. The concomitant decrease of 700nm-peak from matrix gives another evidence of the presence of non-radiative channels due to the increase of Nd concentration. As a consequence, the emission of Nd^{3+} ions is more intense when the Nd content is low (5.0×10^{19} at.cm^{-3}) corresponding to RFP_{Nd2O3} = 0.3 W.cm^{-2}.

3.4 Effect of annealing conditions

To study the effect of annealing conditions, the optimized layer deposited by co-sputtering approach with RFP_{Si} = 1.48 W.cm^{-2} and RFP_{Nd2O3} = 0.3 W.cm^{-2} has been chosen. As described in section 2.1.2 of chapter 2, there are two annealing approaches, RTA and CA, used in this work.

3.4.1 Annealing temperature for RTA approach

(a) Fourier transform infrared spectroscopy

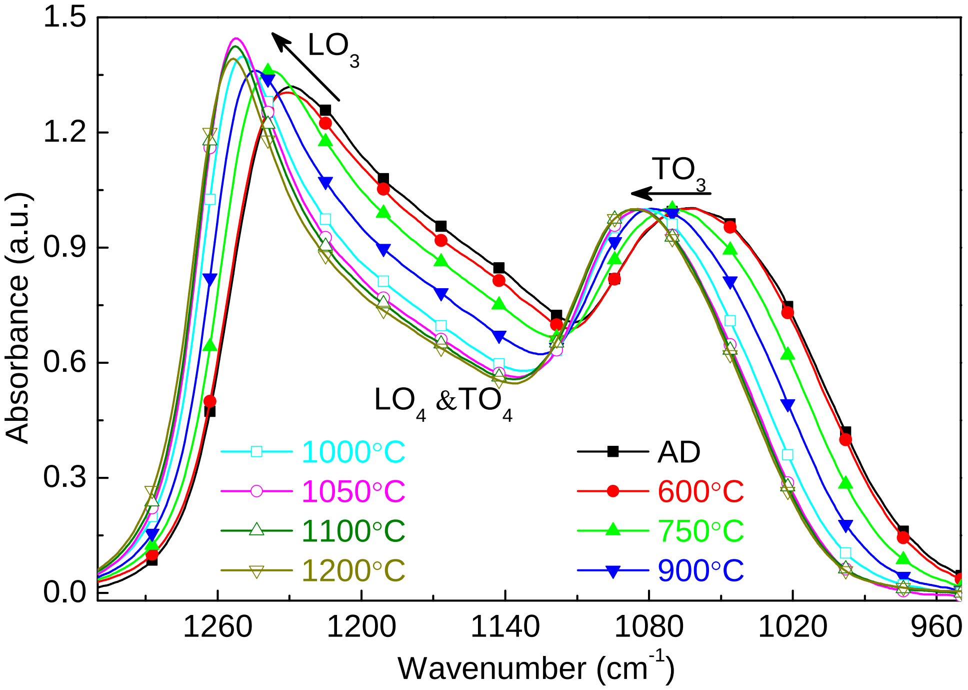

Figure 3.14: FTIR spectra recorded at Brewster angle of 65º for as-deposited (AD) and 1min-annealed Nd-SiO$_x$ films at indicated T_A temperature. The spectra were normalized to the intensity of one at the top of TO_3 band.

Figure 3.14 shows the evolution of FTIR spectra for Nd-SiO$_x$ films annealed at different temperatures. There are two main bands, as mentioned above, attributed to longitudinal optical (LO_3) and transverse optical (TO_3) phonons of Si-O bonds. The relative intensity of the former peaking in the 1230-1255 cm^{-1} range increases with T_A up to 1050ºC, and then slightly decreases for higher T_A. According to the work of Olsen and Shimura[22] LO_3 band intensity corresponds to the number of Si-O-Si bonds at 180º present at the Si/SiO$_2$ interface. Consequently, this is the signature of the increasing formation of Si-nps in our film upon annealing temperature up to 1050ºC. For increasing T_A, the Si-nps size increases at the expense of Si-nps density characterized by the number of Si-O-Si bonds located at the Si/SiO_2 interfaces. As a consequence, a slight decrease of the LO_3 mode intensity (with respect to TO_3) is noticed. Concerning the peak positions of LO_3 and TO_3 modes, they respectively blue-shift from 1230 to 1255 cm^{-1} and from 1052 towards 1081 cm^{-1} with increasing T_A. These progressive shifts towards the stoichiometric position of amorphous SiO_2 (1255 cm^{-1} for LO_3 and 1081 cm^{-1} for TO_3) are indicative of the phase separation between Si-nps and silicon oxide occurring in the film. This is confirmed by the decrease of the disorder in the matrix as evidenced by the evolution of the intensity of the LO_4&TO_4 pair modes with T_A.

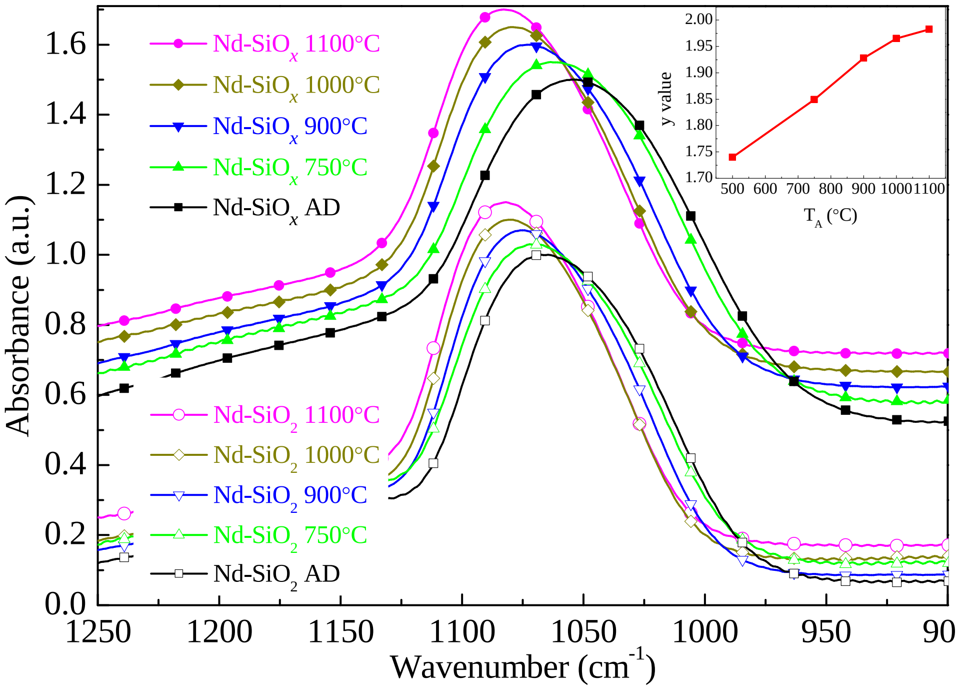

Figure 3.15: FTIR spectra of typical Nd-SiO_x (solid) and Nd-SiO_2 (hollow) films, collected at normal incidence for as-deposited (AD) and indicative T_A-1min-annealed samples. Inset shows the y values in SiO_y phase versus T_A.

In order to evidence the phase separation between Si and SiO_y ($y>x$) occurring in samples of SiO_x, normal incidence FTIR spectra were performed on Nd-SiO_x and Nd-SiO_2 films. The latter film without Si excess was deposited using the similar parameters to have a SiO_2 reference sample to compare with SiO_x one at each T_A. As shown in figure 3.15, the peak positions of both samples move to higher wavenumbers with increasing T_A, and both almost reach the same peak position after an annealing at 1100°C. It can be deduced from the following equation:

$$y = 2\frac{W_{TO_3}^{SiO_x} - W_{TO_3}^{Si}}{W_{TO_3}^{SiO_2} - W_{TO_3}^{Si}}. \tag{3.5}$$

The $W_{TO_3}^{Si}$ value is 965 cm^{-1}[23], while the $W_{TO_3}^{SiO_x}$ and $W_{TO_3}^{SiO_2}$ values correspond to the TO_3 peak position for annealed Nd-SiO$_x$ and Nd-SiO$_2$ films, respectively. One can obtain a gradual increase of y value (Fig. 3.15 inset), which denotes the phase separation process with a decrease of isolated Si atoms in silicon oxide phase. Considering that we have no oxidation process during the annealing treatment, this is thus a signature of the formation of Si-nps.

(b) Raman spectroscopy

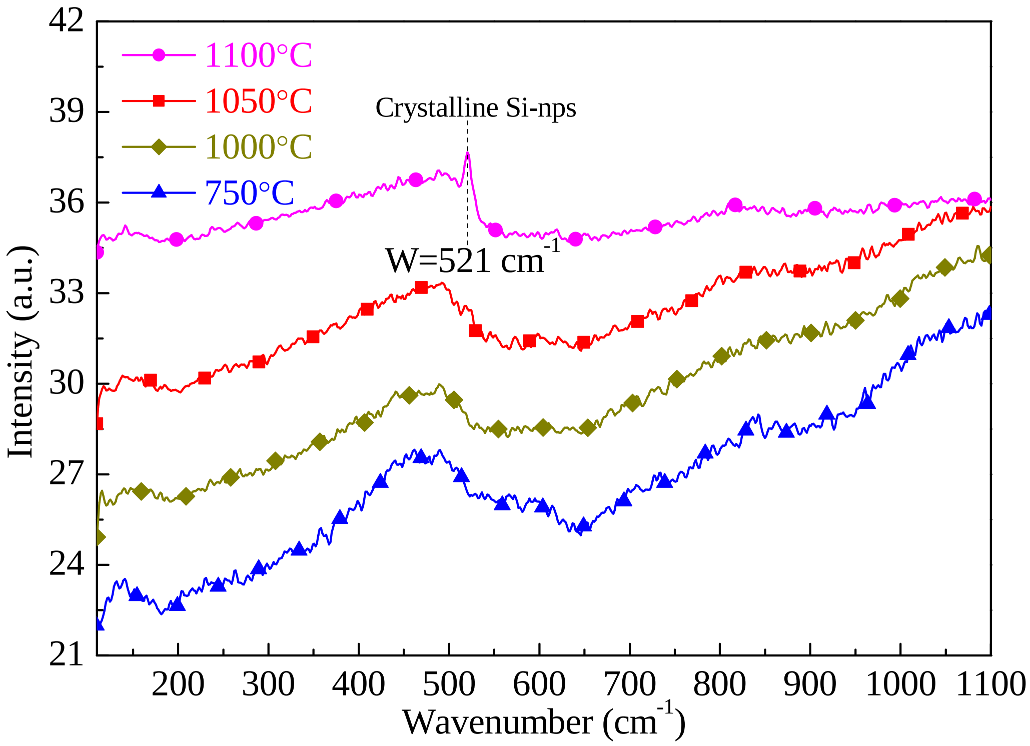

Figure 3.16: Raman spectra of the Nd-SiO$_x$ films deposited on quartz substrate and annealed at indicated T_A for 1 min.

The evolution of film microstructure versus T_A has been analyzed by means of Raman spectroscopy (Fig. 3.16). Each curve has a broad band peaking at ~480 cm^{-1} attributed to amorphous Si agglomerates. Such a result is in agreement with above FTIR results revealing the formation of Si-nps at low temperature (750°C)[24]. By increasing T_A up to 1100°C, a sharp peak at around 521 cm^{-1} assigned to crystalline

Si-nps appears while, in the same time, the 480 cm^{-1}-band intensity decreases. This convincingly certifies that the T_A=1100°C annealing promotes the formation of Si nanocrystals. The results of Raman experiments on non-doped-SiO_x thin films (not shown here) follow the same trends. This is supported by the fact that the low Nd content incorporated may not affect the formation of either amorphous or crystalline Si-nps.

(c) Photoluminescence properties

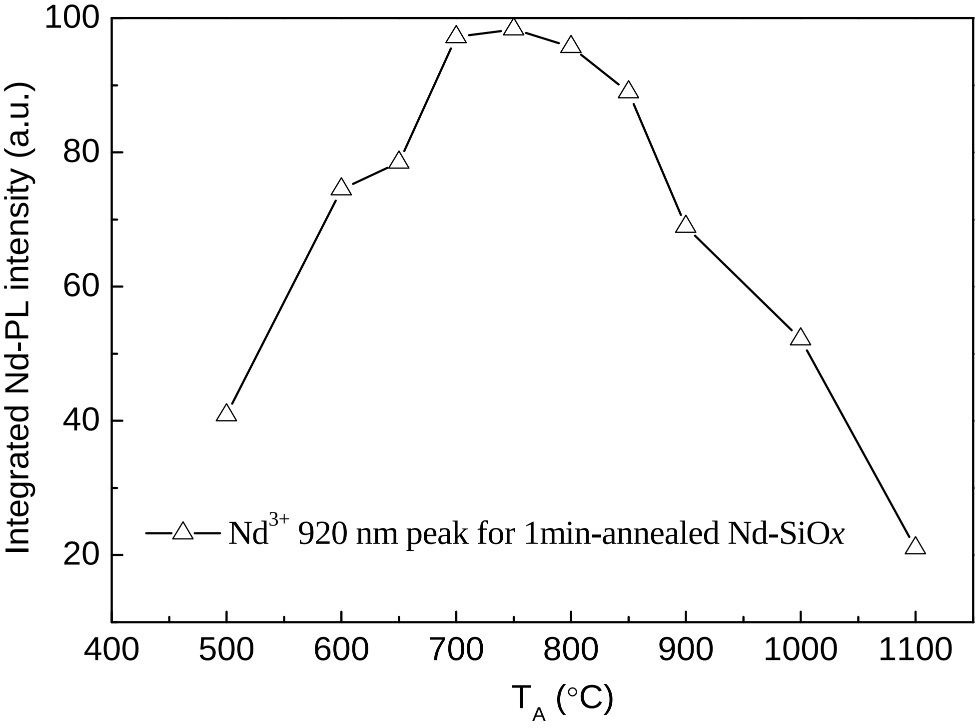

Figure 3.17: Evolution of Nd^{3+} PL intensity at 920 nm as a function of T_A for 1min-annealed Nd-SiO_x films excited by a 488 nm excitation wavelength non-resonant for the Nd^{3+} ions.

This paragraph will address the effect of T_A on Nd^{3+} PL properties (Fig. 3.17). Even though the as-deposited layer clearly shows PL, the intensity increases with T_A and is enhanced by a factor 2.5 upon annealing at 750ºC before decreasing for higher T_A. The optimized temperature at 750ºC corresponding to maximum Nd^{3+} PL may be explained by the fact that both matrix ordered degree and coupled Nd^{3+} number evolve in opposite trend with annealing temperature. In this regard, the FTIR spectra reported in figure 3.14 have evidenced the attenuation of LO_4&TO_4 pair mode with increasing T_A. Such an evolution implies that the film matrix gradually becomes ordered, which would favor the Nd^{3+} emission by decreasing the non-radiative paths.

The concomitant increase of the LO_3 intensity with T_A in the 600-1050°C range suggests an increase of Si-nps density also favoring an enhancement of Nd^{3+} emission. But, for $T_A \geq 750$ºC, formation of Nd_2O_3 clusters occurs and decreases the Si:Nd^{3+} coupling rate as evidenced by lifetime measurements detailed below. Therefore, a maximum Nd^{3+} PL is reached at the moderated temperature (T_A=750ºC) and always short time (1 min.).

3.4.2 Annealing temperature for CA approach

(a) Fourier transform infrared spectroscopy

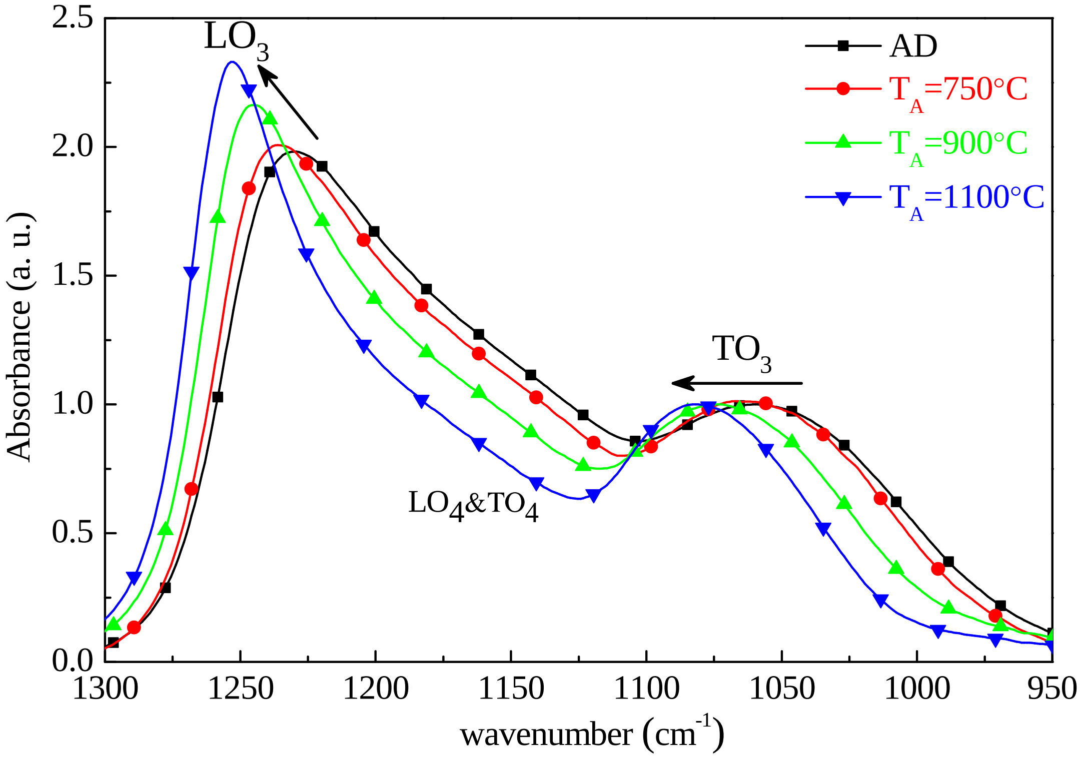

Figure 3.18: FTIR spectra recorded at Brewster angle of 65º for as-deposited (AD) and 1hour-annealed Nd-SiO_x films. The films were annealed at indicated T_A.

The effects of annealing temperature on FTIR spectra are presented in figure 3.18. The TO_3 peak position shifts gradually from 1052 to 1081 cm^{-1} with the increasing annealing temperature. This shift is explained the increase of Si-nps size at the expense of Si-nps density with annealing temperature. Moreover, the intensity of the LO_3 peak increases while that of the LO_4&TO_4 pair mode attenuates with T_A. The former is a signature of the improvement of the Si/SiO_x interface, whereas the latter indicates a reduction in disorder of the host matrix. As a consequence, the spectra show a similar behavior as those obtained on films annealed by RTA in figure 3.14.

(b) Raman spectroscopy

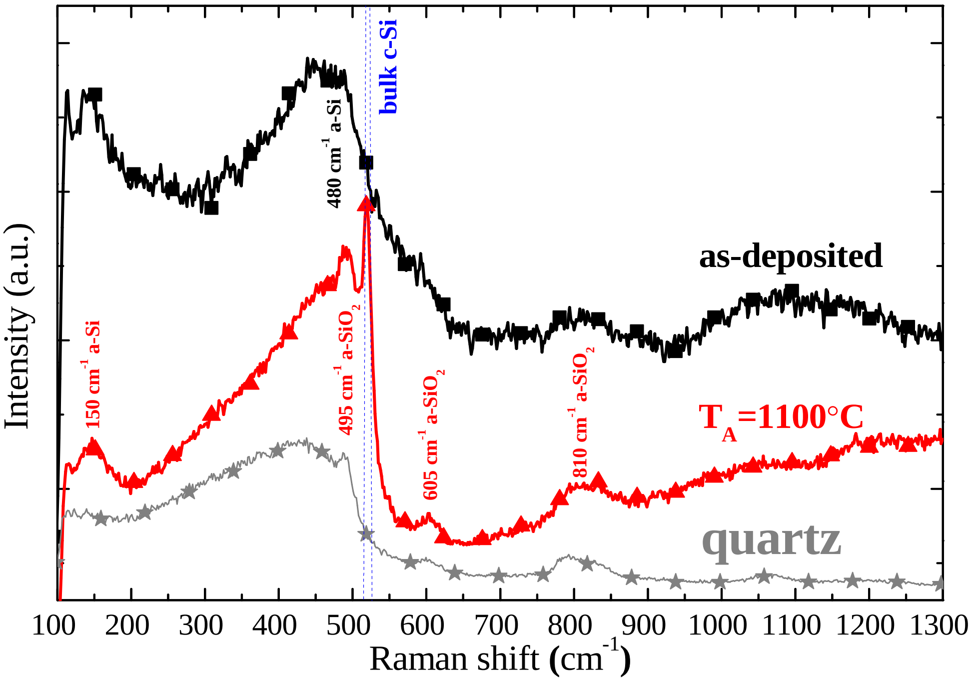

Figure 3.19: Raman spectra of the Nd-SiO$_x$ films deposited on quartz substrate before and after 1hour-annealing at 1100ºC. Both spectra of quartz substrate and bulk crystalline Si wafer peak are also shown.

Figure 3.19 displays the Raman spectra of Nd-SiO$_x$ films and a quartz substrate. They reveal several Raman bands located at 495, 605, and 810 cm^{-1} due to phonons in amorphous silica. The as-deposited sample presents two additional bands at 150 and 480 cm^{-1} which are attributed to the amorphous Si. This denotes that Si-nps are already formed in the as-grown layers. After annealing at 1100ºC, these two bands are attenuated. Concomitantly, a sharp peak located at about 521 cm^{-1} appears. This peak position is the same as that of bulk crystalline Si wafer, demonstrating the emergence of crystalline Si nanoparticles. Thus, the similar Raman behaviors are observed as those of RTA samples presented in figure 3.16.

(c) Photoluminescence properties

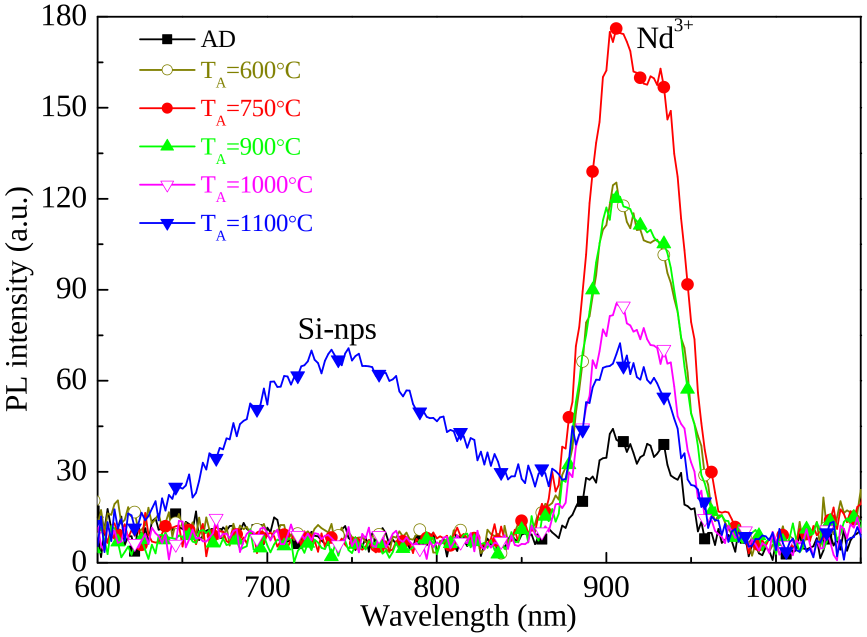

Figure 3.20: evolution of PL spectra of samples before and after annealing at the indicative temperature for 1 hour duration. The excitation wavelength is 488 nm which is non-resonant for the Nd^{3+} *ions.*

Figure 3.20 shows the evolution of the room temperature PL spectra of samples before and after annealing at the indicative temperature. In the visible range, a broad PL band centered at about 750 nm is recorded for 1100ºC-annealed layers. This band is originating from recombination occurring in quantum-confined excitonic states in Si-nps. When the layers are annealed at lower temperatures, no emission peak has been observed. However, the microstructural analyses have evidenced the presence of Si-nps in these films. Thus, the quenching of the visible emission can be attributed to either an efficient energy transfer to surrounding Nd^{3+} ions or to non-radiative defects present in the host matrix. The analyses of the Nd^{3+} emission intensity at around 920 nm reveal a gradual increase of the emission up to a maximum reached for T_A = 750ºC, following by a decrease for higher temperatures. Thus the quenching of the visible PL in the 600-900°C range is probably due to the sensitization of the lanthanide ions, the optimized Si:Nd coupling being achieved after an annealing at 750ºC. It is worth to note that a notable emission from Nd^{3+} ions was obtained for the as-deposited sample and this fact can be explained by either formation of Si-nps during fabrication process or by energy transfer from host defects towards Nd^{3+} ions[25].

3.4.3 Annealing duration

It was seen in previous sections that the structural and PL properties show similar behavior for layers annealed by RTA and CA approach. The former duration is fixed at 1 minute while latter at 1 hour. To optimize the annealing processes, intermediate durations have been investigated. In this part, some specific annealing is carried out in RTA furnace for duration in 5-60 min range.

(a) Transmission electron microscopy

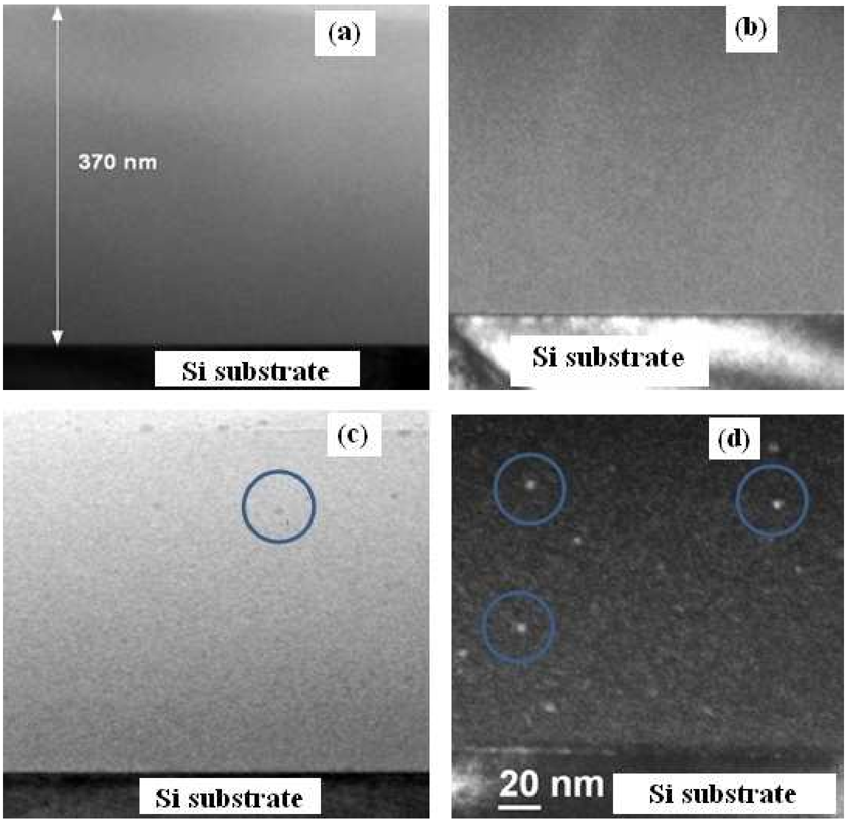

Figure 3.21: (a) bright field and (b) dark field images for 1min-1100ºC-annealed layer, (c) bright field and (d) dark field for images for 1hour-1100ºC-annealed layer. The layer thickness is about 370 nm. The present Si-nps are highlighted by a circle.

In order to explore the effects of annealing duration on layer microstructure, transmission electron microscopy (TEM) investigations were carried out on Nd-SiO$_x$ films annealed at 1100ºC either in RTA or CA furnaces. As shown in figure 3.21, one cannot observe any crystalline Si-nps in the 1min-annealed layer whereas Si nanocrystals have been detected by Raman spectroscopy (See Fig. 3.16). This can be due either to their smaller size than the TEM resolution and/or their weak density. By contrast, in both bright and dark field images the 1hour-annealed layer clearly presents crystalline Si-nps with an average size of about 5 nm. This confirms that a longer annealing time favors larger Si-nps formation.

(b) Photoluminescence properties

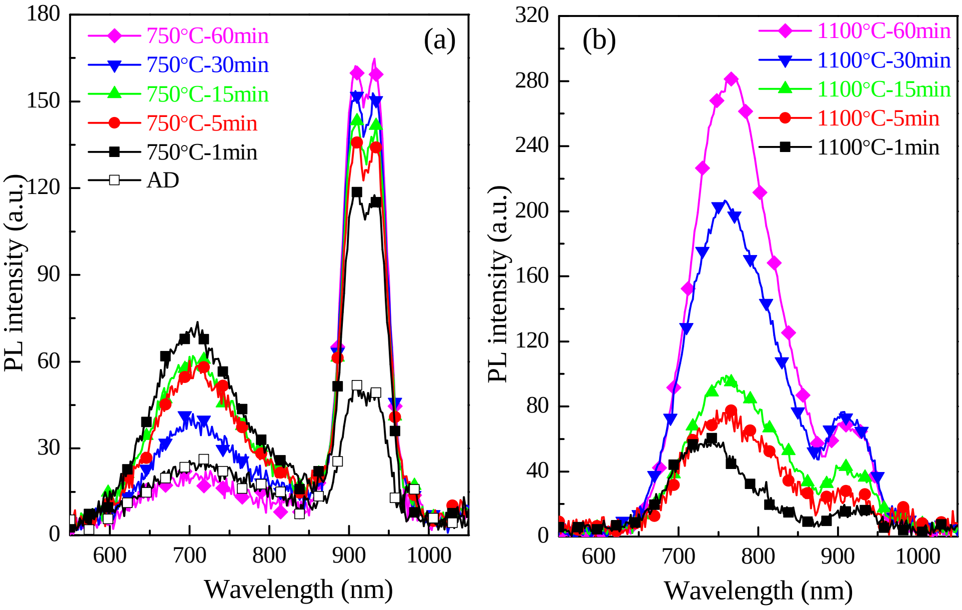

Figure 3.22: PL spectra of samples annealed for the indicative duration at 750ºC (left) and 1100ºC (right). The excitation wavelength is 488 nm which is non-resonant for the Nd^{3+} ions.

Figure 3.22 shows the PL spectra versus annealing duration (t_A) for two typical temperatures at 750ºC and 1100ºC. After an annealing at 750ºC (Fig. 3.22 (a)), we notice the presence of a PL emission in the 600-800 nm region whose the intensity decreases with t_A and the position sets invariable at about 710 nm. Such a behavior follows the signature of radiative defects as discussed in detail latter. In the same time, the 920nm-PL emission of the Nd^{3+} ions non-resonantly excited with 488 nm light increases with t_A. These evolutions are the signature of sensitizers present in the matrix which transfer efficiently their energy to the surrounding lanthanide ions and of a recovering of the non-radiative channels with the annealing duration. Both processes allow the promoting the emission of the rare earth ions. After an annealing at higher temperature (1100°C), the visible peak intensity increases with t_A and its position gradually shifts to higher wavelength (Fig. 3.22 (b)). Such a behavior is originating from the growth of larger Si-nps with t_A leading to modification of the band gap of the quantum confined Si-np. As in the previous case, the Nd^{3+} peak emission increases with t_A but remains lower than in the 750°C-annealing treatment case. In contrast, the emission in visible range has higher intensity at 1100°C than the case at 750°C. This is probably due to the formation of Nd_2O_3 clusters leading to lower the number of Nd^{3+}:Si-nps coupling. It thus results in a low intensity of Nd^{3+} PL and in an enhancement of Si-nps emission intensity.

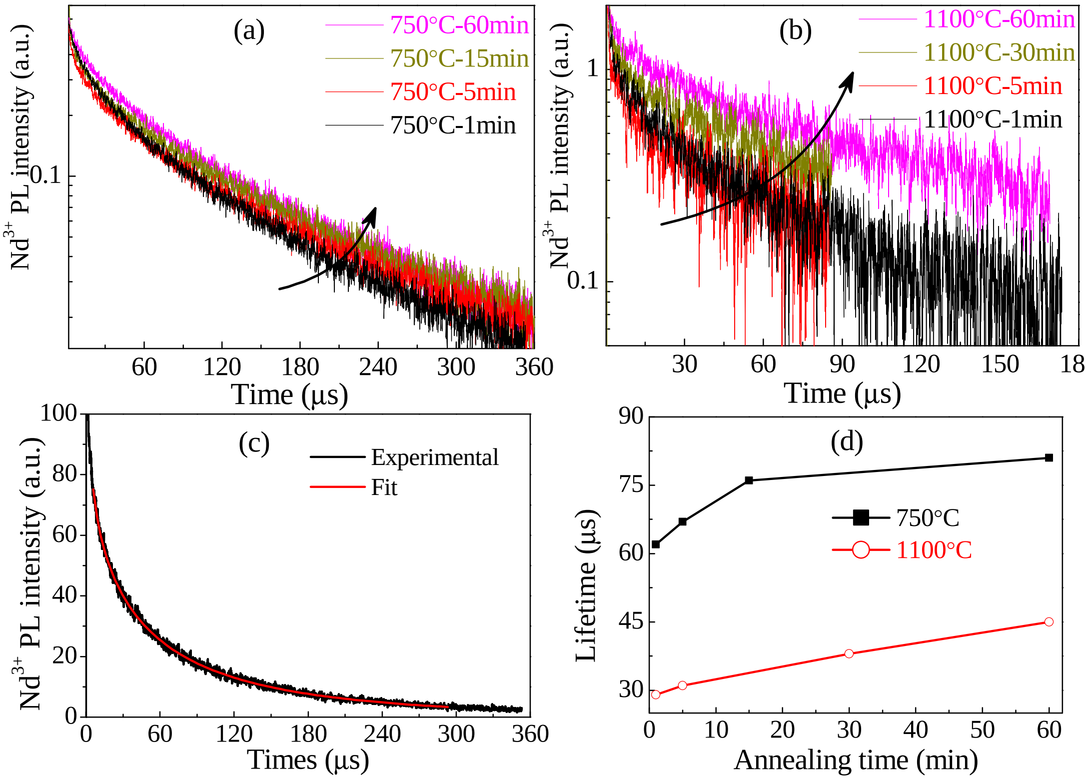

Figure 3.23: Nd^{3+} PL decay curves of Nd-SiO_x films (a) annealed at 750ºC and (b) at 1100ºC for the indicative duration. (c) A typical decay curve of Nd^{3+} PL with its fitting, (d) Evolution of the Nd^{3+} lifetimes with annealing time. The excitation wavelength is 488 nm which is non-resonant for the Nd^{3+} ions.

The Nd^{3+} PL decays versus t_A have been investigated and the results have been displayed in figure 3.23. All the decay curves show a non-exponential nature, which allows to be fitted by a stretched exponential function (Fig. 3.23(c)). The obtained results have been presented in figure 3.23(d). As noticed, the lifetimes gradually increase with t_A at both temperatures: from 62 to 81 µs for 750ºC and from 29 to 45 µs for 1100ºC. It denotes that a longer lifetime is achieved by an extending annealing duration which attests of the recovering of the non-radiative channels. The lifetime at low T_A (750ºC) is higher than that at 1100ºC which has already been ascribed to the growing of Nd_2O_3 clusters at high T_A annealing[26].

3.4.4 Forming gas annealing

To go further in the achievement of optimal Nd^{3+} emission, we have performed annealing treatment under forming gas (95% Ar and 5% H_2) which is recognized as an effective approach to passivate the non-radiative channels and thus to enhance the emission[27], [28]. Herein, we carried out this approach named FG annealing in two ways. A single step in which we replace the N_2 gas by the forming gas and the annealing at required T_A and t_A are carried out. A two-steps annealing in which we proceed first to the typical annealing at high temperature under N_2 gas, and in second step we extend it at 500ºC during 5 hour under FG ambient. These annealing processes were all performed in an RTA furnace.

(a) Single step annealing

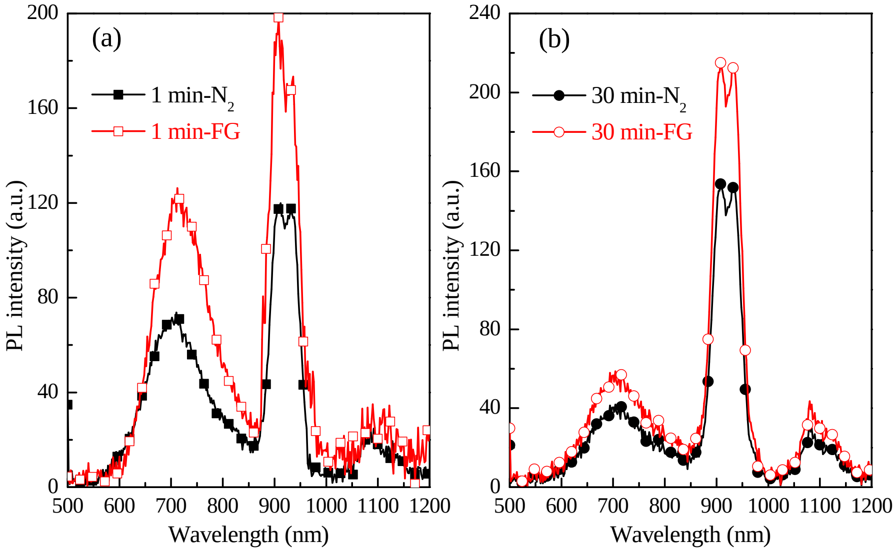

Figure 3.24: PL spectra for samples annealed at 750ºC during (a) 1min. and (b) 30 min. under N_2 gas (solid) and FG ambient (hollow), respectively. The excitation wavelength is 488 nm which is non-resonant for the Nd^{3+} ions.

Figure 3.24 shows the PL spectra of samples annealed under N_2 and FG ambient, respectively. Comparing to N_2 annealing, remarkable enhancements (at least 40%) of intensities for both visible emission and infrared Nd^{3+} PL are obtained after FG annealing whatever the duration applied. It is explained by a passivation of non-radiative defects by hydrogen during annealing. This is also supported by the experimental result (data not shown) that comparable PL intensity is observed when replacing N_2 gas by Ar gas. Note that the obtained intensity by 1min-FG annealing is higher than that achieved after 30min-N_2 annealing. These denote that FG annealing is more powerful than long-duration annealing to passivate the non-radiative defects. Thus, annealing under FG ambient is an effective way to enhance the PL intensity of Nd^{3+} ions.

(b) Two steps annealing

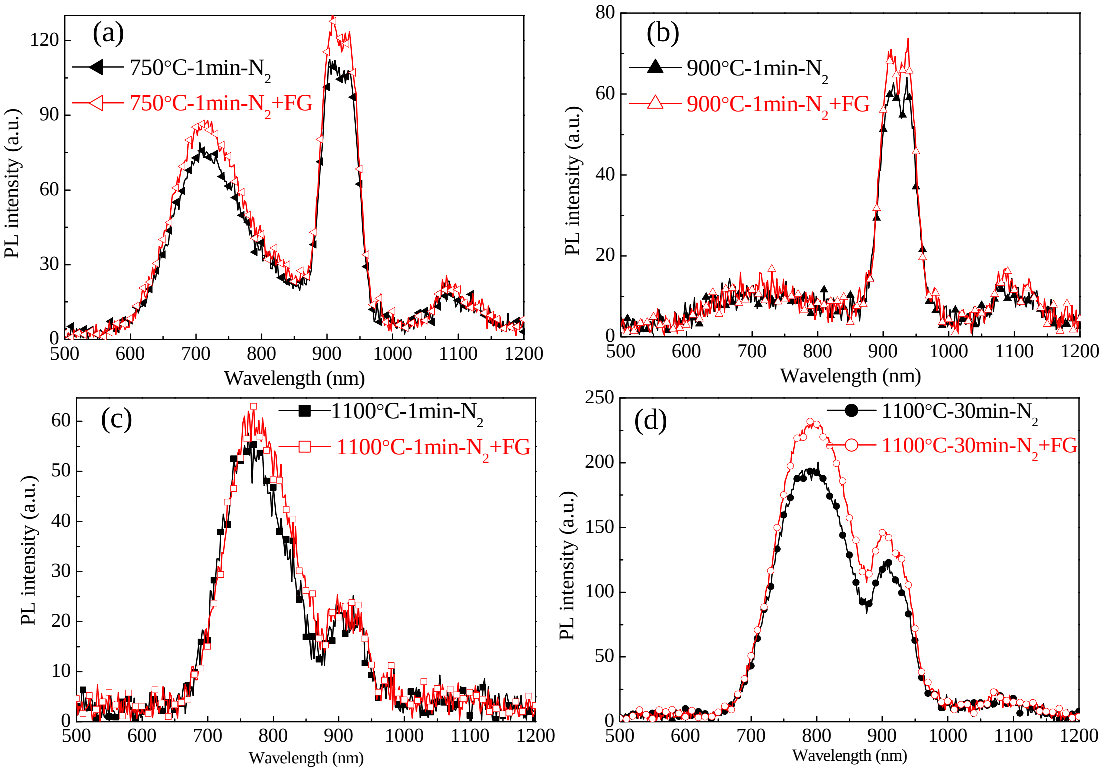

Figure 3.25: PL spectra of samples annealed at the indicative T_A and t_A. The black curves with solid symbol correspond to annealing under N_2 gas, while the red ones with hollow symbol concern the two steps annealing process. The FG in this figure represents a 500ºC-5hour-annealing under forming gas ambient. The excitation wavelength is 488 nm which is non-resonant for the Nd^{3+} ions.

This part aims at investigating an additional annealing under FG ambient at low temperature (500ºC) after a first annealing under N_2 gas at high T_A (750, 900, 1100ºC). For the first step annealing, the Nd^{3+} PL intensity shows a decreasing function when T_A increases from 750 to 1100ºC (Fig. 3.25). The reason has been described above and is ascribed to the lowering number of sensitizers:Nd^{3+} couple due to the formation of Nd_2O_3 clusters. By the second step annealing, the PL intensity shows slightly increase with less than 15% whatever the temperature or the duration applied. This implies that the annealing treatment to which we submit the layer (first step) is sufficient to recover most part of the non-radiative channels present in the matrix. The enhancement of PL intensity by second step annealing is lesser than the previous case of single step annealing under FG ambient. It suggests an importance of the gas nature used in the first step annealing.

3.5 Energy transfer mechanism

To study the mechanism of sensitization of Nd^{3+} ions, we have investigated two kinds of films, SiO_x and Nd-SiO_x, containing the same silicon excess (4.7 at.% estimated by FTIR experiments). The Nd-SiO_x layer corresponds to the optimal sample with Nd content of about 5×10^{19} Nd.cm^{-3}.

3.5.1 PL properties for SiO_x films

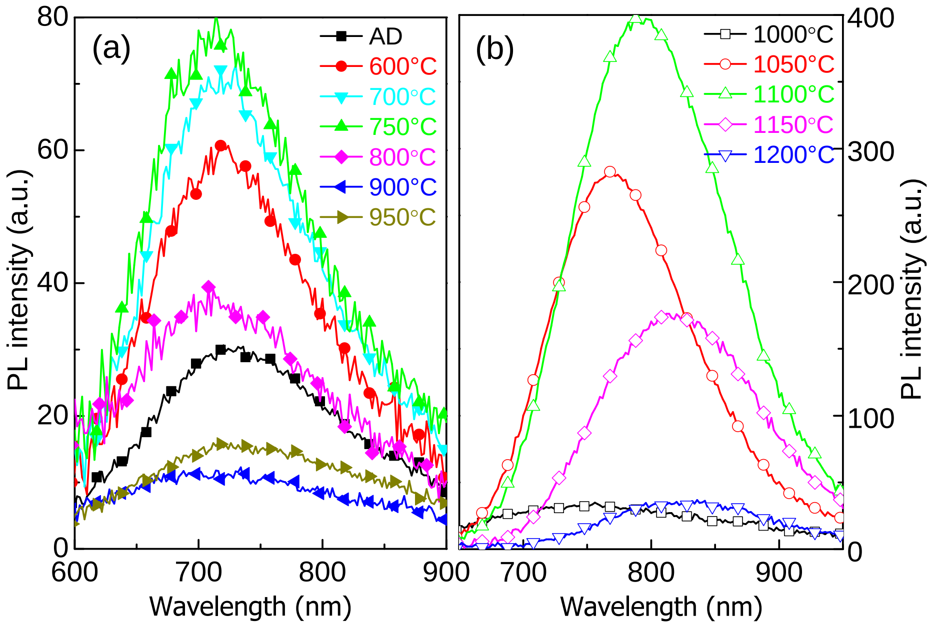

Figure 3.26: The PL spectra of SiO_x films annealed at the indicative temperature during 1 minute. The left graph (a) corresponds to T_A lower than 1000°C while the right one (b) to high T_A higher than 1000°C. AD is the abbreviation of as-deposited. The excitation wavelength is 488 nm.

The PL properties of SiO_x films were investigated as a function of T_A. The spectra are separately shown in figure 3.26 (a) for low T_A less than 1000°C and figure 3.26 (b) for high T_A more than 1000°C. As noticed on these two graphs, the emission bands peak at different wavelengths depending on the T_A range. Thus the emission peaks obtained for low T_A will be defined as E_L while those for high T_A, E_H.

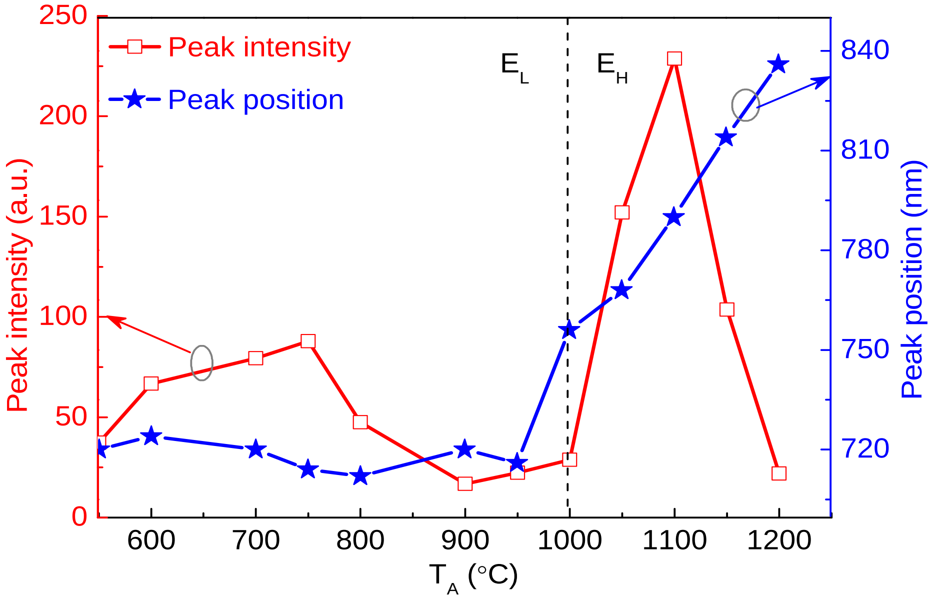

Figure 3.27: Integrated peak intensity (left) and peak maximum position (right) of SiO_x films versus T_A.

The evolutions of the integrated peak intensity and the maximum peak position have been reported as a function of the annealing temperature in figure 3.27. The E_L peak intensity firstly increases to reach a maximum for $T_A = 750$°C before decreasing for higher annealing temperatures. Its position does not change with T_A peaking at around 720 nm. The exact origin of this E_L peak is still unclear. Wang et al.[29] and Wora Adeola et al.[30] have separately observed the very similar E_L peak in their samples. The former attribute it to surface states while the latter to band tails states. Therefore, at this level of discussion, we ascribe this E_L peak to radiative defects states which origin will be specified later. Comparatively for T_A higher than 1000°C, the E_H peak intensity rises up abruptly till a maximum at $T_A = 1100$ºC and thereafter drops down to a very low value for the highest annealing temperature ($T_A = 1200$ºC). However, the maximum E_H intensity is more than three times higher than the one achieved for E_L peak after annealing at $T_A = 750$°C. The band positions red-shift from 756 to 836 nm with increasing T_A, allowing of attributing the E_H peak to the quantum-confined excitonic states in Si-nps[31]. Note that both E_L and E_H peaks are related to the Si excess incorporated in the SiO_2 matrix as no emission was observed from pure SiO_2 sputtered films annealed at any T_A.

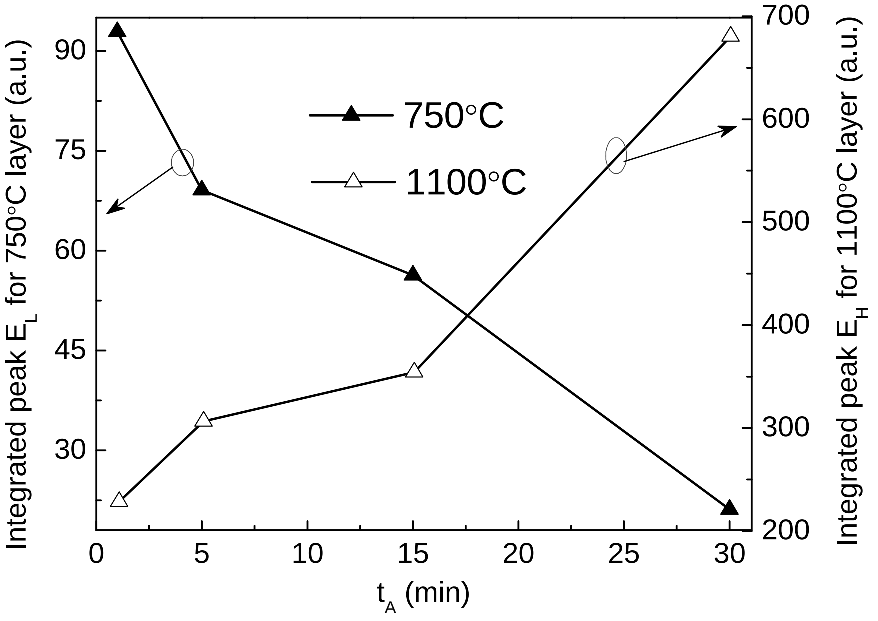

Figure 3.28: E_L and E_H integrated peak intensity versus t_A for SiO_x films annealed at 750°C (left scale) and 1100°C (right scale), respectively. The excitation wavelength is 488 nm.

To further analyze the different PL behaviors between low- and high- T_A layers, two typical annealing temperatures (750 and 1100°C) corresponding to the maximum PL intensities achieved were set to study the effect of annealing time t_A. The evolutions of peak intensity as a function of t_A are presented in figure 3.28. It can be noticed that the E_L peak intensity gradually decreases with time for the 750°C-annealed samples while E_H peak significantly increases for the 1100°C-ones, for the same range of time. This PL evolution is another evidence of different excitation-deexcitation mechanisms: radiative defects controlled at 750°C while quantum confinement controlled at 1100°C. When the annealing duration is increased, the radiative defects are quenched at 750°C probably due to the rearrangement of Si and/or O atoms, while the 1100°C-extended annealing could mainly passivate the non-radiative defects such as stressed bond angles, distorted bond length in host matrix...In high temperature range, Garrido et al.[27] have obtained the same PL behavior versus t_A. They observe that during annealing process the nucleation and growth of Si-nps are almost completed in a few minutes and the average Si-nps diameter remains constant for longer annealing times. Thus increasing annealing time up to 30 min favors achievement of high Si-nps density but remains sufficiently short to avoid the growth of large Si-nps which are detrimental for the quantum confinement process[32]. Moreover, such extra annealing time favors the recovering of the non-radiative channels.

3.5.2 Compared the PL properties of SiO_x to Nd-SiO_x film

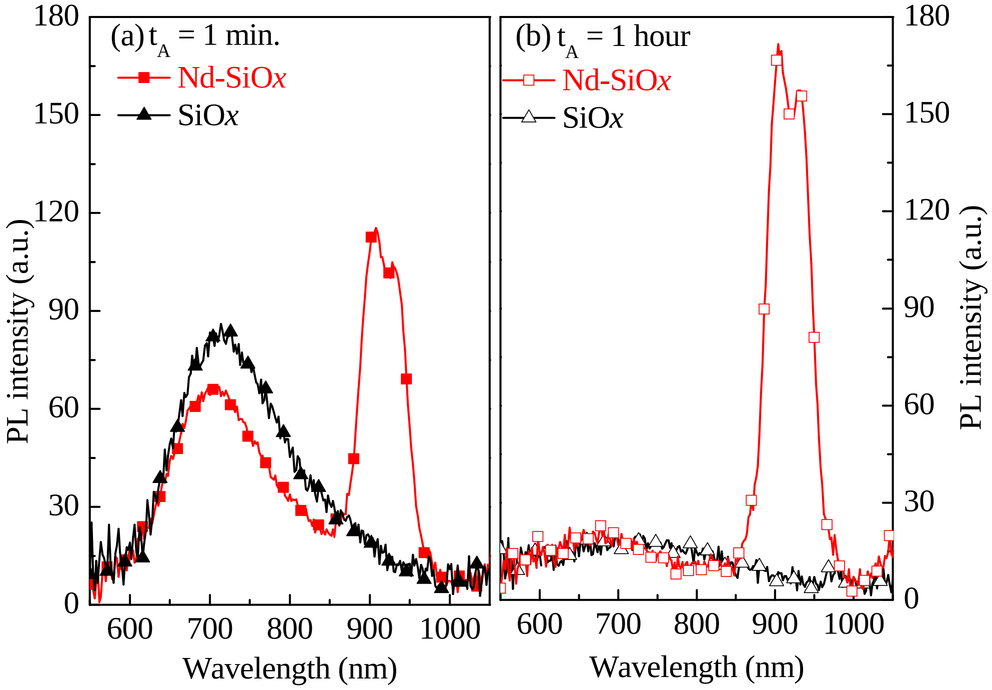

Figure 3.29: PL spectra of Nd-SiO_x and SiO_x films annealed at 750°C during (a) 1 minute and (b) 1 hour. The excitation wavelength is 488 nm which is non-resonant for the Nd^{3+} ions.

To study the excitation mechanism of Nd^{3+} ions in Nd-SiO_x system, PL experiments are performed on Nd-doped SiO_x layers annealed at 750 and 1100°C which correspond to the two temperatures allowing the achievement of the maximum intensity for E_L and E_H peaks, respectively. Figure 3.29(a) shows the PL spectra of Nd-SiO_x and SiO_x films annealed at 750°C during 1 minute. The significant Nd^{3+} PL peak from the deexcitation from the $^4F_{3/2}$ to $^4I_{9/2}$ level at around 920 nm is observed for Nd-doped layer excited with the non-resonant 488nm-Ar laser wavelength. This implies the existence of Nd^{3+} sensitizers present in the SiO_x matrix. The occurrence of an energy transfer from sensitizers to Nd^{3+} ions is evidenced by the concomitant lowering E_L peak intensity compared to that from undoped SiO_x layer.

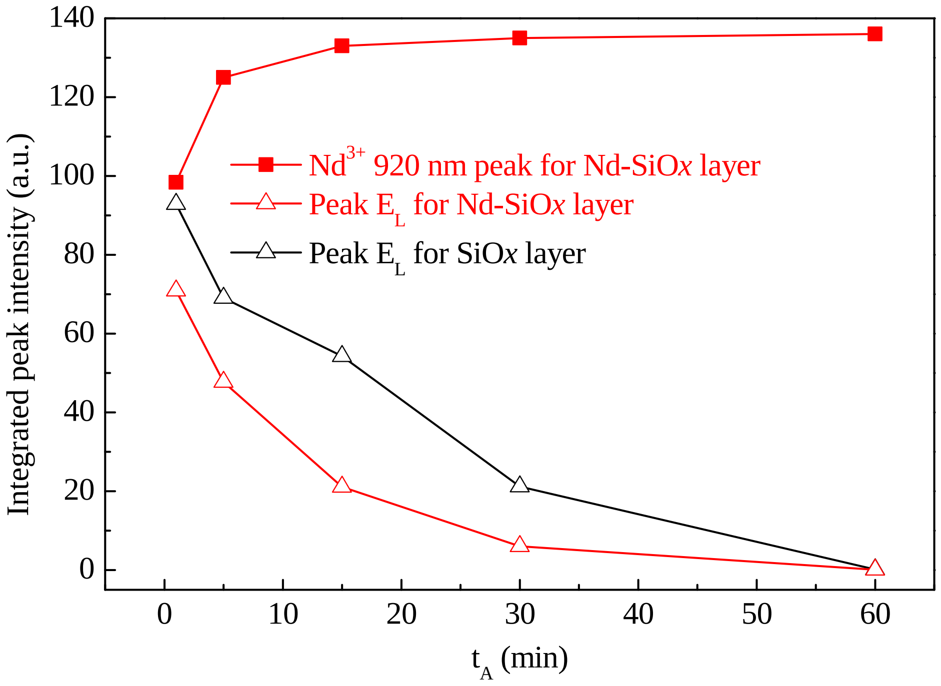

Figure 3.30: Integrated peak intensities of Nd-SiO$_x$ *and SiO*$_x$ *films annealed at 750°C versus t*$_A$*. The excitation wavelength is 488 nm which is non-resonant for the Nd*$^{3+}$ *ions.*

To confirm this behavior investigation of the visible and Nd^{3+} PL intensities as a function of annealing duration has been carried out (Fig. 3.30). One can noticed that the visible E$_L$ peak intensity decreases versus t$_A$ for both SiO$_x$ and Nd-SiO$_x$ films. As explained above, this evolution can be ascribed to the recovering of the radiative defects. For at least t$_A$ $\leq$ 30 min, the E$_L$ peak intensity from Nd-doped SiO$_x$ layer annealed at 750°C shows a lower value than that of undoped one. Such a behavior is an evidence of an efficient energy transfer from these radiative defects to Nd^{3+} ions states, playing the role as Nd^{3+} sensitizers as mentioned above. Concerning the Nd^{3+} emission evolution at 920 nm, it increases until 15 min. of annealing and saturates afterward. Such saturation may be attributed to (i) the passivation of some non-radiative defect and/or (ii) the existence of another type of sensitizers. Moreover, we have observed in the figure 3.28 a decrease of the low T$_A$ type Nd^{3+} sensitizer (E$_L$ peak) with longer annealing, which should contribute to a decrease of the Nd^{3+} PL intensity. Consequently those trends of visible and Nd^{3+} PL intensities are a signature of the existence of another type of sensitizers that also excite efficiently the Nd^{3+} ions (Fig. 3.29(b)). As demonstrated in our previous work[33], such sensitizers grown at low T$_A$ contain a few Si atoms (less than 15 atoms) and will be here named atomic scale sensitizers (ASS). They differ from the luminescence centers proposed by Savchyn et al.[34] since using also a RTA of 100 s, they observed always a PL peak position shift which is in disagreement with our results (seen Fig. 3.26(a)).

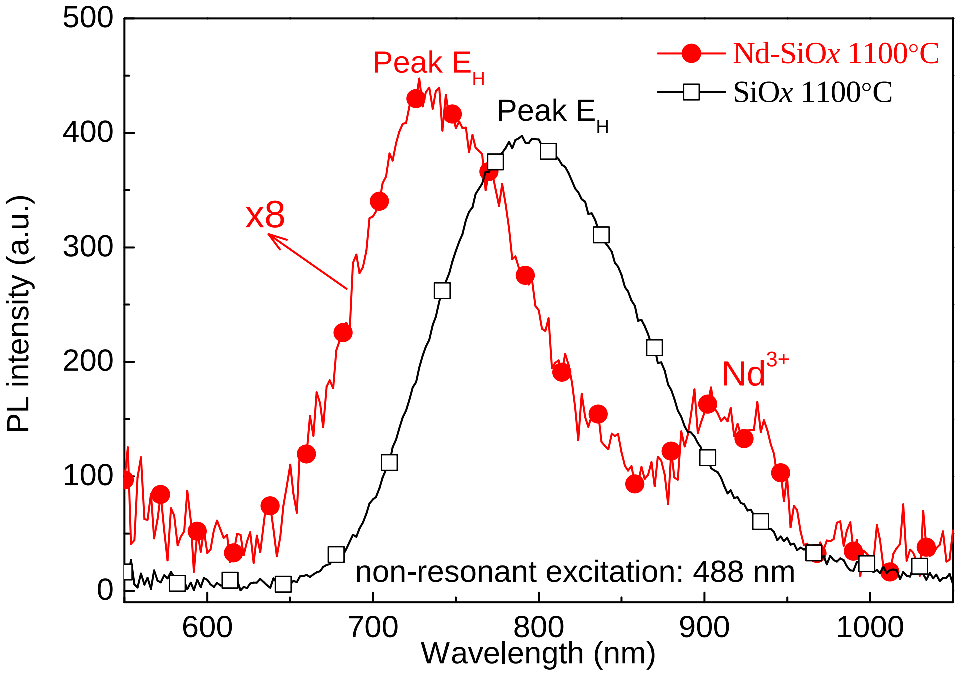

Figure 3.31: PL spectra of both Nd-SiO$_x$ and SiO$_x$ films annealed for 1 minute at 1100°C. The excitation wavelength is 488 nm which is non-resonant for the Nd^{3+} ions.

When annealed at higher temperature (1100°C), the intensity of E_H peak falls down by about 8 times after Nd incorporation (Fig. 3.31). It is thus supposed that most of emitters transfer energy to their nearby Nd^{3+} ions. One can notice that the position of E_H peak shifts from about 790 to 730 nm after Nd incorporation. This shift is probably explained by the two Nd^{3+} absorption bands peaking at about 750 and 808 nm[35] and is a confirmation of the energy transfer process involved. Nevertheless, the Nd^{3+} PL intensity achieved at such T_A appears very low. This demonstrates the E_H peak emitters formed at this high temperature act as sensitizer of Nd^{3+} ions, but unfortunately, this efficient energy transfer process suffers from Nd_2O_3 clusters formation and/or a too large sensitizer-Nd^{3+} distance. This can explain that the drop of Si-nps PL does not lead to a high PL emission of the Nd^{3+} ions. In addition, the effect of annealing duration was investigated at 1100°C. The E_H peak intensity of Nd-SiO$_x$ film gradually increases with increasing t_A (data not shown here), presenting thus a similar trend to that achieved for undoped layer (Fig. 3.28).

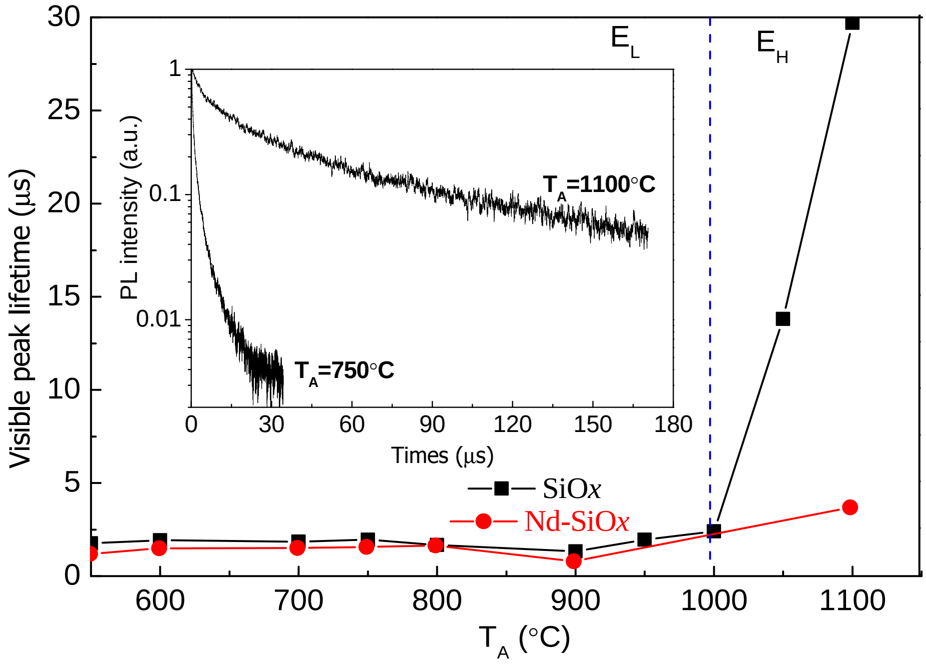

Figure 3.32: Evolution of PL lifetimes measured on peak E_L and E_H versus T_A for 1min-annealed SiO_x and Nd-SiO_x films excited at 488 nm and detected at the maximum point of each peak. The inset shows the PL decay curves for SiO_x films annealed at 750 and 1100ºC.

Lifetimes τ measured on E_L and E_H peaks do not show a single exponential trend, therefore as a first approach the integrated equation (3. 6)[36] was used in order to fit the decay curve:

$$\tau = \int \frac{I}{I_0} \mathrm{d}t, \tag{3.6}$$

where I is a time dependent peak intensity while I_0 is the intensity at t = 0 s. For E_L peak, the lifetimes of both doped and non-doped films are low and invariable at about 2 µs as shown in figure 3.32. This confirms that the visible E_L peak origins from the defects.[37] For E_H peak from non-doped SiO_x film, the lifetime increases dramatically and holds a value of 29 µs for 1100ºC-SiO_x film. This value is indicative that E_H peak originates from the exciton recombination in Si-nps.[38] In contrast for Nd-SiO_x film annealed at 1100ºC, this lifetime value decreases to 3.6 µs. This decrease is due to the energy transfer to Nd^{3+} ions as described by the effective lifetime deduced from rate equation[39] in the sensitizer : Nd system:

$$\tau_{\text{Nd-}SiO_x} = \frac{\tau_{SiO_x}}{1 + KN^0_{Nd}\tau_{SiO_x}} \tag{3.7}$$

where $\tau_{Nd\text{-}SiOx}$ is the E_L or E_H peak lifetime for Nd-SiO$_x$ film while τ_{SiOx} corresponds to the non-doped SiO$_x$ film lifetime; K is the coupling constant between sensitizers and Nd^{3+} ions; N_{Nd}^0 is the Nd^{3+} density in the fundamental state. The term $KN_{Nd}^0\tau_{SiOx}$ describes phenomenologically^{44} the coupling between sensitizers and Nd^{3+} ions. Therefore, the decrease of $\tau_{Nd\text{-}SiOx}$ with respect to τ_{SiOx} can be ascribed to the increase of the coupling term $KN_{Nd}^0\tau_{SiOx}$ and thus evidences the energy transfer to Nd^{3+} ions. In Nd-SiO$_x$ films annealed at T_A<1000ºC, the lifetime $\tau_{Nd\text{-}SiOx}$ is slightly lower than τ_{SiOx} taking into account our experimental uncertainties. For layers annealed at T_A>1000ºC the lifetime $\tau_{Nd\text{-}SiOx}$ is 10 to 20 times lower than SiO$_x$ lifetime (Fig. 3.32). Consequently, for low T_A Nd-SiO$_x$ layers have a weaker coupling term $KN_{Nd}^0\tau_{SiOx}$ compared to higher one. The efficiency η of energy transfer can be estimated by the following equation:[40]

$$\eta = 1 - \frac{\tau_{Nd-SiOx}}{\tau_{SiOx}} \qquad (3.8)$$

One can obtain that in Nd-SiO$_x$ films annealed at T_A<1000ºC, the efficiency is lower than 10%, while η reaches about 90% for 1100ºC-annealed layer. Notwithstanding, the weaker sensitizer:Nd coupling regime or lower efficiency for the low T_A, the highest PL intensity is achieved. Such a feature can be explained by the larger number of sensitized Nd^{3+} ions due to the larger density of both radiative defects and atomic scale sensitizers (low T_A) than that of Si-nps sensitizers (high T_A).

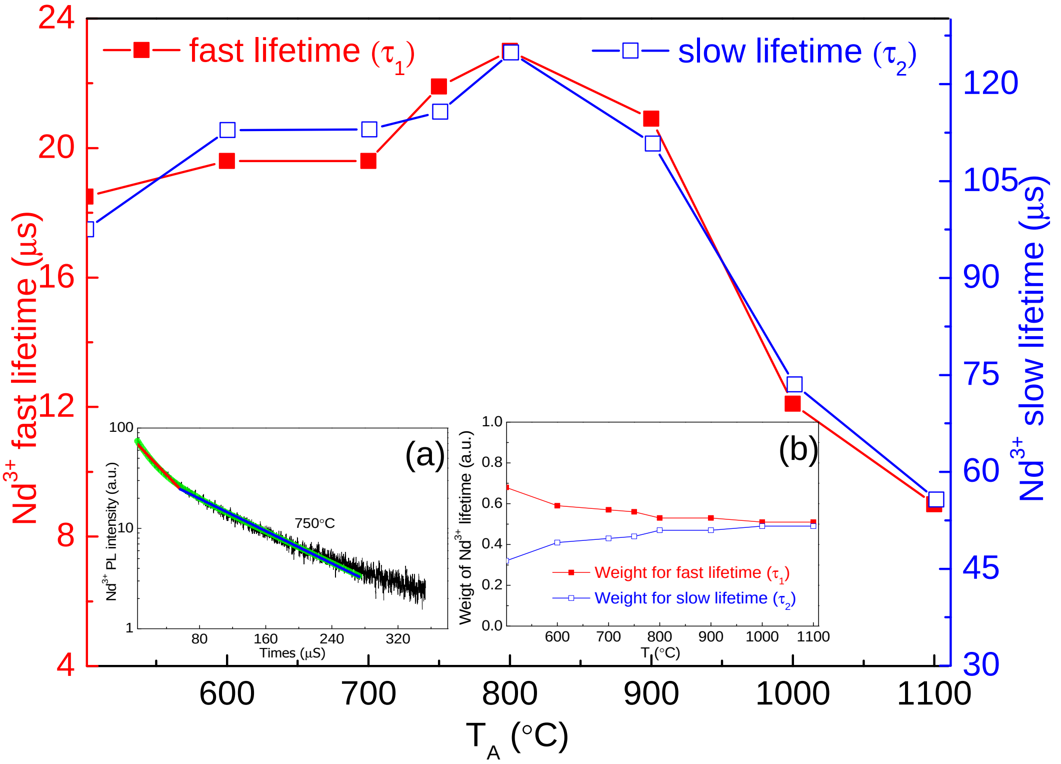

Figure 3.33: Evolution of Nd^{3+} PL lifetime at 920 nm versus T_A. The inset (a) is a representative decay rate of 750°C Nd-SiO_x PL, fitted by a two-exponential decay model, while the inset (b) is the component of Nd^{3+} fast or slow lifetime.

The decay rate of Nd^{3+} infrared PL at 920 nm has a non-exponential nature as seen from the figure 3.33 inset (a). For all the films, the Nd^{3+} PL decay rate was fitted by a two-exponential decay model:

$$I(t) = A_1 \exp(-\frac{t}{\tau_1}) + A_2 \exp(-\frac{t}{\tau_2})\,. \tag{3.9}$$

Fast (τ_1) and slow lifetimes (τ_2) have been reported in figure 3.33, and the corresponding component of lifetime ($A_1/(A_1+A_2)$, $A_2/(A_1+A_2)$) is described in the inset (b). On one hand, the fast lifetime is shorter than 24 µs, while the slow one is in the 50-130 µs range. It is observed that both of them gradually increase followed by a dramatic decrease. The maximum is achieved after an annealing at T_A=800ºC. This evolution versus T_A is comparable to the results reported by Li et al.[15] explaining that the local environment of Nd^{3+} ions is deteriorated because of the formation of Nd_2O_3 clusters after annealing at high temperatures. Such a rare earth clusterization has been also observed in a similar sputtered system as demonstrated in our study using atom probe tomography technique[33]. On the other hand, the component of fast lifetime decreases from 0.68 to 0.51, in figure 3.33 inset (b), while the slow case increases from 0.32 to 0.49. This indicates that (i) the fast lifetime dominates the Nd^{3+} emission for all the layers, and that (ii) the contribution of slow lifetime to Nd^{3+} PL gradually increases with T_A.

3.5.3 Interactions between sensitizers and Nd^{3+} ions

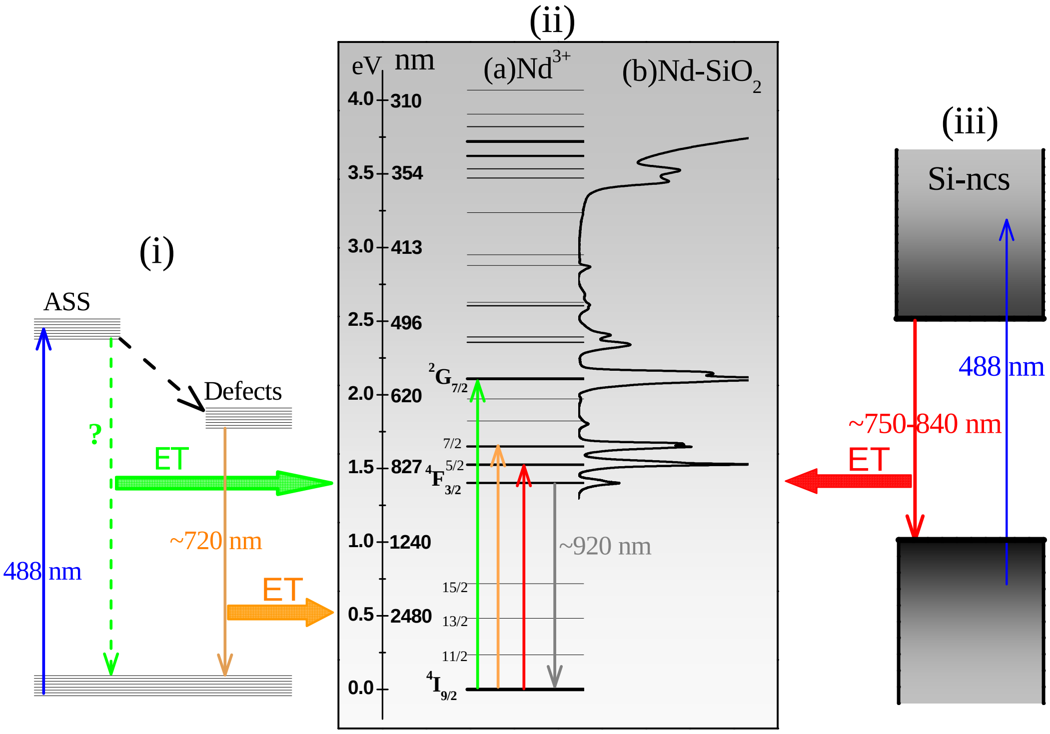

Figure 3.34: Schematic illustrations of the Nd^{3+} ions excitation. (i) Energy diagrams of atomic scale sensitizers (ASS) and defects within the films annealed at T_A <1000°C, (ii) (a) energy diagram of Nd^{3+} ions and (b) absorption spectrum of Nd^{3+} ions doped in SiO_2 film, and (iii) energy diagram of Si-nps within the films annealed at T_A>1000°C. ET is the abbreviation of energy transfer.

The energy transfer from sensitizers present in SiO_x matrix to Nd^{3+} ions has been demonstrated using a non-resonant excitation as described above and now our purpose is to analyze this transfer process in more details (Fig. 3.34). The absorption spectrum (Fig. 3.34(iib)) of Nd^{3+} ions in Nd-doped SiO_2 film presents four typical absorption bands peaking at about 880, 808, 750, and 585 nm. They correspond to the transitions from the ground level $^4I_{9/2}$ to the excited level $^4F_{3/2}$, $^4F_{5/2}$, $^4F_{7/2}$, and $^2G_{7/2}$, respectively.[1] Thus, from these quantified energy levels and the positions of E_L and E_H emissions, one can propose a scheme of the transfer mechanism as detailed in figure 3.34.

For low T_A-annealed Nd-SiO_x layers, ASS and radiative defects are present in the matrix. Both efficiently sensitize the Nd^{3+} ions, since the intense Nd^{3+} PL has been observed in both samples annealed at 750°C 1min and 1 hour (Fig. 3.34). When the radiative defects are recovered with T_A, the atomic scale sensitizers, whose density increases with the temperature, dominate the sensitization of the rare earth ions. As a consequence, in this intermediate temperature range, two paths of sensitization of Nd^{3+} ions will coexist and are at the origin of the radiative recombination from the $^4F_{3/2}$ to the ground state $^4I_{9/2}$ level with an emission at about 920 nm.

In the case of high T_A-annealed Nd-SiO_x layers, the formed Si-nps have a smaller band gap than in the case of atomic scale sensitizers. These Si-nps can also transfer their energy to Nd^{3+} ions as demonstrated by the decreasing of Si-nps PL intensity (Fig. 3.31) as well as its lifetime (Fig. 3.32). But the PL intensity of Nd^{3+} ions achieved after such a treatment is low. Such a feature can be attributed to two phenomena: (i) a cross relaxation process among Nd^{3+} ions occurs due to the formation of Nd_2O_3 clusters as witnessed by its lifetimes (Fig. 3.33), (ii) the formation of Si-nps as already observed in similar sample doped with Er ions[41] will lead to an increase of the sensitizer:Nd distance.

For all the Nd-SiO_x layers, a Nd^{3+} ions PL decay with a non-exponential nature was observed and has been fitted using a double exponential decay model leading to the determination of a fast and a slow components. They present an opposite behavior with the annealing temperature (inset (b) in Fig. 3.33): the former decreases while the latter increases. Horak et al.[42] have attributed the shortening of the decay time to a modification of local density of states (LDOS) brought by the Si interface. This is consequently a signature of the distance between rare earth ions and sensitizer. Considering that higher will be the annealing temperature stronger will be the phase separation in our layers,[43] high temperature results in a larger the Sensitizer : Nd^{3+} distance. Thus, one can explain the two lifetime components of the PL decay to the different environment of Nd^{3+} ions which is modified by the annealing treatment. This would explain the observed increase of the ratio of slow over fast components of PL decay with temperature.

3.6 Conclusion:

The Si excess in Nd-doped SRSO layers has been engineered by monitoring the hydrogen rate (r_H) for reactive co-sputtering approach or by tuning the RFP_{Si} for classical co-sputtering approach. The Si excess was calculated by both ellipsomtery and FTIR methods. The maximum Nd^{3+} PL was obtained from the sample containing 4.7 at.% Si excess (from FTIR experiments) deposited by classical co-sputtering approach. Moreover, the Nd content was adjusted by controlling the RFP_{Nd2O3}. It is to note that we have also evidenced an effect of the RFP_{Si} on Nd concentration. Via RBS experiments, the optimal film was estimated to contain about 5.0×10^{19} Nd.cm^{-3}. Numerous annealing treatments were performed on the sample with both optimized Si excess and Nd content. Firstly, we have investigated the influence of annealing temperature T_A concerning two approaches. RTA approach can significantly enhance the Nd^{3+} PL with respect to as-deposited layer with an optimized T_A in moderate range (700-800ºC). Similar evolution of Nd^{3+} PL versus T_A has been observed for Conventional Annealing method. A high Nd^{3+} PL was achieved at moderate T_A due to high density of sensitizers present in Nd-SRSO layer. For increasing T_A higher than 1000ºC, this Nd^{3+} PL was decreased attributing to both formation of Nd_2O_3 clusters and the increasing sensitizer:Nd^{3+} distance. Secondly, the effect of annealing duration t_A from 1 min to 60 min has been explored. It is found that the infrared Nd^{3+} PL intensity was increased at whatever T_A ascribed to growing more sensitizers and/or passivating non-radiative channels. Thirdly, the annealing under FG ambient is noticed as another effective way to enhance the Nd^{3+} PL intensity due to the passivation of non-radiative defects by hydrogen. In order to study the mechanism of excitation towards Nd^{3+} ions, we began with the visible emission originating from host matrix. This emission for T_A<1000ºC was suppressed with longer t_A while T_A>1000ºC annealing can favor such emission. It has been demonstrated that the visible peak at T_A<1000ºC is attributed to defects levels, while at T_A>1000ºC quantum confinement effect rules the visible emission. The radiative defects have less than 10% efficiency of energy transfer to Nd^{3+} ions, contrarily the quantum confined Si-nps hold as high as 90% efficiency. Then, we have evidenced that two kinds of sensitizers (radiative defects and atomic scale sensitizers) towards Nd^{3+} ions would coexist for T_A<1000ºC Nd-SRSO films, while Si-nps were grown acting as sensitizer for higher T_A films.

Bibliography

---

[1] D. Bréard, F. Gourbilleau, A. Belarouci, C. Dufour, R. Rizk, J. lumin. **121** (2006) 209

[2] D. Bréard, F. Gourbilleau, C. Dufour, R. Rizk, J. L. Doualan, P. Camy, Mater. Sci. Eng. B **146** (2008) 179

[3] L. Khomenkova, F. Gourbilleau, J. Cardin, R. Rizk, Physica E **41** (2009) 1048

[4] K. Hijazi, L. Khomenkova, F. Gourbilleau, J. Cardin, R. Rizk, J. lumin. **129** (2009) 1886

[5] R. Nalini, Films minces à base de Si nanostructuré pour descellules photovoltaïques de 3ème génération. PhD thesis, Universite de caen/Basse-Normandie, (2012)

[6] J. E. Olsen, F. Shimura, J. Appl. Phys. **66** (1989) 1353

[7] F. Iacona, G. Franzò, C. Spinella, J. Appl. Phys. **87** (2000) 1295

[8] E. Quiroga-González, W. Bensch, M. Aceves-Mijares, Z. Yu, R. López-Estopier, K. Monfil-Leyva, Thin solid films **519** (2011) 8030

[9] K. Watanabe, H. Tamaoka, M. Fujii, K. Moriwaki, S. Hayashi, Physica E **13** (2002) 1038

[10] K. Watanabe, M. Fujii, S. Hayashi, J. Appl. Phys. **90** (2001) 4761

[11] K. Hijazi, R. Rizk, J. Cardin, L. Khomenkova, F. Gourbilleau, J. Appl. Phys. **106** (2009) 024311

[12] H. Rinnert, M. Vergnat, G. Marchal, A. Burneau, Appl. Phys. Lett. **72** (1998) 3157

[13] S. Y. Seo, M. J. Kim, J. H. Shin, Appl. Phys. Lett. **83** (2003) 2778

[14] A. N. MacDonald, A. Hryciw, F. Lenz, and A. Meldrum, Appl. Phys. Lett. **89** (2006) 173132

[15] R. Li, S. Yerci, S. O. Kucheyev, T. van Buuren, L. Dal Negro, Opt. express **19** (2011) 5379

[16] L. Skuja, J. Non-Cryst. Solids **239** (1998) 16

[17] H. J. Fitting, T. Barfels, A. N. Trukhin, B. Schmidt, A. Gulans, A. von Czarnowski, J. Non-Cryst. Solid **303** (2002) 218

[18] S. Cueff, C. Labbé, B. Dierre, F. Fabbri, T. Sekiguchi, X. Portier, R. Rizk, J. Appl. Phys. **108** (2010) 113504

[19] O. Debieu, J. Cardin, X. Portier, F. Gourbilleau, Nanoscale Res. Lett. **6** (2011) 161

[20] C. Jacinto, S. L. Oliveira, L. A. O. Nunes, J. D. Myers, M. J. Myers, T. Catunda, Phys. Rev. B **73** (2006)125107

[21] E. Steveler, H. Rinnert, M. Vergnat, J. Appl. Phys. **110** (2011) 113518

[22] J. E. Olsen, F. Shimura, J. Appl. Phys. **66** (1989) 1353

---

[23] B. Yan, J. H. Dias da Silva, P. C.Taylor, J. Non-Cryst. Solids **227** (1998) 528

[24] C.-H. Liang, J. Cardin, C. Labbé, F. Gourbilleau, J. Appl. Phys. **114** (2013) 033103

[25] S. Cueff, C. Labbé, O. Jambois, B. Garrido, X. Portier, R. Rizk, Nanoscale Res. Lett. **6** (2011) 395

[26] M. Shah, M. Wojdak, A. J. Kenyon, M. P. Halsall, H. Li, I. F. Crowe, J. Lumin. **132** (2012) 3103

[27] B. Garrido Fernandez, M. López, C. García, A. Pérez-Rodríguez, J. R. Morante, C. Bonafos, M. Carrada, A. Claverie, J. Appl. Phys. **91** (2002) 798

[28] S. P. Withrow, C. W. White, A. Meldrum, J. D. Budai, D. M. Hembree, J. C. Barbour, J. Appl. Phys. **86** (1999)396

[29] M. Wang, D. Yang, D. Li, Z. Yuan, D. Que, J. Appl. Phys. **101** (2007)103504

[30] G. Wora Adeola, H. Rinnert, P. Miska, M. Vergnat, J. Appl. Phys. **102** (2007) 053515

[31] N. M. Park, C. J. Choi, T. Y. Seong, S. J. Park, Phys. Rev. Lett. **86**, (2001)1355

[32] M. Roussel, E. Talbot, P. Pareige, F. Gourbilleau, J. Appl. Phys. **113** (2013) 063519

[33] E. Talbot, R. Larde, P. Pareige, L. Khomenkova, K. Hijazi, F. Gourbilleau, Nanoscale Res. Lett. **8** (2013) 39

[34] O. Savchyn, F. R. Ruhge, P. G. Kik, R. M. Todi, K. R. Coffey, H. Nukala, H. Heinrich, Phys. Rev. B **76** (2007) 195419

[35] D. Breard, F. Gourbilleau, A. Belarouci, C. Dufour, and R. Rizk, J. Lumin. **121** (2006) 209.

[36] Y. H. Xie, M. S. Hybertsen, W. L. Wilson, S. A. Ipri, G. E. Carver, W. L. Brown, E. Dons, B. E. Weir, A. R. Kortan, G. P. Watson, A. J. Liddle, Phys. Rev. B **49** (1994) 5386

[37] L. N. Dinh, L. L. Chase, M. Balooch, W. J. Siekhaus, F. Wooten, Phys. Rev. B **54** (1996) 5029

[38] M. L. Brongersma, A. Polman, K. S. Min, E. Boer, T. Tambo, H. A. Atwater, Appl. Phys. Lett. **72** (1998) 2577

[39] B. Garrido, C. Garc_ıa, S. Y. Seo, P. Pellegrino, D. Navarro-Urrios, N. Daldosso, L. Pavesi, F. Gourbilleau, R. Rizk, Phys. Rev. B **76** (2007) 245308

[40] P. Vergeer, T. J. H. Vlugt, M. H. F. Kox, M. I. den Hertog, J. P. J. M. van der Eerden, A. Meijerink, Phys. Rev. B **71** (2005) 014119

[41] F. Gourbilleau, M. Levalois, C. Dufour, J. Vicens, and R. Rizk, J. Appl. Phys. **95** (2004) 3717

[42] P. Horak, W. H. Loh, A. J. Kenyon, Opt. Express **17** (2009) 906

[43] M. Roussel, E. Talbot, P. Pareige, F. Gourbilleau, J. Appl. Phys. **113** (2013) 063519

Chapter 4: A study on Nd doped Si-rich silicon nitride films

4.1 Introduction

The optimized emission from Nd^{3+} ions in Nd-SRSO layers has been achieved in chapter 3. In this chapter, we will focus our study on the emission of Nd-SRSN films. Since, as mentioned in chapter 1, the SRSO and SRSN are two typical Si-based matrices with different optical properties. We thus expect to observe different behavior of Nd^{3+} ions luminescence in SRSN host matrix comparing to SRSO one. We will here investigate the effect of composition (Si excess and Nd content) and post-annealing treatments on the structural and optical properties of Nd-SRSN layers. For this purpose, the films have been fabricated using the reactive co-sputtering method since, as described in chapter 2, no Nd^{3+} emission has been observed from the layers deposited by the classical co-sputtering approach. Two annealing processes, i.e. rapid thermal annealing (RTA) and/or classical annealing (CA), will be performed.

4.2 Effect of Si excess incorporated

4.2.1 Fourier transform infrared spectroscopy

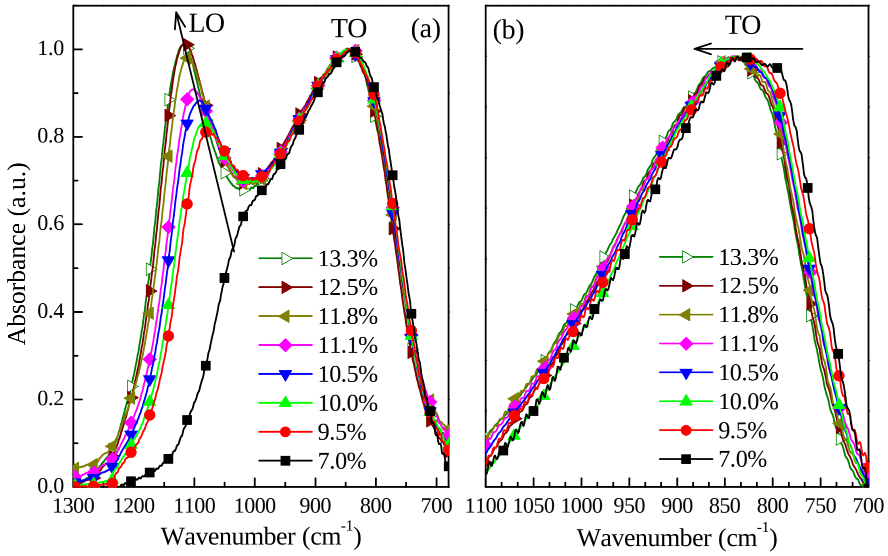

Figure 4.1: FTIR spectra recorded with (a) an incidence angle of 65° and (b) a normal incidence for as-deposited Nd-SRSN layers produced by the indicated $N_2/(N_2+Ar)$ nitrogen rates (r_N).

Figure 4.1 shows the evolution of the FTIR spectra recorded with (a) an incidence angle of 65° and (b) a normal incidence for as-deposited Nd-SRSN films prepared with the indicative r_N. All the spectra are normalized to the intensity of TO band centered at about 830 cm^{-1}. In figure 4.1(a), the TO band only changes slightly with r_N, whereas the evolution of LO band in the range of 970-1150 cm^{-1} is more pronounced. A significant blue-shift of LO peak position and a concomitant increase of its intensity with increasing r_N can be noticed. Similar behaviors have been reported in SRSN thin films by Huang et al.[1], and have been ascribed to the decreasing of the Si excess in the host matrix. In figure 4.1(b), the TO band shifts to high wavenumbers. This shift is limited compared to the previously mentioned Nd-SRSO material due to the more "rigid" SRSN bond structures[2]. Yerci et al.[3] have observed this similar blue-shift when the Si content decreases. Hasegawa et al.[4] have ascribed it to the decrease of the Si-N bond length due to the compositional change of the nitride layers. As a consequence, using the relation described in Sect. 2.2.1 Chap. 2, the Si excess incorporated in our layers has been estimated and is found ranging from 30.1 to 9.6 at.% when r_N varies from 7.0% to 13.3%.

The ordered degree of the layer can also be characterized using FTIR experiments. Yerci et al.[3] assume that the full width at half maximum (FWHM) of the TO band is related to the matrix quality. They notice that the FWHM is inversely proportional to the Si excess. Molinari et al.[5] explain that the increase of the structural disorder is caused by the nitrogen in Si-rich SiN_x:H alloy responsible of the widening of the band tail states. However, we do not observe any change of FWHM (Fig. 4.1(b)), while the two TO and LO bands (Fig. 4.1(a)) gradually separate with r_N. This is the signature of the ordering of the films with the incorporation of nitrogen in the matrix.

4.2.2 Ellipsometry

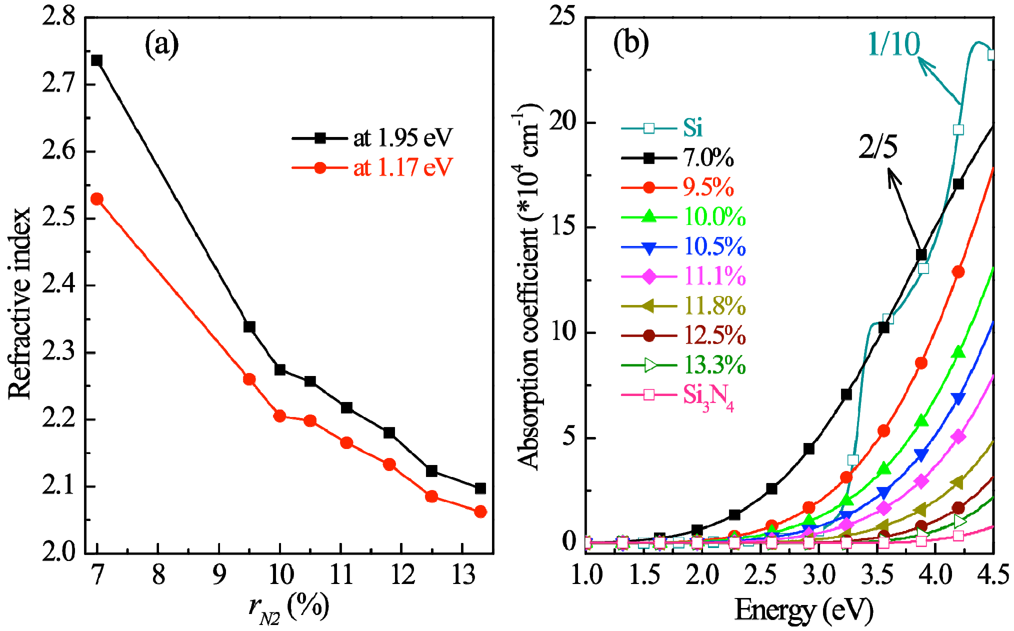

Figure 4.2: For as-deposited layers, (a) refractive index evolution as a function of the nitrogen rate r_N for two energies, 1.17 and 1.95 eV; (b) absorption coefficient versus energy from 1.0 to 4.5 eV for different r_N investigated and pure Si_3N_4 and Si layers.

The values of refractive index (n) and absorption coefficient (α) have been deduced from the ellipsometry measurements (Sect. 2.2.2 Chap. 2). Figure 4.2(a) represents the refractive index evolution as a function of the hydrogen rate r_N for two energies, 1.17 and 1.95 eV. As in the case of the SRSO doped layers, the value of n = 1.17 eV is considered for the design of a single mode waveguide at the 1.06 µm wavelength (See Sect. 5.2 Chap. 5). Both curves show a decrease with r_N which demonstrates that the increase of the nitrogen content in the plasma diminishes the silicon incorporation in the Si_3N_4 matrix. This evolution confirms the results obtained by FTIR. The minimum value of n achieved at 1.95 eV is 2.1 for r_N = 13.3%, higher than the value of 1.85 for Si_3N_4[4] [6]. This result demonstrates that the layer contains a Si excess. Figure 4.2(b) displays the absorption coefficient of thin films versus energy from 1.0 to 4.5 eV for different nitrogen rates investigated as well as pure Si_3N_4 and Si. The absorption coefficient α is lower than 10^3 cm^{-1} from 1.0 to 1.5 eV in a reduced range with respect to the SRSO ones. For higher energies, it can reach some tens of 10^4 cm^{-1} and is about two times higher than the one achieved for the SRSO layers

(Sect. 3.2.2 Chap. 2). All these curves are between those of Si_3N_4 and Si materials, confirming the incorporation of Si excess by decreasing r_N.

4.2.3 Estimation of Si excess

(a) From FTIR analysis

As already described in sect. 2.2.1 of chap. 2, one can determine the N/Si ratio (x) through the maximum peak position of LO band in FTIR spectra. By increasing the r_N from 7.0% to 13.3%, as shown in table 4.1, the LO position gradually shifts from 978 to 1111cm^{-1}. The x value thus changes from 0.66 to 1.07. The atomic percentage of Si excess estimated from the obtained x value shows a decrease from 30.1 to 9.6 at.% with the incorporation of nitrogen during the process. The high value of absorption measured for the low nitrogen rate can be then ascribed to the high Si content incorporated in the nitride matrix.

	FTIR			Ellipsometry		
r_N (%)	W_{LO} (cm^{-1})	x=N/Si	Si excess (at.%)	n at 1.95 eV	x=N/Si	Si excess (at.%)
7.0	978	0.66	30.1	2.736	0.66	30.1
9.5	1065	0.93	15.9	2.338	0.92	16.2
10.0	1073	0.95	14.7	2.274	0.96	14.0
10.5	1082	0.98	13.5	2.257	0.98	13.5
11.1	1089	0.10	12.5	2.218	1.01	12.2
11.8	1102	1.04	10.8	2.180	1.04	10.9
12.5	1107	1.06	10.2	2.123	1.08	9.0
13.3	1111	1.07	9.6	2.097	1.11	8.1

Table 4.1 Si excess is estimated by FTIR in left part and from refractive index n in right part for the as-deposited samples. The uncertainty of W_{LO} value is 1 cm^{-1} while n value is 0.002.

(b) From ellipsometric spectroscopy analysis

In Sect.2.2.1 of Chap. 2, I have described the relationship allowing the determination of the N/Si ratio (x) from the values of refractive index obtained by fitting the ellipsometry spectra. The approach considering a combination between the chemical bonds density and refractive index was used in this work. As shown in the right part of table 4.1, the obtained x values raise from 0.66 to 1.11 while the refractive indices drop from 2.736 to 2.097. Thereafter, the Si excess is estimated from 30.1 to 8.1 at.% by monitoring the r_N from 7.0 to 13.3%. As a consequence, both

x values and Si excess determined from refractive indices have the same values and evolution trends as those obtained from FTIR spectra.

(c) Estimation error for Si excess

As a logical step, the error estimations have been studied for the Si excess deduced from the two experimental approaches.

- For FTIR approach,

as $x = 0.003(W_{LO} - 1197) + 4/3$, (4.1)

so $\Delta x = 0.003\Delta W_{LO}$,

(4.2)

where the Δx is N/Si ratio error and ΔW_{LO} is about 1 cm^{-1}.

- For ellipsometric approach,

as $x = \frac{4(4.498 - n)}{3(n + 0.798)}$, (4.3)

so $\frac{\Delta x}{x} = (\left|\frac{1}{4.498 - n}\right| + \left|\frac{1}{n + 0.798}\right|) \times \Delta n$, (4.4)

where the Δn is about 0.002.

Since $Si_{ex}(at.\%) = y = \frac{4 - 3x}{4 + 4x} \times 100\%$, (4.5)

we determine the maximum and minimum values of Si excess achieved with an uncertainty Δx (eg. 4.2 and 4.4 depending on the techniques used):

$y_{\max} = \frac{4 - 3(x - \Delta x)}{4 + 4(x - \Delta x)} \times 100\%$, (4.6)

$y_{\min} = \frac{4 - 3(x + \Delta x)}{4 + 4(x + \Delta x)} \times 100\%$, (4.7)

The uncertainty Δy is determined by the absolute difference between y_{max} and y_{min} values. The obtained error values Δy plotted with the Si excess are shown in figure 4.3.

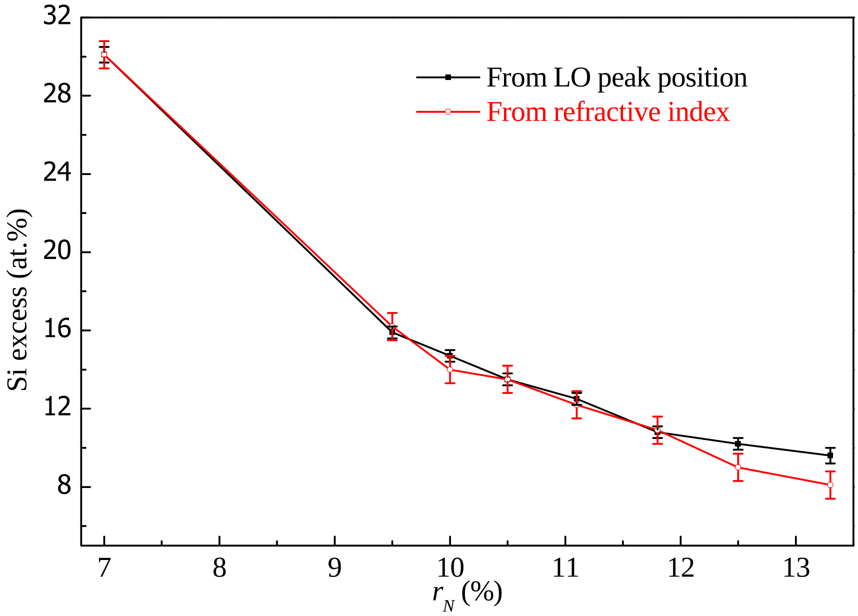

Figure 4.3: Si excess evolution versus r_N *with experimental error bars for classical co-sputtered samples. The Si excess values have been deduced from FTIR and ellipsometric measurements.*

One can see (Fig. 4.3) that the Si excess obtained by both methods follows a comparable decrease with nitrogen rate r_N within the error bars. Indeed used ellipsometry method concerns the density of chemical bonds presented in the matrix. Moreover, the increase of the LO band intensity is a signature of the Si-N density increase and Si content decrease in the volume of SiN_x while the ordering of the films increases. Consequently, one can suppose that both methods are sensitive to a similar volume of Si excess in thin film and lead to a comparable result shown in Table 4.1 from 30.1 to 8.1 at.%.

4.2.4 Optimal Si content

This section aims at obtaining an optimal emission from Nd^{3+} ions in SRSN matrix using a 488 nm non-resonant laser excitation. Both as-grown and 750°C-1min-annealed layers were chosen to study their photoluminescence properties. This allows determining the best deposition conditions for fabricating thin films that will be used for the next optimization study.

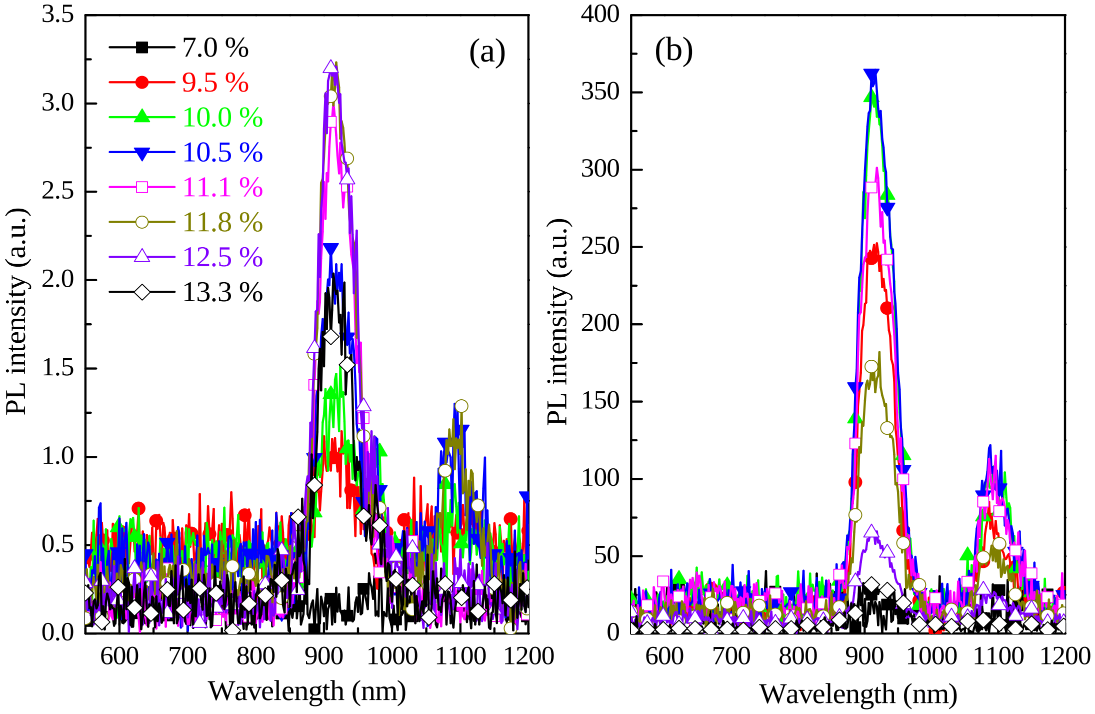

Figure 4.4: PL spectra for different nitrogen rates r_N from 7.0% to 13.3% in (a) as-grown samples and (b) 750ºC-1min-annealed samples. The excitation wavelength (488 nm) is non-resonant with the energy levels of the Nd^{3+} ions.

Figure 4.4 shows the PL spectra from Nd-SRSN films deposited with various r_N before (a) and after annealing at 750°C during 1 minute (b). For the as-deposited samples, Nd^{3+} PL peaks are clearly observed at about 920 and 1100 nm. It denotes that sensitizers transferring energy to Nd^{3+} ions are already present in the as-grown samples. The maximum of PL is obtained for sample deposited with high nitrogen rate (r_N = 12.5%). After annealing at 750ºC during one minute, the intensity of Nd^{3+} PL is enhanced by more than two order magnitudes. One can see it gradually increases as the r_N decreases from 13.3% to 10.5%, before falling down for lower r_N. No emission is recorded from the sample with r_N = 7.0%. This demonstrates the importance of controlling the nitrogen rate to (i) favor the highest sensitizer density, (ii) decrease the Sensitizers-Nd^{3+} ions distance, (iii) monitor the Si excess to avoid a too high disorder of the matrix which will create non-radiative de-excitation paths, and (iv) promote the highest coupling rate between sensitizers and lanthanide ions. One can notice that for both as-grown and annealed layers, no emission in the visible range has been recorded contrarily to the SRSO-doped thin films (Sect 3.2.4 Chap. 3). It could be attributed either to maximum Sensitizers-Nd^{3+} ions coupling, or to other physical mechanism allowing an efficient sensitization of the rare earth ions. After annealing, the maximum Nd^{3+} PL is achieved from the samples with $r_N \approx 10.5\%$ corresponding to an optimal Si excess of 13.5 at.%.

4.3 Effect of Nd content incorporated

After obtaining the optimal Si excess, samples are produced with different Nd contents by monitoring the Nd_2O_3 RF power density (RFP_{Nd2O3}) applied to the cathode. In this section, the RFP_{Nd2O3} is varied between 0 to 0.6 W.cm^{-2}.

4.3.1 Estimation of Nd content

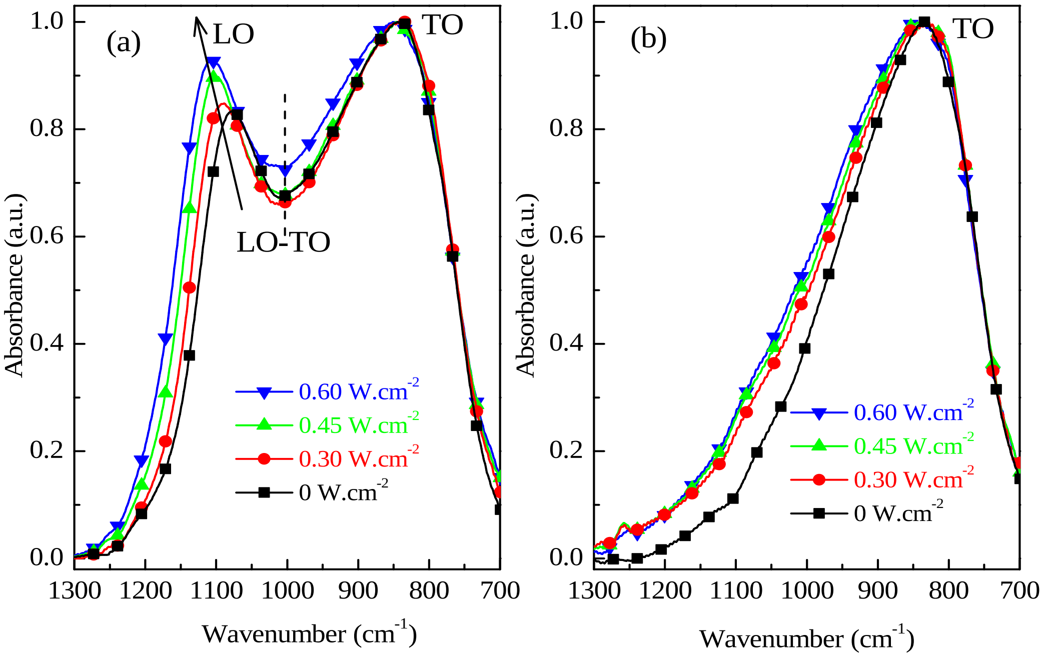

Figure 4.5: FTIR spectra recorded with (a) an incidence angle of 65° and (b) a normal incidence for as-deposited samples fabricated with the indicated RFP_{Nd2O3}. The curves have been normalized with respect to the TO band intensity.

The FTIR spectra corresponding to measurements performed at an angle of 65° and at normal incidences are shown in figure 4.5(a) and (b) after normalization to the TO vibration mode. In figure 4.5(a), LO and TO bands from Si-N bond vibrations are present. As seen, the LO peak gradually shifts to high wavenumber with a concomitant increase of its intensity, with RFP_{Nd2O3}. This is the signature of the Si excess decrease, as demonstrated above. Such evolution can be explained by the increase of species present in the plasma with RFP_{Nd2O3} which will raise the free mean path of the sputtering element and/or species. Consequently, the reaction with nitrogen in the plasma leads to a lower incorporation of Si excess with RFP_{Nd2O3}. The increase of Nd concentration in the host matrix induces a concomitant disorder as evidenced by the evolution of the overlap intensity of LO-TO pair. Moreover, the sputtering of the oxide target of Nd favors the incorporation of oxygen and thus a band from Nd-O-Si vibration located at about 940 cm^{-1} may contribute to the evolution to the FTIR spectra in this region[7]. The presence of oxygen in the films is confirmed with the experiments performed at normal incidence. In figure 4.5(b), the left shoulder located in the region 1050-1100 cm^{-1} corresponding to the TO_{Si-O} vibration band, exhibits a gradual increase with RFP_{Nd2O3}. Thus, FTIR experiments confirm the incorporation of O and Nd atoms which are favored by the increasing RFP_{Nd2O3}.

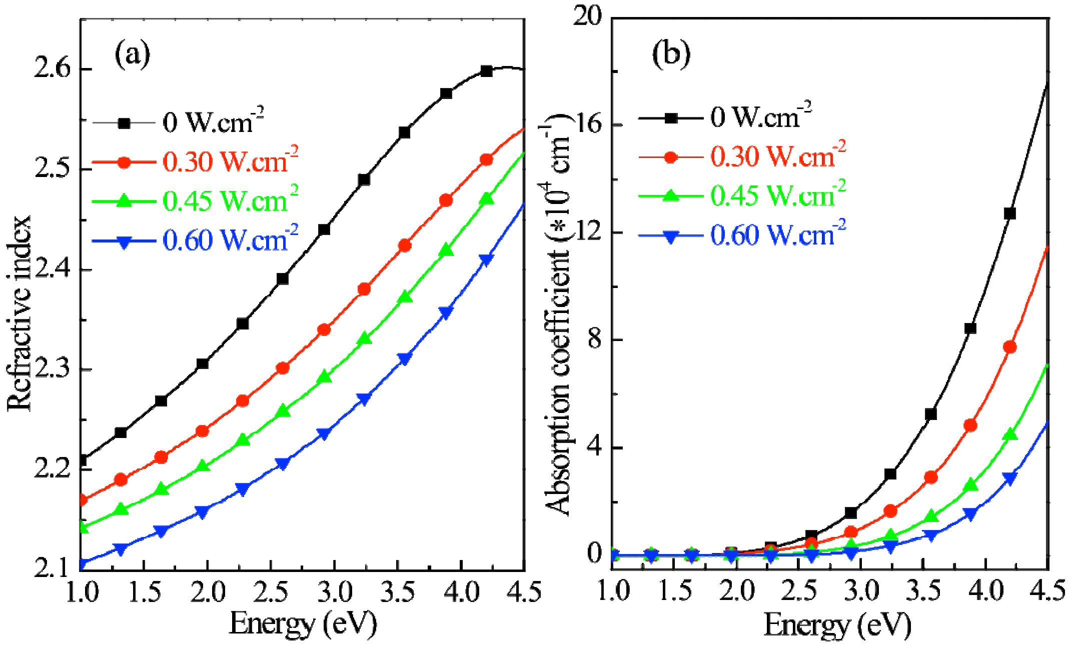

Figure 4.6: Evolutions of (a) refractive index and (b) absorption coefficient for as-deposited samples with the indicated RFP_{Nd2O3}.

Ellipsometric experiments were carried out to study the evolution of layer compositions. The obtained refractive index (n) and absorption coefficient (*k*) are displayed in figure 4.6(a) and (b), respectively. Both n and k values show a gradual decrease with increasing RFP_{Nd2O3}. The former confirms the results achieved by FTIR experiments with a reduction of Si excess and an increase of the oxygen content in the as-grown layers. This is corroborated by the decrease of the absorption coefficient with RFP_{Nd2O3}.

To have an idea of the doped Nd content, RBS measurement was performed on a typical sample. It was found that a large Nd concentration of 5×10^{20} at.cm^{-3} has been incorporated into the layer deposited with RFP_{Nd2O3}=0.45 W.cm^{-2} and r_N=10.5%.

4.3.2 Optimal Nd content

The goal is to find the optimal Nd content, which corresponds to the strongest emission intensity of the Nd^{3+}-doped layers. For this purpose, room temperature PL measurements on as-grown and 750°C-1min-annealed layers have been carried out.

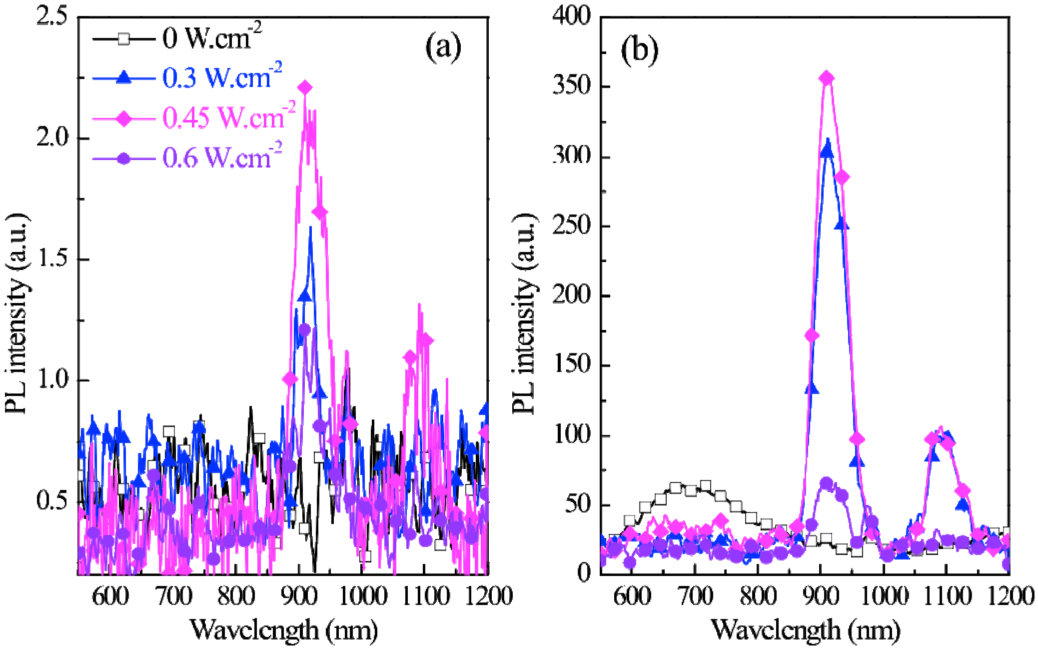

Figure 4.7: PL spectra for (a) as-deposited and (b) 750ºC-1min-annealed samples fabricated with the indicated RFP_{Nd2O3}*. The excitation wavelength (488 nm) is non-resonant with the energy levels of the* Nd^{3+} *ions.*

The PL spectra of samples deposited with various RFP_{Nd2O3} are shown in figure 4.7(a) for as-grown and (b) for 750ºC-1min annealing. As expected, no emission is detected for the as-grown sample fabricated without RF power on the Nd_2O_3 target. After a short annealing time at relatively low temperature, a visible photoluminescence in the 600-800 nm range is recorded. Such an emission has already been observed in our group in SiN_x layer deposited using the same technique and annealed at 900°C during one hour[7]. Taking into account the relatively low temperature applied here, one cannot consequently at this level of the study, define the origin of this emission that can be the result of the presence of amorphous Si-nps, band tails and/or defect states levels[7] [8]. When we incorporate Nd atoms in the nitride layers, an emission peaking at 920 nm and around 1100 nm appears

(Fig. 4.7 (a)). This emission reaches the maximum intensity for the film deposited with RFP_{Nd2O3} = 0.45 W.cm^{-2}, before decreasing for higher RF power density. As seen in the case of the SRSO doped layer (Sect. 3.3.2 Chap.3), this can be attributed to cross relaxation process between Nd^{3+} ions and/or formation of Nd_2O_3 clusters. After annealing (Fig. 4.7 (b)), the trend remains the same with an increase of the Nd emission to reach its maximum for the layer deposited with RFP_{Nd2O3} = 0.45 W.cm^{-2}. Then a decrease attributed to a concentration quenching process is observed. One can notice that for the annealed doped layers, no or really weak (RFP_{Nd2O3} = 0.45 W.cm^{-2}) emission in the visible region is observed. This is the signature of an efficient energy transfer occurring between the visible luminescence centers in the host matrix and the Nd^{3+} ions present in the surrounding.

For further studying the effect of the annealing treatment, the films fabricated with RFP_{Nd2O3} = 0.45 W.cm^{-2} and a nitrogen rate r_N of 10.5% will be used.

4.4 Effect of annealing conditions

The influence of the annealing process on the optical properties of the optimized Nd-doped Si-based layers has been carried out by means of Rapid Thermal Annealing (RTA) or Classical Annealing (CA) approaches.

4.4.1 Annealing temperature for RTA approach

(a) Fourier transform infrared spectroscopy

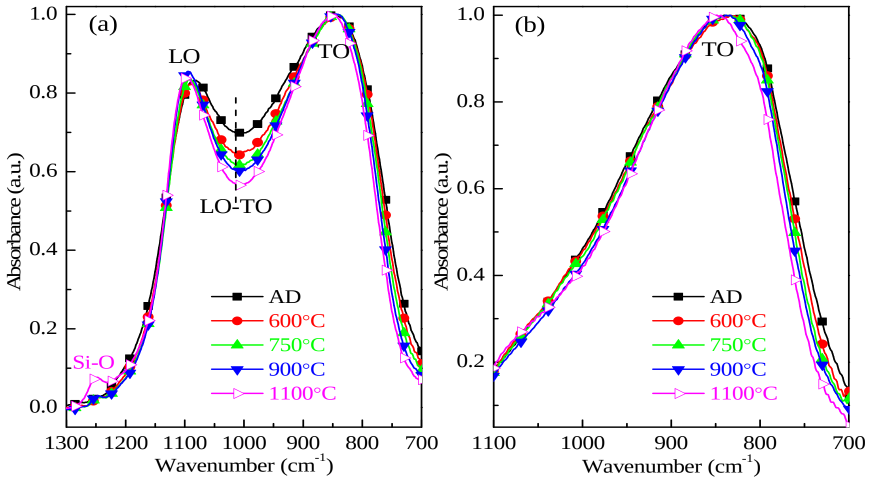

Figure 4.8: FTIR spectra recorded with (a) an incidence angle of 65° and (b) a normal incidence for the Nd-SRSN layers as-deposited (AD) and 1min-annealed at the indicated temperatures (T_A). The curves have been normalized with respect to the TO band intensity.

Figure 4.8 shows the FTIR spectra of as-deposited and annealed Nd-SRSN samples prepared with r_N, RFP_{Nd2O3} and RFP_{Si} of 10.5%, 0.45 and 4.5 W.cm^{-2}, respectively. The spectra are normalized to the TO mode. The annealing treatment consists in heating the samples at 600, 750, 900 or 1100°C (T_A) during one minute using the RTA procedure detailed in Sect.2.1.2 of Chap. 2. The overlap intensity of TO-LO pair displays a decreasing trend with T_A. As already mentioned, such pair intensity is related to the disorder of the host matrix. Consequently, this evolution with T_A indicates a reorganization of the matrix. Note the appearance of a vibration mode peaking at about 1250 cm^{-1} for T_A=1100ºC. This peak attributed to the asymmetric stretching vibration of Si-O bond (LO_3) (Sect. 2.2.1 Charp.2) is related to the Si-O-Si bond at 180°. It could be the result of Si-np formation in the host matrix and/or the oxidation of the surface of the film. Figure 4.8(b) displays the spectra recorded in the normal incidence allowing to obtain the TO vibration mode. The maximum of this band is shifting with T_A to high wavenumbers. All these observations suggest a rearrangement of the Si nitride network towards that of the stoichiometric structure by increasing T_A.

(b) Raman spectra

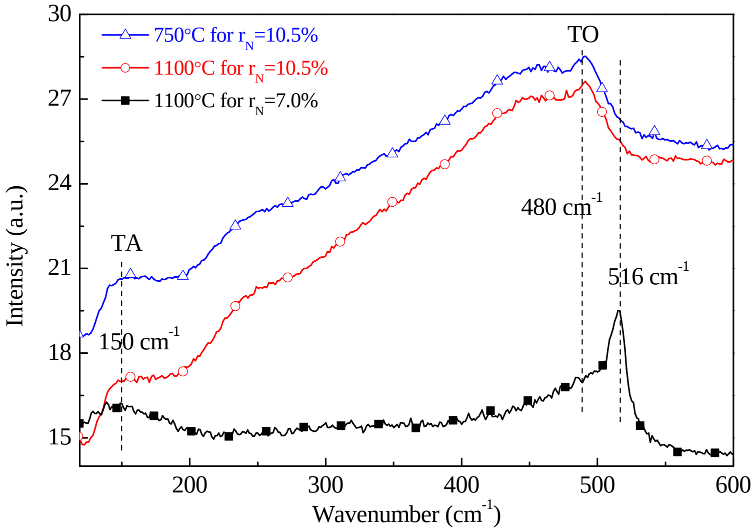

Figure 4.9: Raman spectra of the samples deposited with the indicative nitrogen rate r_N and 1min-annealed at the indicated T_A. The samples were prepared with RFP_{Nd2O3} and RFP_{Si} of 0.45 and 4.5 W.cm^{-2}, respectively.

Figure 4.9 shows the three Raman spectra corresponding to the optimized layer (r_N =10.5%) 1min-annealed at T_A= 750 and 1100ºC, and to the layer containing the highest Si excess (r_N =7.0%) after an annealing at T_A= 1100ºC during 1minute. For the typical layer (r_N =10.5%), both Raman curves have two broad bands centered at about 150 and 480 cm^{-1} which correspond respectively to the transverse acoustic (TA) and transverse optical (TO) phonon frenquencies of amorphous silicon nanoparticules. When the nitrogen rate decreases, i.e. it favors the incorporation of the Si excess, one can see the presence of a peak at 516 cm^{-1} after an annealing at high temperature. This peak is attributed to crystalline Si-nps meaning that threshold limits of Si excess and temperature are required to form Si nanocrystals in such a nitride matrix. Comparing this peak with the one at 521 cm^{-1} for bulk Si, one can deduce the Si-nps size. On the basis of bond polarizability model[9], the frequency red-shift can be presented as a function of the Si-nps size using the analytical expression[7]:

$$\Delta\omega = \beta(\alpha/\mathrm{d})^{\gamma} \tag{4.8}$$

where α is the Si lattice parameter (0.543 nm), d is the crystalline Si-nps diameter, β (47.41 cm^{-1}) and γ (1.44) are both the model parameters. Taking into account a frequency redshift (Δω) of 5 cm^{-1}, the size of the Si nanocrystals is about 2.6 nm. According to the fact that more Si excess favors a growing of large Si-nps, the high r_N (10.5%) films with less Si excess should have Si-nps smaller than 2.6 nm (r_N=7%). This could explain that only amorphous Raman signal (TA and TO peaks) is observed in layer with r_N=10.5%.

(c) Photoluminescence properties

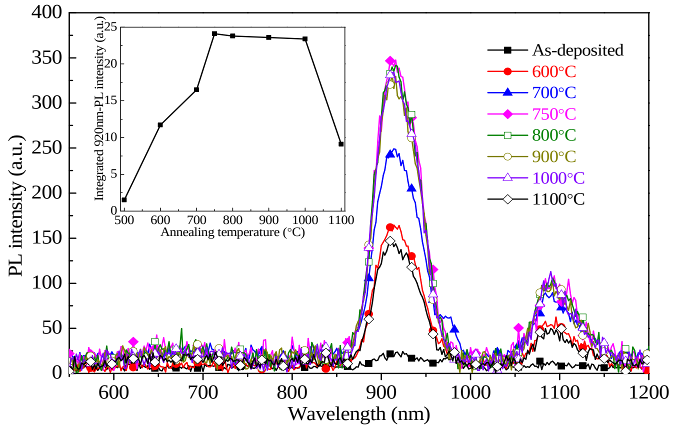

Figure 4.10: PL spectra for as-deposited and 1min-annealed samples (at indicated T_A). The sample was prepared with r_N, RFP_{Nd2O3} and RFP_{Si} of 10.5%, 0.45 and 4.5 $W.cm^{-2}$, respectively. The inset shows the integrated PL intensity for 920 nm peak versus T_A. The excitation wavelength (488 nm) is non-resonant with the energy levels of the Nd^{3+} ions.

The PL spectra are displayed in figure 4.10 for as-deposited and annealed at various T_A films during one minute. Whatever the T_A applied, there is no emission in the visible range 600-800 nm. This differs from the Nd-SRSO films (Sec. 3.5 in Chap. 3) for which remarkable emission bands have been recorded due to the presence of radiative defects or Si-nps., Taking into account the RAMAN results, these observations can be the results of (i) a nitride matrix not favorable for light emitting Si-nps or radiative defects and/or (ii) an efficient energy transfer from sensitizers to Nd^{3+} ions.

In infrared range 850-1200 nm, two peaks appear locating at about 920 and 1100 nm. They are attributed to the radiative recombination occurring in Nd^{3+} ions from the $^4F_{3/2}$ to $^4I_{9/2}$ and to $^4I_{11/2}$ levels, respectively. When increasing T_A, the PL intensity (see inset) is significantly improved before collapsing at 1100ºC. The samples show optimal PL in a wide range of annealing temperatures from 750 to 1000ºC. Similarly to Nd-SRSO samples (Sect. 3.4.1 Chap. 3), the optimal T_A for achieving the brightest emission corresponds to a moderate temperature. Indeed low T_A does not allow to recover the non-radiative defects present in samples while high T_A could lead to form rare earth clusters and/or to lower the density of efficient sensitizers[10]. But even after a 1000ºC annealing treatment, the nitride samples still can hold a high PL, suggesting that such matrix is less favorable for the formation of Nd-based clusters. If we assume that these Nd-based clusters are mainly composed of Nd oxide[11], it is reasonable to conclude that these clusters grow easier in the oxide matrix, even if one have the presence of oxygen in a low content in our samples. Thus the nitride host matrix is favorable to the incorporation of a higher Nd concentration (10 times more than oxide case) and, with a presence of Si excess, to achieve a high PL intensity even after annealing at high temperatures as high as 1000°C. This result is in agreement with those on similar system Er-SRSN film, for which Er ions are kept optically active even at high temperature[12][13]. The authors explain that such a result is consistent with the lower diffusivity of metals in nitrides with respect to that in silica[14].

It is interesting to note that the Nd^{3+} peak intensity for layer having same thicknesses has three times higher PL in Nd-SRSN samples compared to the Nd-SRSO films. This is explained by a higher Nd content incorporated with less probability to form clusters in nitride matrix and a short Nd-Sensitizer distance.

4.4.2 Annealing temperature for CA approach

(a) Fourier transform infrared spectroscopy

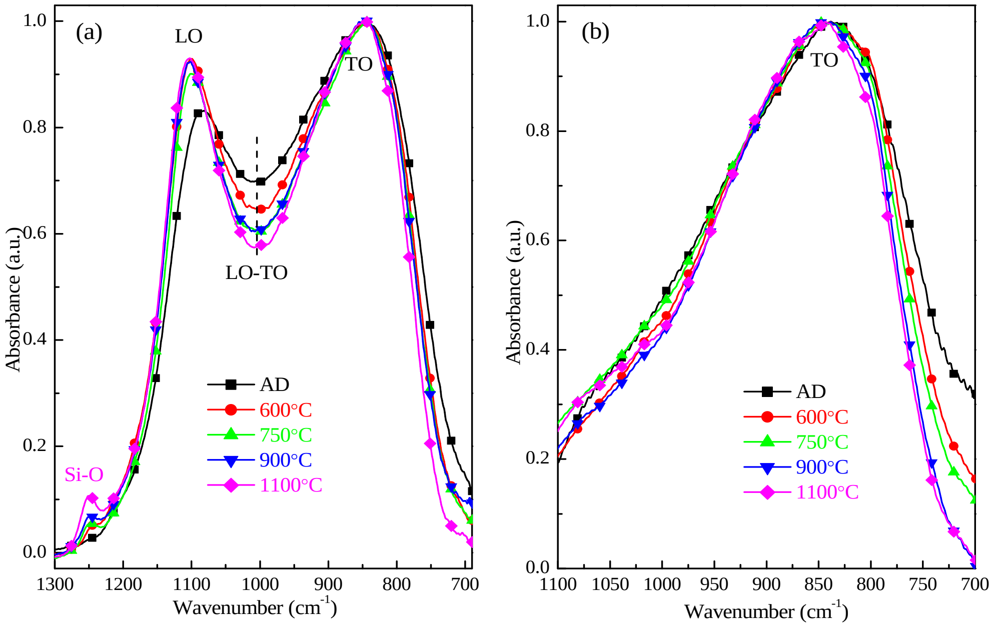

Figure 4.11: FTIR spectra recorded with (a) an incidence angle of 65° and (b) a normal incidence for the Nd-SRSN layers as-deposited (AD) and 1hour-annealed at the indicated temperatures. The sample was prepared with r_N, RFP_{Nd2O3} and RFP_{Si} of 10.5%, 0.45 and 4.5 W.cm^{-2}, respectively. The curves have been normalized with respect to the TO band intensity.

Figure 4.11 shows the effect of the classical annealing treatment (600-1100°C during 1 hour) on the microstructure of the layers using FTIR experiment in (a) an incidence angle of 65° and (b) a normal incidence. All the spectra are normalized to the TO band intensity. In the case of 65° incidence, the LO peak intensity increases significantly after annealing and shifts towards higher wavenumbers. The position of TO peak follows a similar trend. The LO-TO coupling band gradually attenuates with increasing T_A, suggesting a host matrix becoming more ordered. The Si-O peak at about 1250 cm^{-1} appears with annealing and increases with T_A evidencing either an oxidation of the surface of the films or presence of Si-nps surrounded by O atoms provided by the sputtering of the Nd oxide target. In the case of normal incidence measurements, the TO peak is also observed to blue shift with T_A. This result indicates a structural rearrangement of the matrices and/or a phase separation in the Nd-SRSN materials with annealing.

(b) Raman spectra

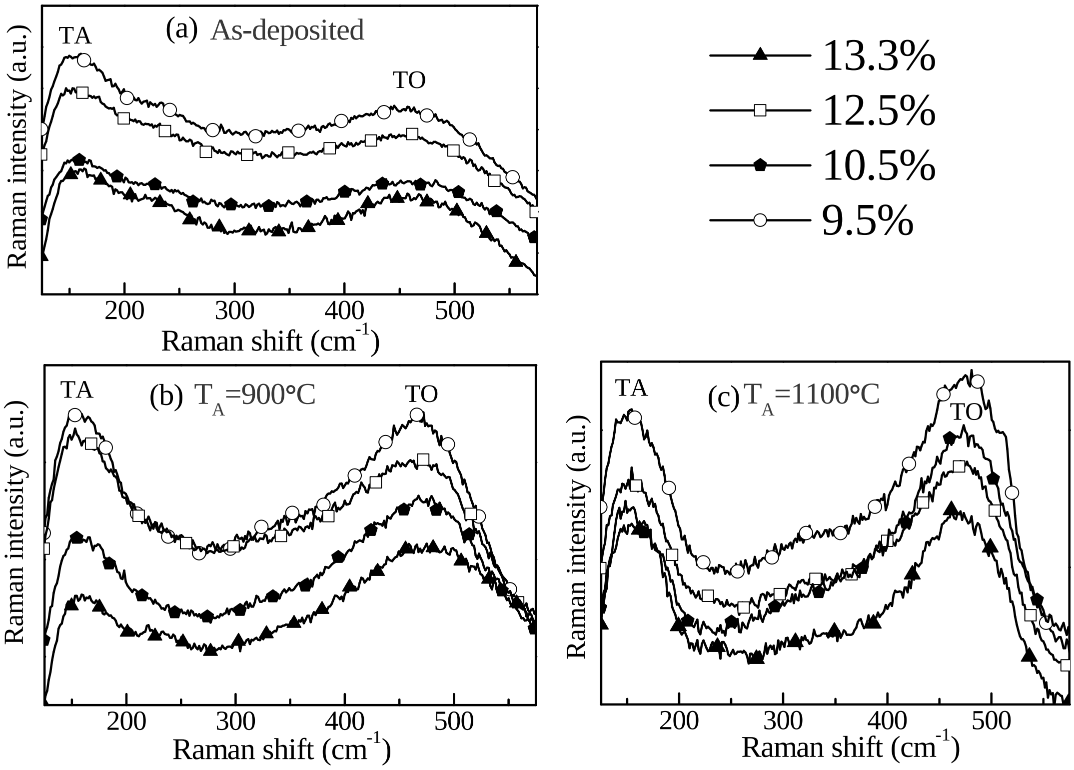

Figure 4.12: Raman spectra of the as-deposited and 1hour-annealed Nd-SRSN films at 900 and 1100°C. The layers have been deposited on fused silica with RFP_{Nd2O3}*= 0.45 W.cm*$^{-2}$*,* RFP_{Si}*=4.5 W.cm*$^{-2}$*, and indicated* r_N*.*

Figure 4.12 has three pictures corresponding to as-deposited, T_A= 900 and 1100ºC samples. These samples contain the typical Nd-SRSN layers (r_N=10.5%), as well as with other r_N for the comparison of their Raman spectra. In figure 4.12(a) for the as-deposited samples, the Raman curves show two broad vibration bands located at 150 and 480 cm^{-1}. These are respectively attributed to the transverse acoustic (TA) and the transverse optical (TO) phonon for amorphous Si-nps suggesting the formation of Si-nps during the deposition process. After the layers were annealed at 900ºC, both TA and TO bands are changed to be clearly narrower and more pronounced. This evolution is explained by an increase in the Si-nps concentration. Upon annealing at 1100ºC, these two bands have the highest intensity, whereas, no additional peak is noticed such as at about 521 cm^{-1}. One can assume that no crystalline Si-nps have been formed during such a high annealing process. This observation is in agreement with the one achieved in our team on undoped SRSN layers[8]. Debieu et al. revealed that the samples containing a low Si excess (refractive index lower than 2.5) have only amorphous Si-nps even after an annealing treatment at 1100ºC. This can be explained by the work of Mulloni et al.[15] who have found that the nitrogen has an ability to suppress the diffusion of silicon atoms during annealing. This may lead to grow only small Si-nps.

(c) Photoluminescence properties

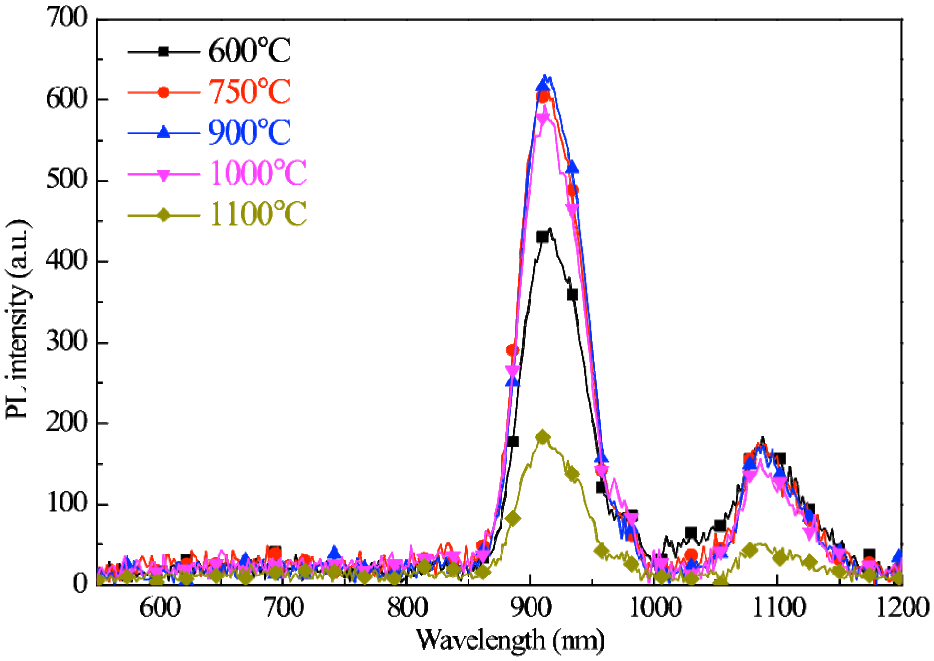

Figure 4.13: PL spectra for samples under 1hour-annealing at the indicated temperatures. The sample was deposited with RFP_{Nd2O3}*= 0.45 W.cm*$^{-2}$*,* RFP_{Si}*=4.5 W.cm*$^{-2}$*, and* r_N*=10.5%. The excitation wavelength (488 nm) is non-resonant with the energy levels of the* Nd^{3+} *ions.*

Figure 4.13 shows the PL spectra for samples annealed at different temperatures. The results are similar to those obtained after an RTA treatment. In 600-800 nm visible range, no emission band is seen from all the samples even after an annealing at 1100ºC, while in 850-1200 nm infrared range, remarkable Nd^{3+} emission peaks are detected. The peaks intensities present significant increase when T_A rises from 600 to 750ºC. The maximum PL is achieved between 750 and 1000ºC, before decreasing for higher T_A. However, the 1100ºC annealing does not lead to a complete suppression of the Nd^{3+} emission. Again, one can mention that the temperature range corresponding to the optimal Nd^{3+} PL is broader than in the case of the oxide host matrix. Such a result is the same than the RTA effects already described above. This broad optimal temperature domain is ascribed to a less diffusivity of RE ions in nitride layer than in oxide one.

4.4.3 Annealing duration

The previous two sections have concerned the effects of RTA and CA approaches on the structural and PL properties of the films. The influence of annealing temperature has been investigated with a duration fixed at 1 min for RTA and 1 hour for CA approach. In this section, we detail the result achieved after a process in RTA furnace during 5-60 min at two specific temperatures, 750 and 1100ºC.

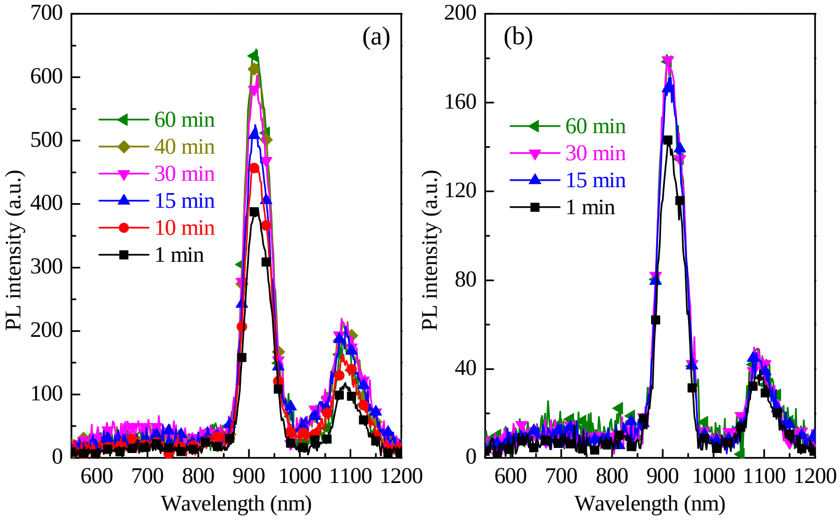

Figure 4.14: Evolution of PL spectra versus annealing duration from 1 to 60 min for samples annealed at 750ºC (a) and 1100ºC (b). The sample was deposited with RFP_{Nd2O3}*=0.45 W.cm*$^{-2}$*,* RFP_{Si}*=4.5 W.cm*$^{-2}$*, and* r_N*=10.5%. The excitation wavelength (488 nm) is non-resonant with the energy levels of the* Nd^{3+} *ions.*

Figure 4.14 shows the PL spectra of the Nd-SRSN samples, recorded after different annealing durations. In Fig. 4.14(a) for T_A = 750ºC, the emission intensity is improved with t_A and reaches the maximum after 60 min of annealing. Near twofold increase is observed for 1 hour annealed sample in comparison to the 1 min one. This increase is connected to the reorganization of the matrix and thus a decrease of the non-radiative defects with extending t_A value. In Fig. 4.14(b) for T_A = 1100ºC, the enhancement of PL intensity with t_A is also noticed. A saturation of PL seems to occur and appears after an annealing duration of 30 min. This can be attributed to the high T_A that provides enough energy for the layer reorganization during shorter time. Anyway, this high temperature is nevertheless not adapted for the achievement of intense emission since the maximum PL obtained is four times lower than after a process at 750°C.

4.4.4 Forming gas annealing

This section aims at investigating the effect of annealing the film in the forming gas (FG: 95% Ar and 5% H_2). The Nd-SRSN samples studied have been fabricated with RFP_{Nd2O3}= 0.45 W.cm^{-2}, RFP_{Si}=4.5 W.cm^{-2}, and r_N=10.5%. Two approaches have been carried out. On one hand, single step annealing is performed using FG gas at the optimized T_A = 750ºC. On the other hand, the two-steps approach includes firstly an annealing at higher temperatures (750 and 1100ºC) under N_2 gas, and then annealing at 500ºC for 5 hour under FG ambient. These annealing processes were all performed in RTA furnace.

(a) Single step annealing

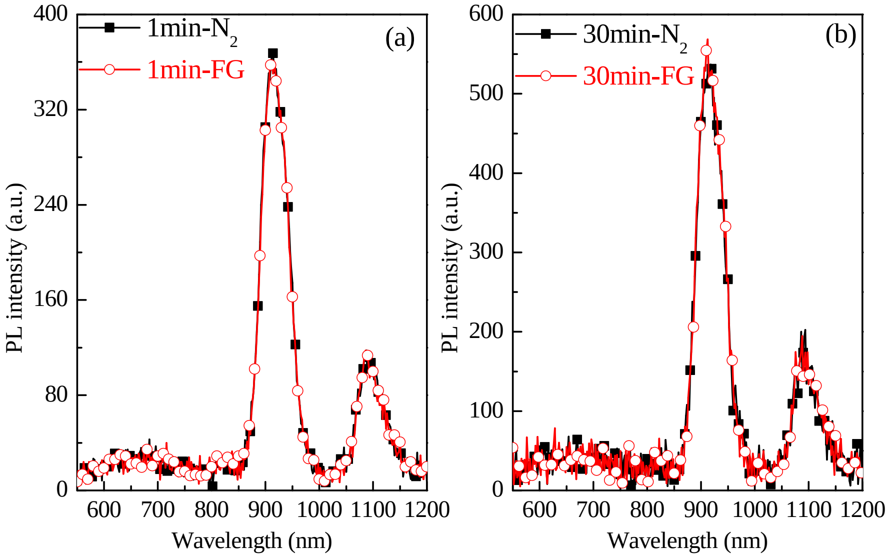

Figure 4.15: PL spectra of samples annealed at 750ºC for (a) 1 min and (b) 30 min duration under N_2 gas (black solid) and FG ambient (red hollow), respectively. The 488 nm excitation wavelength is non-resonant with the energy levels of the Nd^{3+} ions.

Figure 4.15 shows the PL spectra of samples annealed under N_2 gas and FG ambient, respectively. As seen, the Nd^{3+} PL intensity remarkably increases with annealing duration from 1 to 30 minutes under either N_2 gas or FG ambient. Such improvement is due to the modification of host matrix during annealing. This modification occurs independently on the used gas. Moreover, when comparing two different gases, no difference of PL spectra is noticed between N_2 and FG gas annealing for either 1 or 30 minutes duration. This differs from the case of Nd-SRSO layers (Sec.3.4.4 in Chap.3) for which a higher PL intensity has been observed after an annealing under FG gas. Such a result means that the amount of non-radiative channels which can be passivated is low in the SRSN matrix.

(b) Two steps annealing

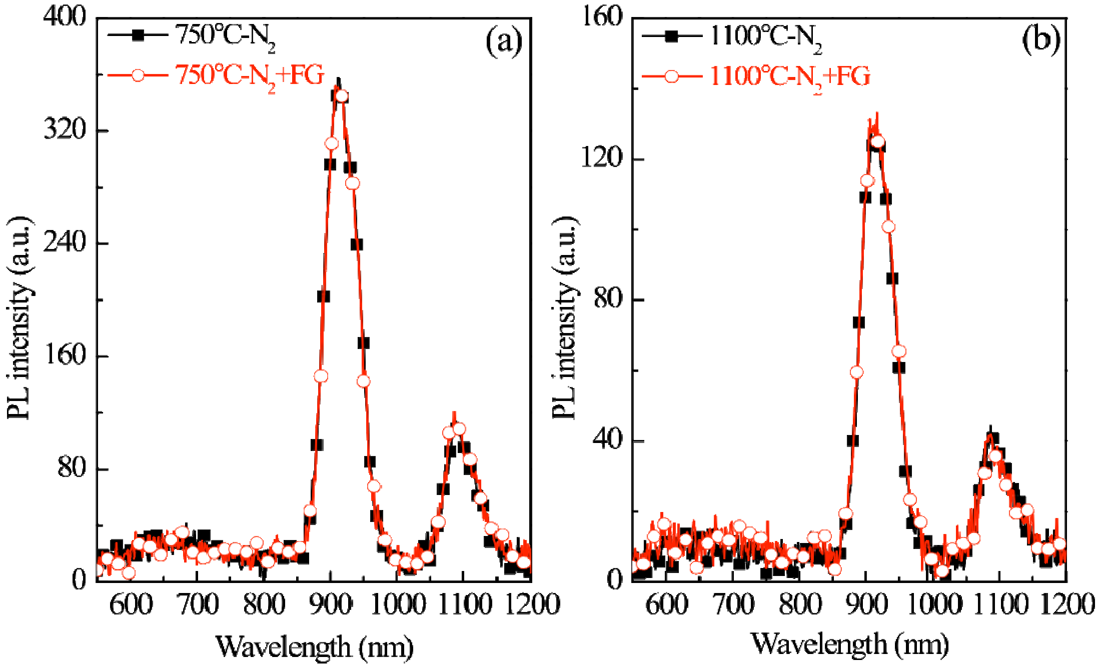

Figure 4.16: PL spectra of samples annealed at the indicative T_A for 1 min duration. The black curves with solid symbol correspond to annealing under N_2 gas, while the red curves with hollow symbol concern two steps annealing. The FG in this figure represents a 500°C-5hour-annealing under forming gas ambient. The 488 nm excitation wavelength is non-resonant with the energy levels of the Nd^{3+} ions.

Figure 4.16 presents the comparison of PL spectra for samples annealed at 750°C- or 1100°C during 1minute followed or not by a 500°C-5hour annealing under FG ambient. In the first step annealing at either 750 or 1100°C under N_2 gas, significant Nd^{3+} PL has been observed using non-resonant excitation wavelength for the Nd^{3+} ions. As mentioned above, this observation denotes the existence of sensitizers towards RE ions. Furthermore, the 1100°C-annealed sample has lower emission intensity than the case at 750°C. It is probably explained by the formation of Nd_2O_3 clusters and/or by the lower density of efficient sensitizers after the high temperature annealing. These imply different microstructures presented in these two

T_A-annealed films. To further modify the microstructure of such already annealed layers, the second step annealing has been carried out at 500ºC for 5 hour under FG ambient. But we did not notice any change of the FTIR spectra (data not shown) comparing to the one after first step annealing. Moreover, no difference is seen for the Nd^{3+} PL in contrast to the case of first step annealing at either 750 or 1100ºC. This again differs from the case of Nd-SRSO layers (Sec.3.4.4 in Chap.3). It comes to the conclusion that rather few non-radiative channels that can be passivated by the H are residual in the first step annealed layers.

4.5 Energy transfer mechanism

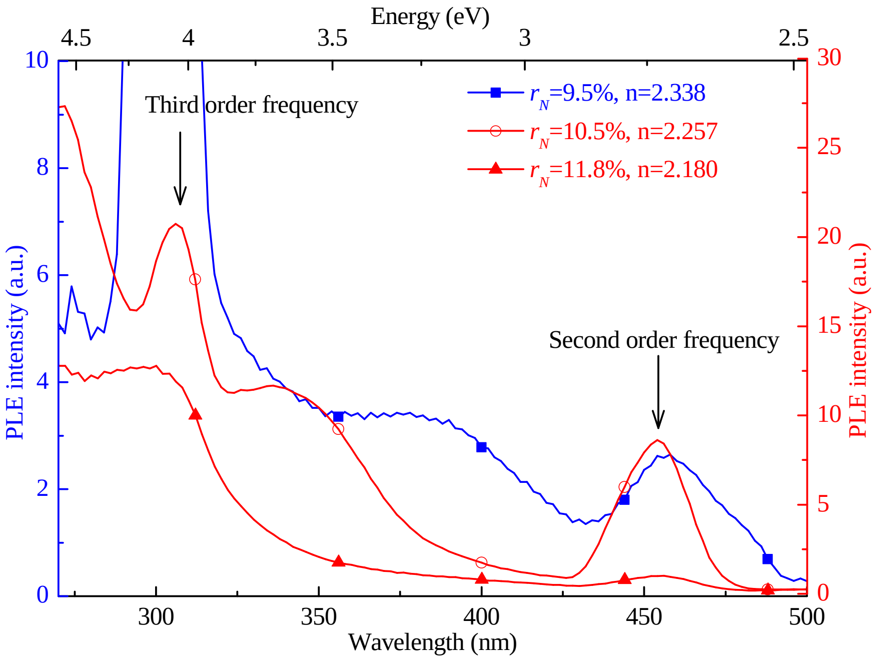

Figure 4.17: PLE spectra detected at 920 nm for three samples (r_N=9.5%, 10.5%, and 11.8%) annealed at 750ºC for 1 min duration. The curves correspond to different perpendicular scales classified by their color.

To study the energy transfer mechanism, PL excitation (PLE) measurements were carried out on three Nd-SRSN samples deposited at different r_N and annealed at 750ºC for 1 minute duration. As mentioned above, these samples have various refractive indices (n) indicating different Si excess incorporated. In figure 4.17, the obtained PLE spectra detected at 920 nm are shown. The spectra have been corrected by the power variation of the used excitation source. Each curve has two peaks at about 307 and 460 nm which are respectively ascribed to third and second order of the detected wavelength. For all the spectra, the PLE intensities present an increase with excitation energy with a slope increase characteristic of band-tail to band-tail absorption mechanism in amorphous silicon oxynitride matrix[16]. Since PLE spectra are recorded at 920 nm, they reflect also the transfer of excitation to Nd^{3+} ions. The positions of the PLE intensity maxima are shifting to high energies with increasing r_N. Assuming that there is no modification of rare earth ions states, this behavior may be attributed to band gap enlargement of Silicon Nitride matrix with increasing of r_N and consequently is a confirmation of the decrease of Si excess incorporated in the film.

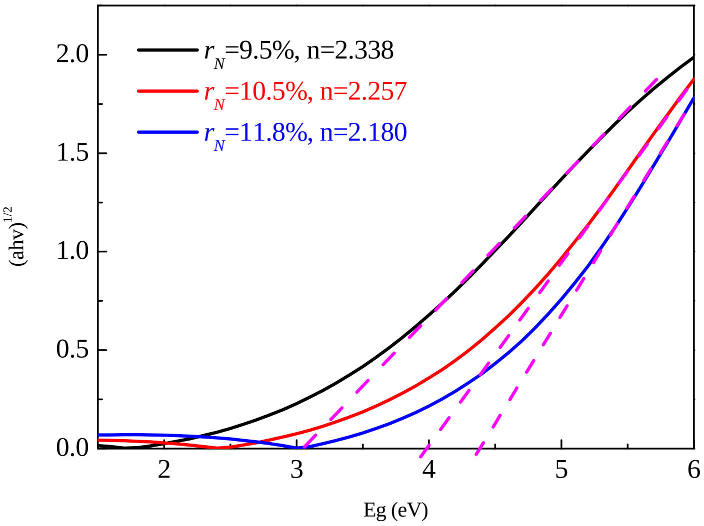

Figure 4.18: Estimation of optical band gap for three samples (r_N=9.5%, 10.5%, and 11.8%) annealed at 750ºC for 1 min duration.

In order to check this hypothesis, Tauc plot were performed on absorption coefficient evolution with energy (shown in Fig 4.18) of same SiN_x samples (r_N=9.5%, 10.5%, and 11.8% annealed at 750ºC for 1 min duration). A Tauc gap (optical gap) was found to increase from 3.05 to 4.40 eV with r_N varying from 9.5% to 11.8% in the same manner as reported by Biggemann et al.[17]. This confirms the fact that there is a proportional dependency between the SiN_x matrix band gap and the nitrogen rate r_N. Consequently the Band gap enlarges inversely to the excess of Si incorporated in the SiN_x host matrix. These results demonstrate the tunability of the absorption windows of SiN_x matrix and thus, the excitation windows for the indirect excitation of the Nd^{3+} ions by a fine engineering of the Si excess.

As a result, the PLE experiments have demonstrated that the band tails states can act as efficientive sensitizers towards the Nd^{3+} ions in the high energy range

(> 2.75 eV). While in lower energy range (< 2.75 eV), the low PLE intensity does not allow to identify the sensitizers involved in the 488 nm (2.54 eV) excitation used in PL measurements. But the difference in PLE intensity between high and low energy range suggest that band tails is a more effective sensitizer of Nd^{3+} ions than the one involved in the sensitizing at 488 nm (2.54 eV).

4.6 Conclusion

We have presented a detailed experimental study of Nd-SRSN films deposited by reactive co-sputtering approach using Si and Nd_2O_3 targets under N_2-rich Ar plasma. The Si excess has been tuned by changing the N_2 rate r_N, while Nd content via monitoring the RFP_{Nd2O3}. The former was calculated by both FTIR and ellipsometric experiments, while the latter from RBS measurements. We have found that the optimized film can be prepared with r_N=10.5% and RFP_{Nd2O3}=0.45 W.cm^{-2}, which has a composition of about 13.5 at.% Si excess and 5.0×10^{20} Nd.cm^{-3}. Then this optimized layer was submitted to an annealing process such as RTA and CA approaches. The former approach allows the formation of amorphous Si-nps for the layers containing a Si excess less than 16.1 at.% even after an annealing treatment at 1100ºC. For the higher Si excess (30.1 at.%), crystalline Si-nps of 2.6 nm diameter are present after an annealing at 1100ºC. The Nd^{3+} PL using 488 nm non-resonant excitation was highly improved after RTA annealing and displayed the maximized intensity in a broad temperature range from 750-1000ºC. This can be explained by a low diffusivity of metal ions in nitride matrix contrarily to the oxide one. In the case of CA approach, comparable results have been obtained about the amorphous Si-nps and Nd^{3+} PL evolution versus T_A. We have found that the CA approach favors higher Nd^{3+} PL intensity than the RTA case, which agrees with the effect of annealing duration. It was shown at either T_A= 750 or 1100ºC, the Nd^{3+} PL increases with t_A similarly to the oxide layers. However, contrary to Nd-SRSO, we did not observe any enhancement of Nd^{3+} emission under FG annealing. This may be due to the lower amount of non-radiative channels that can be passivated by FG in the SRSN matrix. The PLE investigation have proved that at high excitation energy (> 2.75 eV) a band tails sensitizers play a major role while at lower excitation energy nature of sensitizer has not been identified. Moreover, they showed that the band tails states of SRSN host matrix can sensitize the Nd^{3+} ions in a more efficient manner than other sensitizer involve in the excitation at lower energy 488 nm (2.54 eV).

Bibliography

---

[1] L. Huang, K. W. Hipps, J. T. Dickinson, U. Mazur, X. D. Wang, Thin Solid Films **299** (1997) 104

[2] K. M. Mikhail Baklanov and M. Green, Dielectric Films for Advanced Microelectronics (Wiley Series in Materials for Electronic & Optoelectronic Applications), 1st ed. New York: Wiley, Apr. **6** (2007)

[3] S. Yerci, R. Li, S. O. Kucheyev, T. van Buuren, S. N. Basu, N. Soumendra, L. D. Negro, IEEE J. Sel. Topics Quantum Electron. **16** (2010) 114

[4] S. Hasegawa, L. He, Y. Amano, T. Inokuma, Phys. Rev. B **48** (1993) 5315

[5] M. Molinari, H. Rinnert, M. Vergnat, J. Appl. Phys. **101** (2007) 123532

[6] R. Vernhes, O. Zabeida, J. E. Klemberg-Sapieha, and L. Martinu, J. Appl. Phys. **100** (2006) 063308

[7] O. Debieu, R. P. Nalini, J. Cardin, X. Portier, J. Perrière, F. Gourbilleau, Nanoscale Res. Lett. **8** (2013) 31

[8] Y. Liu, Y. Zhou, W. Shi, L. Zhao, B. Sun, and T. Ye, Mater. Lett. **58** (2004) 2397

[9] V. Paillard, P. Puech, M. A. Laguna, R. Carles, B. Kohn, F. Huisken, J. Appl. Phys. **86** (1999) 1921

[10] O. Savchyn, F. R. Ruhge, P. G. Kik, R. M. Todi, K. R. Coffey, H. Nukala, H. Heinrich, Phys. Rev. B **76** (2007)195419

[11] A. Podhorodecki, G. Zatryb, J. Misiewicz, J. Wojcik, P. R. J. Wilson, P Mascher, Nanotechnology **23** (2012) 475707

[12] J. S. Chang, K. Suh, M. S. Yang, and J. H. Shin, Silicon Photonics II: Components and Integration, Lockwood，P. Lorenzo (Eds.) XVI, **95** (2011)

[13] W. C. Ding, Y. Liu, Y. Zhang, J. C. Guo, Y. H. Zuo, B. W. Cheng, J. Z. Yu, Q. M. Wang, Chin. Phys. *B* **18** (2009) 3044

[14] G. Raghavan, C. Chiang, P. B. Anders, S. M. Tzeng, R.ldo Villasol, G. Bai, M. Bohr, D. B. Fraser, Thin Solid Films **262** (1995) 168

[15] V. Mulloni, P. Bellutti, L. Vanzetti, Surf. Sci. **585** (2005)137

[16] Y. T. An, C. Labbé, J. Cardin, M. Morales, F. Gourbilleau, Adv. Opt. Mater. DOI: 10. 1002/ adom. 201300186

[17] D. Biggemann and L. R Tessle, Mater. Sci. Eng. B **105** (2003) 188

Chapter 5: Devices based on Nd-SRSO and Nd-SRSN materials

5.1 Introduction

Optical waveguides are fundamental components of integrated optical circuits because they are the basic element of various devices such as light modulator, laser, and optical amplifier. A natural choice is to look for transparent dielectrics already used in photonics, such as Si, Br, Ge, Al doped in SiO_2. In case of device with low gain such as Erbium Doped Fiber Amplifier (EDFA)[1] long lengths of device (fiber) are necessary for operation due to small gain. In case of integrated device, it is necessary to work with stronger light matter interaction in order to shorten the device length. For this reason, semiconductor based waveguide device with optical gain are studied since many years. The choices of waveguide core and cladding material determine the gain, the band and bandwidth of the signal, the integration density and the minimum intrinsic losses. Furthermore, due to their CMOS technology compatibility, silicon semiconductor based devices are of particular interest for their possible integration in microelectronics. Moreover, using Si-rich Si-based materials allows (i) to tune the refractive index of the material by the variation of Si excess and (ii) to reach propagation loss as low as 0.4 dB.cm^{-1} at 1523 nm[2]. Hence, the SRSO or SRSN layers can be used to form the core region of a planar waveguides.

The Er-doped waveguide has aroused a huge concern in research community due to the Er^{3+} emission at about 1.54 μm corresponding to the minimum of absorption of standard silica optical fibers[3]. In more compact system, in order to shorten the operating length of the amplifier, erbium-doped waveguide amplifier (EDWA) with higher gain has to be found[4]. One possible solution is to use Er^{3+} doped SRSO or SRSN. In this system, several advantages have been achieved. First, the Si-nps have a continuous broad absorption band[5] that allows the use of low-cost LEDs. This obviates the need of a laser at a specific wavelength that matches the narrow absorption band of rare earth ions. Second, the effective excitation cross section of Si-nps-sensitized Er^{3+} ions is about four orders of magnitudes higher than that of Er^{3+} doped in silica[6]. Finally, the Si-nps sensitization enhances the excitability of Er^{3+}

ions favoring an achievement of net gain at 1.54 µm[7] [8]. However up to now, there are only few papers demonstrating the net gain of Er^{3+} ions[9] [10] [11]. This is explained by the nature of the three-level electronic 4f structure for the Er^{3+} ions leading to a population inversion threshold power and to the possible re-absorption of 1.54 µm photon by the neighboring Er^{3+} ions. In contrast, the Nd^{3+} ions emitting in four-level configuration (1.06 µm) do not have a population inversion threshold pump power and there is no re-absorption of the emitted light at 1.06 µm. Moreover, the up-conversion is negligible with Nd^{3+} ions[12] emitting at 1.06 µm compared to Er^{3+} ions[13] emitting at 1.54 µm. Consequently, a net gain should be achievable with Nd^{3+} ions in an easier manner than with Er^{3+} ions.

In this study, we are concerning the Nd-doped in SRSO and SRSN matrices. With the best composition and microstructure obtained by the optimized process in Chap. 3 and Chap. 4, the films are used to fabricate the waveguides. Our goal is to study the possibility to achieve a Si-based laser at 1.06 due to emission from Nd^{3+} ions. In order to realize net gain essential for laser, optical losses have to be minimized and the Nd^{3+} emission maximized. Thus, the work is divided in the investigations on optical losses, guided fluorescence, and pump-probe measurements performed on the waveguide devices. These works were carried out in the framework of the ANR (DAPHNES n°:08-NANO-005) project by our partners P. Pirasteh and J. Charrier [14] [15] from the FOTON laboratory in Lannion.

5.2 Device fabrication

As mentioned in Chap.3, the Nd-SRSO film was synthesized by classical co-sputtering under pure argon plasma using SiO_2, Si, and Nd_2O_3 cathodes. The RF power densities applied are 8.88, 1.48 and 0.30 $W.cm^{-2}$, respectively. In the case of Nd-SRSN film developed in the Chapt.4, the reactive co-sputtering of Si and Nd_2O_3 cathodes has been used. The RF applied power densities were fixed to 4.5 and 0.45 $W.cm^{-2}$, respectively. For this latter approach, the nitrogen rate is fixed at 10.5%. Both layers were submitted to classical annealing at 750ºC during one hour under a pure nitrogen flow.

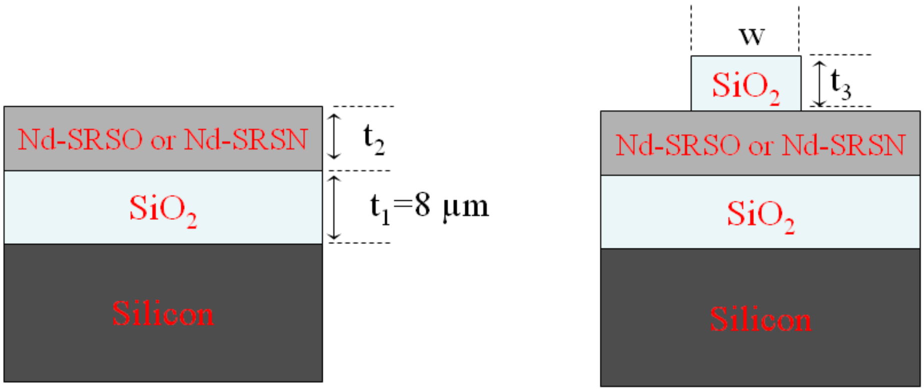

Figure 5.1: Schematic representations of (a) planar waveguide and (b) rib loaded waveguide.

In order to realize a rib loaded waveguide, a design was performed by our project partners (Fig. 5.1). According to this design Si wafers on which an 8 µm-thick cladding layer of thermal SiO_2 were used. The thickness of the cladding has been chosen to ensure an optical confinement in the guiding layer and thus to limit evanescent losses in the substrate. Guiding layers of Nd-SRSO or Nd-SRSN were grown on this thermal SiO_2 layer with a suitable thickness according to the calculation of TE and TM modes dispersion as a function of thickness displayed in figure 5.2. As seen, the Nd-SRSO layer should be thinner than about 1.3 µm to obtain single-mode waveguide, while for Nd-SRSN the thickness of the active layer does not exceed 0.41 µm. Thus, our studied waveguide has 1.1 µm thickness for Nd-SRSO layer or 0.38 µm for Nd-SRSN layer. On top of the guiding layer, a rib of SiO_2 was processed in order to ensure the lateral confinement of the modes. Taking into account the factor of merit (FOM) defined by ratio between the confinement factor Γ and the effective area of the fundamental mode, the thickness of this SiO_2 top layer has been fixed to 0.8 µm to obtain the best lateral light confinement (Fig. 5.3). Moreover, the width of SiO_2 rib can be chosen as 1, 2, 3, 4, 6, or 50 µm, while a 250 µm distance separates each rib loaded waveguide to ensure proper mode isolation.

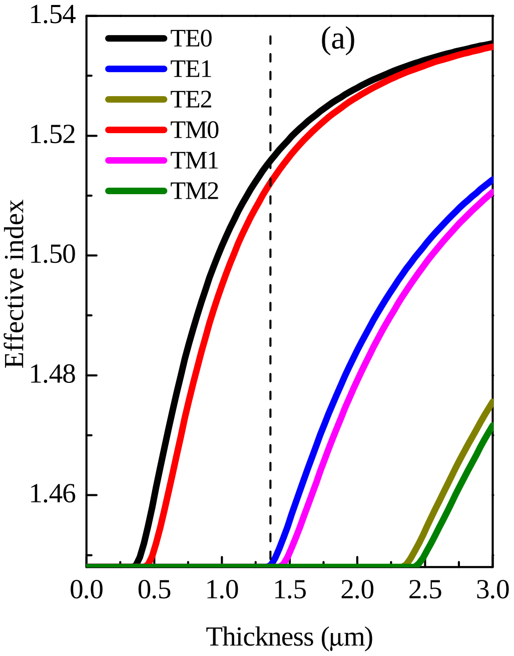

Figure 5.2: Dispersion of modes as a function of the thickness of (a) Nd-SRSO and (b) Nd-SRSN guiding layers for TE and TM polarization at 1064 nm.

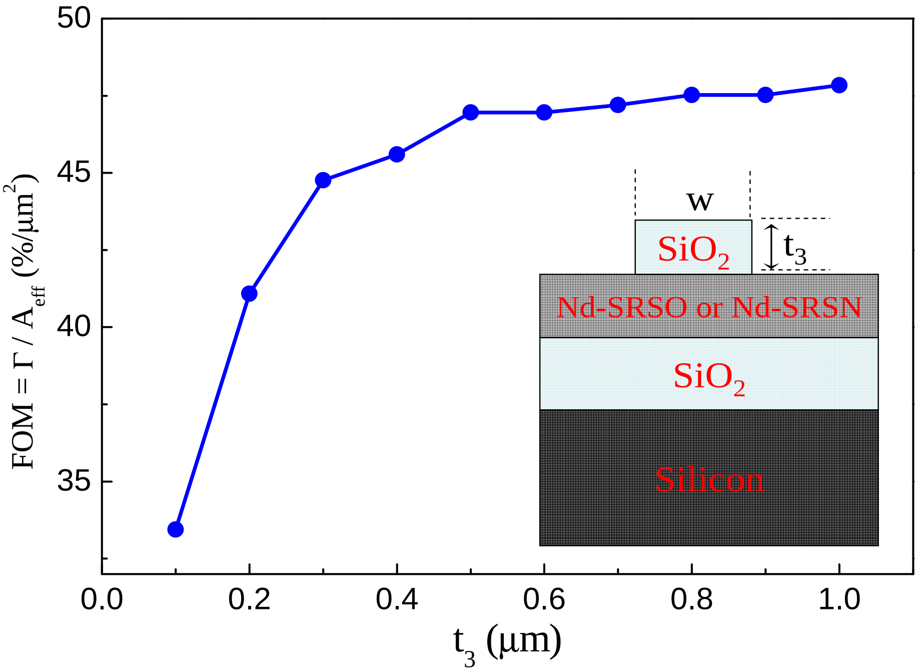

Figure 5.3: Evolution of factor of merit (FOM) as a function of the SiO_2 rib layer thickness t_3 shown in the inset.

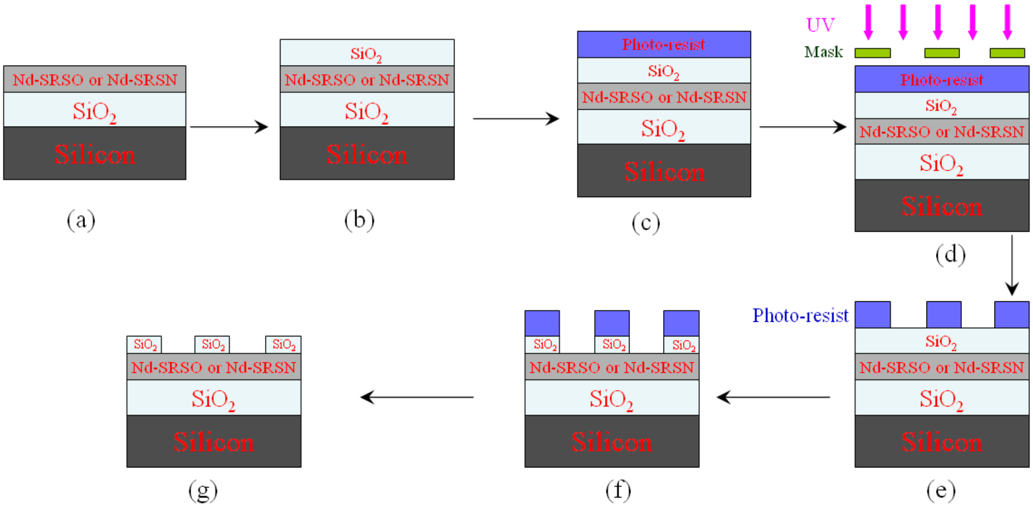

Figure 5.4: Schematic diagrams describing the different steps required for fabricating the rib waveguide.

To achieve a rib waveguide, a standard photolithography and reactive ion etching processes were employed. The detailed processes of such a device fabrication are schematized in figure 5.4. A SiO_2 layer with 0.8 μm thickness was deposited onto the guiding layer. From figure 5.4(b) to (c), the photo-resist was coated on top of surface. In figure 5.4(d), the sample was partially exposed to ultraviolet light (UV) through a mask containing a pattern in which the widths were equal to 1, 2, 3, 4, 6, or 50 μm, each rib being distant each other by 250 μm. The photo-resist was developed and the irradiative area was washed away (Fig.5.4(e)). The sample structure in figure 5.4(f) was obtained via a process of reactive ion etching. As seen, the SiO_2 covered by photo-resist remains, while the SiO_2 without resist cover was etched away. It should be noted that, this etching process does not increase the interface roughness. Finally, the rib waveguide (Fig. 5.4(g)) was achieved by stripping the residual photo-resist.

5.3 Optical properties

5.3.1 Optical losses

Optical losses were measured by studying the scattering light out-coupled from the surface of the waveguide. The laser light was coupled into the waveguide by means of micro-lens optical fiber. The intensity of the scattering light was recorded with a digital camera placed above the sample. Transverse scanning along the light propagation direction obtained by integrating the data along each sampling transverse line enabled the 2-D light intensity distribution of the guide modes to be obtained. The light intensity decreased exponentially with the z-propagation distance and was observed at different wavelengths: 1064, 1310, 1340, and 1550 nm for both planar and rib waveguides. To compare, both undoped and Nd-doped films used as guiding layer are concerned. The results are reported in Table 5.1. As seen, all the obtained values of optical losses are quite lower than 1 dB.cm^{-1} regardless of the wavelength. At each wavelength, there is no significant difference of optical losses between undoped and Nd-doped waveguides for either oxide or nitride host matrices. The losses for rib waveguides are slightly higher than those of planar ones probably due to the presence of side walls.

Waveguide type	Guiding layer	1064 nm	1310 nm	1340 nm	1550 nm
Planar waveguides (dB.cm^{-1})	SRSO	0.8±0.2	0.5±0.2	0.5±0.2	0.4±0.2
	Nd-SRSO	0.8±0.2	0.5±0.2	0.4±0.2	0.5±0.2
	SRSN	0.8±0.2	0.5±0.2	0.5±0.2	0.4±0.2
	Nd-SRSN	0.8±0.2	0.5±0.2	0.5±0.2	0.4±0.2
Rib waveguides (dB.cm^{-1})	SRSO	---	---	0.9±0.4	1.2±0.2
	Nd-SRSO	---	---	0.9±0.3	1.0±0.2

Table 5.1 Optical losses values (dB.cm^{-1}) as a function of the wavelength for undoped and Nd-doped planar waveguides and rib waveguides.

5.3.2 Guided photoluminescence

The guided PL measurements on Nd-SRSO and Nd-SRSN planar waveguides were performed at room temperature using an argon laser operating at 488 nm. First, the alignment is optimized between sample, objective and spectrometer by fiber-coupling laser light at 1.06 μm into the waveguide. The guided fluorescence achieved by top surface pumping is studied as a function of the pump power and as well as a function of the distance z between the excitation area and the output of the waveguide (Fig.5.5(a)).

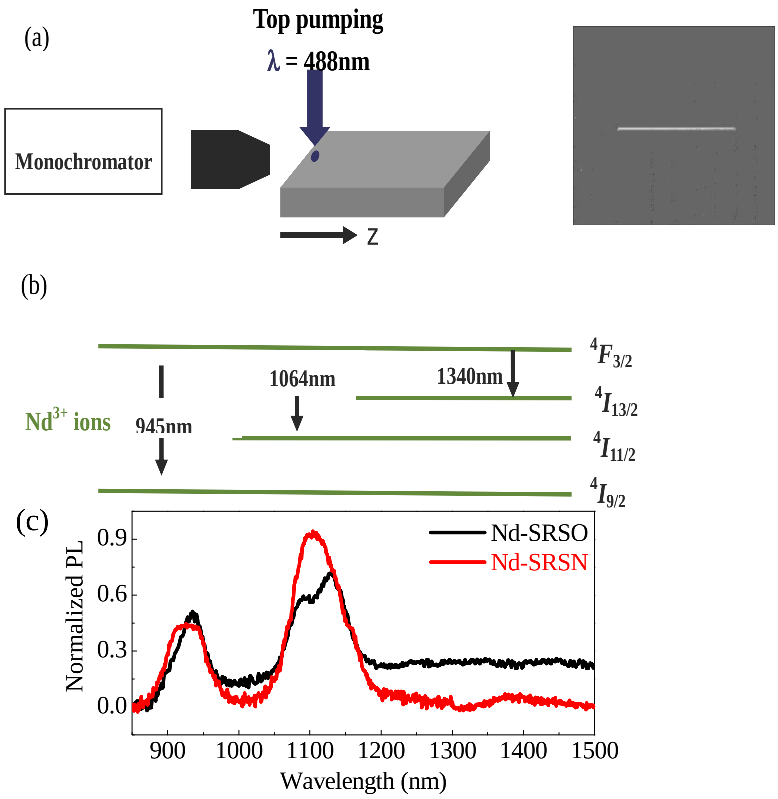

Figure 5.5: (a) Schematic representation of the top surface pumping at 488 nm and near-field of guided PL at the output of planar optical waveguide, (b) energy levels for Nd^{3+} *ion radiative transitions, (c) comparison of guide PL spectra for Nd-SRSO and Nd-SRSN planar waveguides obtained by top-pumping.*

Figure 5.5(c) represents the normalized guided PL spectra of Nd-SRSO and Nd-SRSN for a pump power equal to 150 mW (3.3×10^{19} photons.$cm^{-2}.s^{-1}$) at room temperature. Spectra reveal two principal bands centered about 920 and 1100 nm corresponding to $^4F_{3/2}$–$^4I_{9/2}$ and $^4F_{3/2}$-$^4I_{11/2}$ radiative transitions of Nd^{3+} ions. The presence of the guided PL of Nd^{3+} excited by a non-resonant excitation at 488 nm confirms the efficient sensitization of matrix host towards rare earth ions. The band corresponding to $^4F_{3/2}$-$^4I_{13/2}$ radiative transitions of Nd^{3+} ions is only detectable in the case of Nd-SRSN waveguide, shifted with respect to the 1340 nm. Such a week emission may be explained by a small branching ratio of this transition in both matrices and in the case of Nd-SRSO waveguide the emission of this band may be lower than our detection threshold level (Fig. 5.5(c)).

Moreover, the two spectrum shapes are not identical between Nd-SRSO and Nd-SRSN waveguides. For the oxide active layer, the guided PL reveals a broad band centered at 1100 nm that contains two peaks at 1090 and 1126 nm. Taking into account the geometry of our waveguides these two peaks are only attributed to the contribution of the active layer. This is confirmed by measurements performed on an undoped SRSO planar waveguides fabricated in the same conditions for which no guided PL has been evidenced. So, we can affirm that the guided PL is coming from the active guiding layer and not from the Si substrate. Furthermore, the SiO_2 cladding layer is an 8 μm thick layer which avoids any radiative modes due to an emission from the Si substrate towards the guiding layer. In the case of Nd-SRSN waveguides, a broad band containing a single peak centered at about 1104 nm is observed.

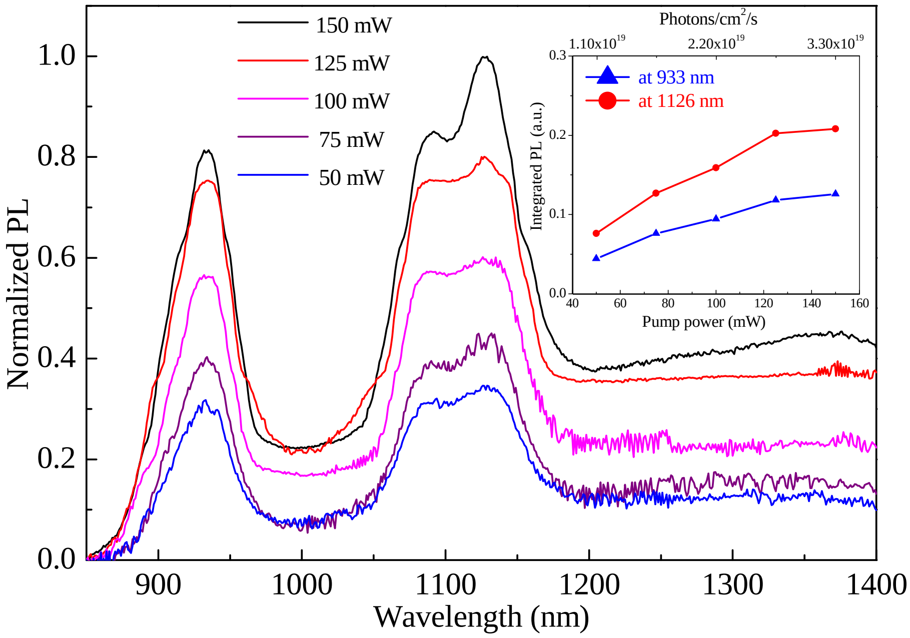

Figure 5.6: (a) Evolution of guided PL spectra obtained by top surface pumping, for different values of the pump power on Nd-SRSO planar waveguides. In the inset: integrated PL for the two emissions corresponding to $^4F_{3/2}$*-*$^4I_{9/2}$ *(850-1000 nm) and* $^4F_{3/2}$*-*$^4I_{11/2}$ *(1000-1200 nm) radiative transitions versus pump power.*

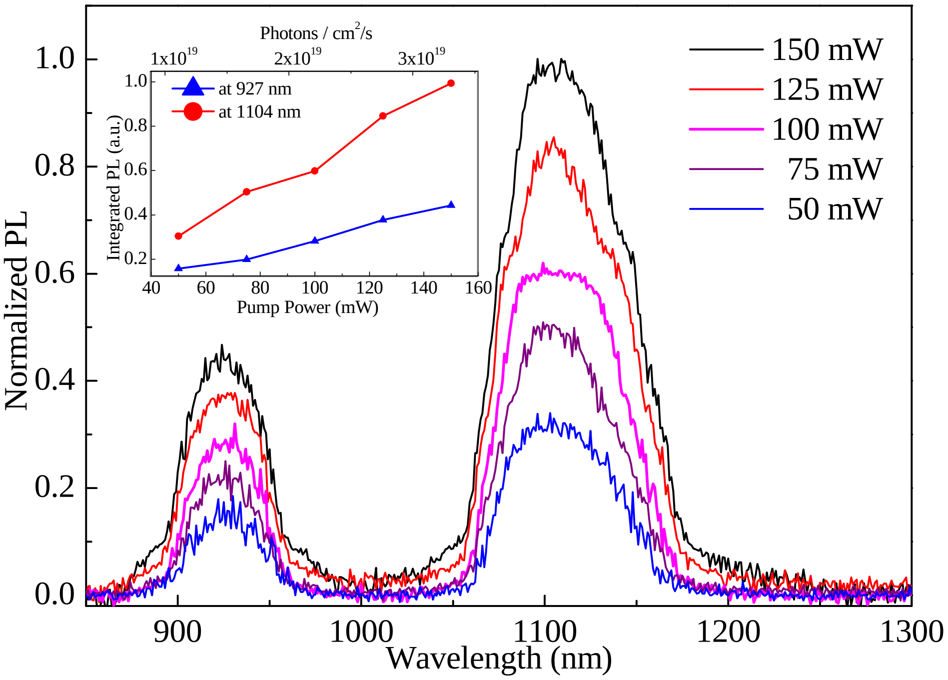

Figure 5.6: (b) Evolution of guided PL spectra obtained by top surface pumping for different values of the pump power on Nd-SRSN planar waveguides. In the inset: integrated PL for the two emissions corresponding to $^{4}F_{3/2}$-$^{4}I_{9/2}$ *(850-1000 nm) and* $^{4}F_{3/2}$-$^{4}I_{11/2}$ *(1000-1200 nm) radiative transitions versus pump power.*

Figures 5.6(a) and (b) respectively show the normalized spectra of guided PL for Nd-SRSO and Nd-SRSN planar waveguides recorded at room temperature and for different pump power (150 mW corresponds to 3.3×10^{19} photons.cm^{-2}.s^{-1}). The spectra have the same shape whatever the applied pump power and the PL intensity increases with excitation power. The insets of Figure 5.6(a) and (b) display the guided PL integrated intensity for the two Nd^{3+} emission peaks. The PL intensity increases linearly for low pump power and no saturation of the intensity has been observed at higher power for both waveguides. The linear increasing of the guided PL intensity of Nd^{3+} excited by a non-resonant excitation at 488 nm confirms the strong coupling between the Si-nps and/or defects and the Nd^{3+} ions in the two different host matrices[16] [17] [18]. It should be noted that the intensity of spectrum base line (from 1000 to 1400 nm) increases with pump power in the Nd-SRSO waveguide, while in the case of Nd-SRSN this stays at a low level whatever the pump powers. This could be attributed to some luminescence defects created during growth of Nd-SRSO film.

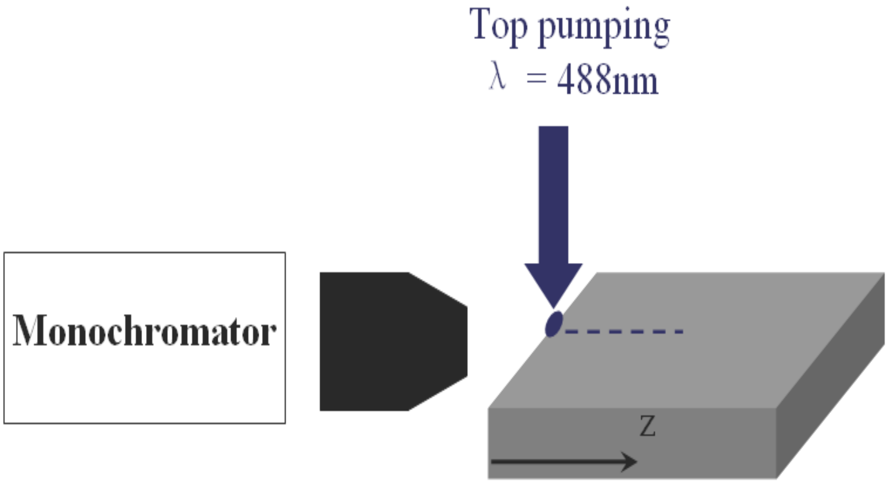

Figure 5.7: (a) Schematic representation of the top surface pumping at 488 nm.

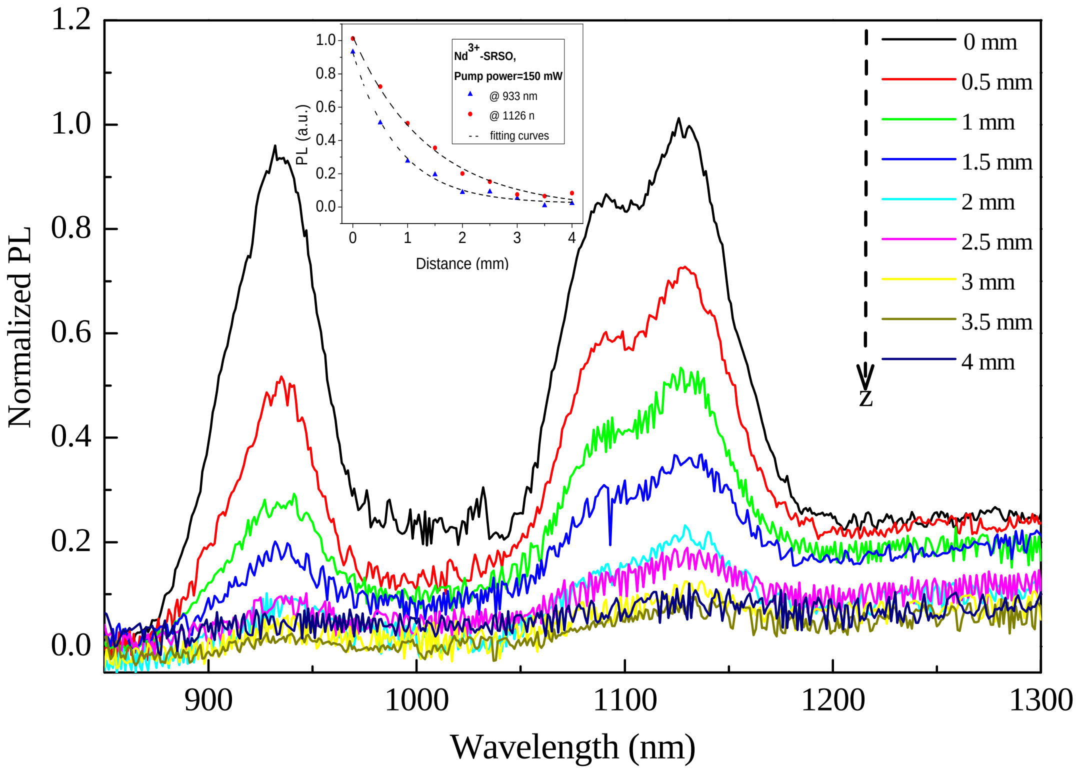

Figure 5.7(b) Evolution of guided PL spectra for different distances z which corresponds to the distance between the excitation area and the output of the waveguide for Nd-SRSO planar waveguides. In the inset: integrated PL versus distance z for the two emissions corresponding to $^4F_{3/2}$-$^4I_{9/2}$ *(850-1000 nm) and* $^4F_{3/2}$-$^4I_{11/2}$ *(1000-1200 nm) radiative transitions.*

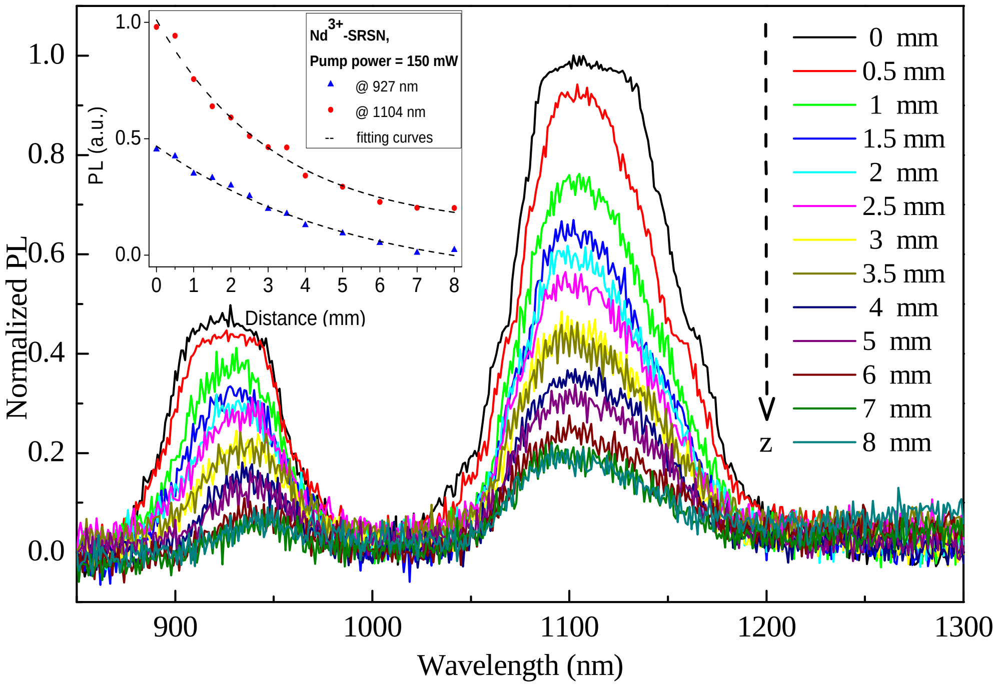

Figure 5.7: (c) Evolution of guided PL spectra for different distances z, which corresponds to the distance between the excitation area and the output of the waveguide for Nd-SRSN planar waveguides. In the inset: integrated PL versus distance z for the two emissions corresponding to $^4F_{3/2}$-$^4I_{9/2}$ *(850-1000 nm) and* $^4F_{3/2}$-$^4I_{11/2}$ *(1000-1200 nm) radiative transitions.*

Then, the guided fluorescence by top surface pumping at 488 nm (150 mW) on planar waveguides is studied as a function of the distance between the excitation area and the output of the waveguide (z) as shown in Figure 5.7(a). Figures 5.7 (b) and (c) represent the evolution of PL spectra (normalized to the thickness) according to the distance z for both waveguides. Guided PL at 945 and 1100 nm were observed until 4 mm from the output of the Nd-SRSO waveguide and until 8 mm from the output of the Nd-SRSN waveguide. As expected, the guided fluorescence at 945 and 1100 nm decreased when the excitation area moved away the output. This is attributed to the optical loss in the active layer as well as to the beam divergence in the planar waveguide. The larger propagation length observed for Nd-SRSN layer is attributed to a better light confinement in the guiding layer due to a higher refractive index contrast (see mode field profiles in Fig. 5.2). The positions of the peaks correspond to the typical transitions between internal energy levels in Nd^{3+} ions as described in figure 5.5(b). The related integrated intensities in the 850–1000 nm and 1000–1200 nm wavelength ranges are reported as a function of the distance in the insets of figure 5.7(b) and (c). The exponential decrease with the distance has been fitted leading to the attenuation values of 10.4 and 7.3 cm^{-1} at 945 and 1100 nm, respectively, in the case of the Nd-SRSO waveguide. For the nitride waveguide, the attenuation coefficients are at least two times lower with deduced values equal to 4.4 and 2.3 cm^{-1} at 945 and 1100 nm, respectively. These measurements allow us to believe that a better luminescence efficiency is obtained in the case of Nd-SRSN waveguides than in the case of Nd-SRSO ones. It is worth noticing that the attenuation value at 945 nm is higher than the one at 1100 nm, because of the re-absorption of the 945 nm radiation by the ground level.

The comparison of the two samples by measuring the guided PL is not straightforward. One of the reasons is the difference of thickness of the active layers for both matrices (1.1 µm for Nd-SRSO while it is of 0.380 µm for Nd-SRSN). The other concerns the difference of the excitation cross section of the Nd-SRSN and Nd-SRSO matrices. Consequently, lifetime measurements have been performed to determine their luminescence efficiency. The fluorescence decays of Nd-SRSO and Nd-SRSN planar waveguides were found to be 97 µs ±2 and 5 µs ±2, respectively. We notice that the lifetime in the nitride matrix is smaller than the one in SRSO attesting the presence of non-radiative defects.

With these measurements, we can notice a higher PL intensity of Nd-SRSN waveguides than Nd-SRSO ones. Indeed, the guided fluorescence by top surface pumping was observed for some more important length from the output in the case of Nd-SRSN waveguide. These measurements confirm that the spontaneous emission is encouraged in the Nd-SRSN matrix because of high PL intensity and a low lifetime, whereas the lower PL and a higher lifetime in the case of SRSO matrix should ensure to achieve a better stimulated emission.

5.3.3 Pump and probe measurements

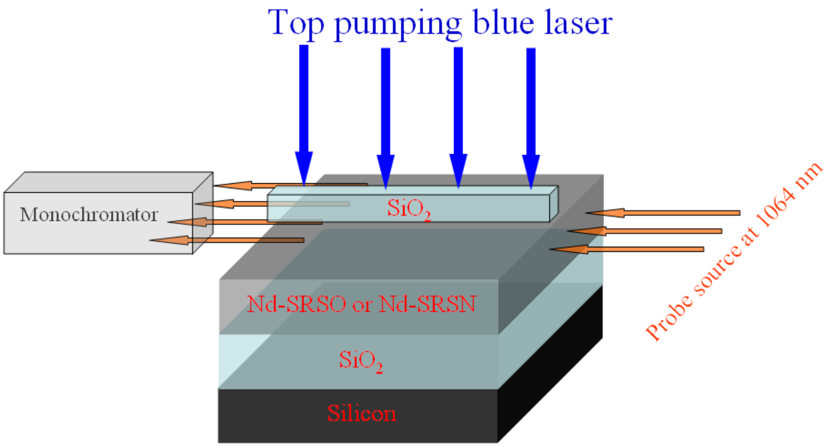

Figure 5.8: Schematic diagram of pump and probe measurements.

The pump and probe measurements, as shown in figure 5.8, have been performed on the rib-loaded waveguides. The pumping source is a modulated blue laser (443 nm) with an average power of 250 mW. The pumping light was focused by means of a cylindrical lens in normal incidence resulting in a pumping elliptic area of size 5×0.5 mm with major axis oriented along the waveguide’s rib. The probe source at 1064 nm, coming from a fiber laser, was chopped and injected into the waveguide. The output signal was focused by lenses on the monochromator entrance, the disperse signal on output of monochromator is detected with synchronous detection system locked to the chopper frequency of the signal. In this system the probe signal is continuously detected and the pump laser is periodically (every 1 minute) switched on and off.

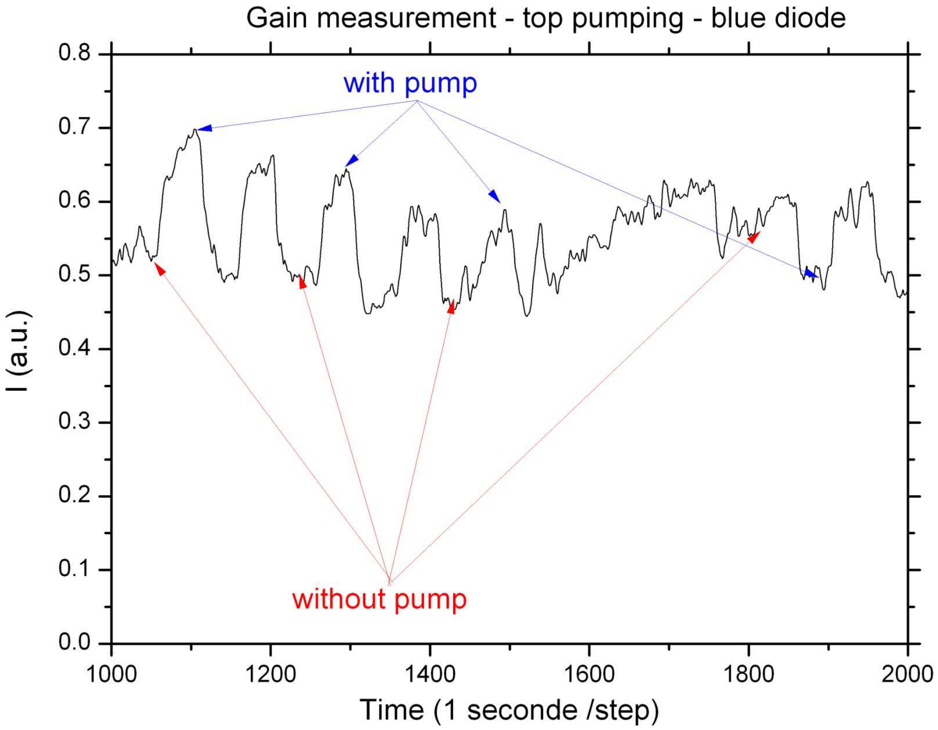

Figure 5.9: Measured signals for the pump and probe experiments of Nd-SRSO waveguide.

The measured signal is displayed in figure 5.9 for the Nd-SRSO waveguide. Before 1600 seconds during measurement, one can observe an increase of PL intensity by about 40% when the pump is with respect to the PL intensity without pumping. Let us consider the signal enhancement (SE) as the ratio of intensities with and without pumping[19]. Thus, one can obtain this SE value as high as 1.4. Such value is higher than the one reported for Er^{3+} system by Daldosso et al.[19]. This is mainly due to the advantage of using the Nd^{3+} ions in a four-level electronic configuration. Furthermore, using the SE value, one can roughly estimate the net gain (g) via the below relation[19]:

$$SE = \exp(gL), \tag{5.1}$$

where the L is the pumping waveguide length equal to 0.5 cm. Thus the g value is about 0.68 cm^{-1} (2.95 $dB.cm^{-1}$) achieved.

After 1600 seconds, we notice an inversion of the curves with an achieved PL intensity with pumping lower than those without pumping. Such a behavior is not clearly explained at this time, but could be the result of some laser thermal effect increasing with measurement time.

In the case of Nd-SRSN waveguide, we did not observe any variation of PL intensity between pumping on and off (data not shown). In other words, the SE value was found constant and equal to 1. It is possibly explained by the low lifetime of Nd^{3+} emission attesting of the presence of numerous non-radiative deexcitation paths.

5.4 Conclusion

We have studied the optical properties of waveguides made of Nd-SRSO or Nd-SRSN materials. Both waveguides have low optical losses of less than 1 $dB.cm^{-1}$ at 1064 nm. It is worth to note that no additional optical loss has been measured at 1064 nm originating from the spectroscopic properties of Nd^{3+} ion (four-level system). Top surface pumping experiments at 488 nm on planar waveguides have evidenced guided PL in both doped matrices. The PL signals at 945 and 1100 nm were observed until 4 mm (Nd-SRSO) and 8 mm (Nd-SRSN) from the excitation area. We have noticed that the PL intensity increases linearly with pumping powers with no saturation in the range of applied powers. The nitride waveguide possesses higher emission intensity than the oxide one. Finally, the pump and probe measurements showed a significant signal enhancement obtained from Nd-SRSO waveguide pumped by blue laser, while no enhancement was observed for Nd-SRSN waveguide. It results in a significant net gain of 0.68 cm^{-1} (2.95 $dB.cm^{-1}$) achieved for oxide waveguide.

As a consequence, the realization of these waveguide devices with notable guided PL and signal enhancement at room temperature opens the route towards the fabrication of 1064 nm laser based on Nd-doped Si-based materials. It represents a further step towards the realization of silicon microphotonics devices.

Bibliography

---

[1] W. J. Miniscalco, J. Lightwave Technol. **9** (1991) 234

[2] G. Rickman and G. T. Reed, IEEE Proc. optoelectron. **141** (1994) 391

[3] E. Desurvire, Phys. Today **47** (1994) 20

[4] P. Kik and A. Polman, Mater. Res. Bull. **23**, (1998) 48–54

[5] O. Debieu, D. Bréard, A. Podhorodecki, G. Zatryb, J. Misiewicz, C. Labbé, J. Cardin, F. Gourbilleau, J. Appl. Phys. **108** (2010) 113114

[6] A. J. Kenyon, C. E. Chryssou, C. W. Pitt, T. Shimizu-Iwayama, D. E. Hole, N. Sharma, C. J. Humphreys, J. Appl. Phys. **91** (2002) 367

[7] H. S. Han, S. Y. Seo, J. H. Shin, Appl. Phys. Lett. **79** (2001) 4568

[8] P. G. Kik and A. Polman, J. Appl. Phys. **91** (2002) 534

[9] P. Pellegrino, B. Garrido, J. Arbiol, C. Garcia, Y. Lebour, J. R. Morante, Appl. Phys. Lett. **88** (2006) 121915

[10] S. Y. Seo, M. J. Kim, J. H. Shin, Appl. Phys. Lett. **83** (2003) 2778

[11] J. S. Chang, I. Y. Kim, G. Y. Sung, J. H. Shin, Opt. express **19** (2011) 8406

[12] S. L. Oliveira, D. F. de Sousa, A. A. Andrade, L. A. O. Nunes, T. Catunda, J. Appl. Phys. **103** (2008) 023103

[13] D. Navarro-Urrios, A. Pitanti, N. Daldosso, F. Gourbilleau, L. Khomenkova, R. Rizk, L. Pavesi, Physica E **41** (2009)1029

[14] P. Pirasteh, J. Charrier, Y. Dumeige, Y. G. Boucher, O. Debieu, F. Gourbilleau, Thin Solid Films **520** (2012) 4026

[15] P. Pirasteh, J. Charrier, Y. Dumeige, J. L. Doualan, P. Camy, O. Debieu, C. L. Liang, L. Khomenkova, J. Lemaitre, Y. G. Boucher, F. Gourbilleau, J. Appl. Phys. **114**, 014906 (2013)

[16] C.-H. Liang, J. Cardin, C. Labbé, and F. Gourbilleau, J. Appl. Phys. **114** (2013) 033103

[17] E. Steveler, H. Rinnert, X. Devaux, M. Dossot, M. Vergnat, Appl. Phys. Lett. **97** (2010) 221902

[18] S. Yerci, R. Li, S. O. Kucheyev, T. van Buuren, S. N. Basu, L. Dal Negro, Appl. Phys. Lett. **95** (2009) 031107

[19] N. Daldosso, D. Navarro-Urrios, M. Melchiorri, C. Garcia, P. Pellegrino, B. Garrido, C. Sada, G. Battaglin, F. Gourbilleau, R. Rizk, L. Pavesi, IEEE J. Sel. Topics Quantum Electron. **12** (2006)1067

Summary and future perspectives

(a) Summary

The objective of this thesis concerns the fabrication of a compact and low cost planar laser, which is compatible with CMOS technology. In particular we have studied two different systems, Nd-SRSO and Nd-SRSN.

First of all we have investigated the Nd-SRSO films deposited by reactive co-sputtering or classical co-sputtering. Both approaches are favorable to achieve an intense Nd^{3+} emission. To optimize this emission, we have engineered the films compositions via tuning the deposition parameters, for example, power densities of Si and Nd_2O_3 targets. The optimal film was achieved with 4.7 at.% Si excess (from FTIR measurement) and 5.0×10^{19} at.cm^{-3} Nd content (from RBS experiment). This film was separately submitted to two annealing approaches, rapid thermal annealing (RTA) and classical annealing (CA). For the former approach, remarkable visible emission has been observed from T_A< 1000ºC annealed films due to some recombination occurring from radiative defect states, while at T_A>1000ºC, the visible emission mechanism is attributed to radiative recombination in Si-nps. We have demonstrated that the Nd^{3+} ions can be effectively sensitized by both these defect states and Si-nps. For the CA approach, the defects emission was quenched for T_A< 1000ºC annealed films while higher temperatures arrow Si-nps luminescence. We have shown that there are Si-nps which play their sensitizing role towards the Nd^{3+} ions for all the involved T_A layers, since the Nd^{3+} PL was noticed in both low and high T_A annealed layers under a 488 nm non-resonant excitation. A remarkable intensity enhancement has been recorded for both visible emissions (from defects or Si-nps) and infrared peaks (from Nd^{3+} ions) under forming gas annealing. This provides a promising way to optimize the luminescence intensity. Finally, the optimal layer from PL intensity point of view was used to fabricate a waveguide structure. The obtained device has less optical losses than those produced similarly in the case of the Er ions and notable guided PL has been observed. It is interesting to note that significant signal enhancement, proving the existence of a net gain, was observed in the pump and probe measurements. These results show that Nd-SRSO film is a very promising gain media on the way to achieve a laser cavity.

For Nd-SRSN films, we have only focused the work on the reactive co-sputtering approach using Si and Nd_2O_3 targets under Ar+N_2 plasma since, no Nd^{3+} emission was observed from the layers deposited by classical co-sputtering. The films compositions have been optimized by adjusting the nitrogen gas ratio and Nd_2O_3 target power density. It was found that the maximum Nd^{3+} PL corresponding to the layer containing a Si excess of 13.5 at.% (from FTIR measurement) and a Nd content of 5.0×10^{20} at.cm^{-3} (from RBS experiment), which are both much higher than the concentration achieved in the case of the oxide matrix. After either RTA or CA processes, the film shows an intense Nd^{3+} emission which increases with T_A. This results in a broad band of maximum PL intensity in 750-1000ºC range before slightly decreasing for higher T_A. This optimal T_A range is wider than in the case of Nd-SRSO film that can be attributed to a less diffusivity of atoms driven by annealing in nitride material. This allows to achieve a Nd^{3+} PL intensity three times higher in the nitride layer than in the oxide one. Additionally, we did not observe any emission improvement under forming gas annealing in contrast to pure nitrogen gas. This is another difference to the oxide matrix. For the Nd-SRSN waveguide, optical losses are low and comparable to Nd-SRSO device. The guide PL is high and has a longer propagation length than the oxide one due to a higher index contrast with a better light confinement in nitride layer. However, one did not achieve any signal enhancement in the pump and probe experiments, ascribing to a fast decay time of Nd^{3+} PL in the nitride matrix and/or thin thickness (0.38 μm) of the corn layer. These results confirm that spontaneous emission is encouraged in the Nd-SRSN sample.

(b) Future perspectives

This thesis is focused on the understanding of growth, composition, microstructure, and optical properties for Si-based materials. We have demonstrated the achievement of an intense Nd emission and at the end of this work, the existence of a net gain which is not stable over time. To understand the origin of such a behavior, further fabrication of waveguides and pump&probe experiments have to be carried out to demonstrate the feasibility of a future Si-based laser. This would require an optimization of the sensitizer:Nd ions coupling rate through the difficult photoluminescence experiment allowing the determination of the number of optically active Nd^{3+} ions. The possibility of incorporating a higher Nd content in the nitride matrix is a promising result that has to be deeply analyzed in terms of microstructure to understand the difference with the oxide matrix. Such a work will give important information on the detrimental problem of the Nd clusterization and will allow to consider new structure to avoid it. This is the way for achieving an improved device containing optimal Nd active ions coupled to sensitizers.

Propriétés optiques des films minces à base de Si dopé Nd : vers un amplificateur optique

Résumé:

Cette thèse décrit le développement et l'étude de matériaux à base silicium (Si) dédiés à des applications en photonique comme l'amplification optique ou le laser. Des matrices de SiO_2 et de Si_3N_4 enrichies en Si contenant des ions de terre rare Nd^{3+} ont été étudiées. Dans ces matrices, les ions Nd^{3+} bénéficient d'un transfert d'énergie de défauts ou/et de nanoparticules de Si présents dans la matrice hôte. Cela permet une excitation indirecte et efficace des ions Nd^{3+} sur une large bande spectral UV-VIS. Ainsi, une émission remarquable des ions Nd^{3+} à 920, 1064, and 1300 nm a été obtenue. Dans le but de développer la couche guidante active d'un guide d'ondes à partir des deux matrices et en choisissant comme figure de mérite l'émission des ions Nd^{3+}, l'optimisation de couches dopées Nd a été menée. La composition a été modifiée en termes d'excès de Si et de taux de Nd par la technique de pulvérisation magnétron. Les deux matrices ont été recuites par un traitement thermique classique ou rapide afin de modifier la microstructure de celles-ci. L'étude des facteurs influençant les mécanismes d'émission et de sensibilisation des ions Nd^{3+} a été réalisées. Dans la matrice de SiO_2 enrichie en Si, plusieurs sensibilisateurs des ions Nd^{3+}, à base de Si, ont été identifiés. Pour la matrice de Si_3N_4 enrichie en Si, un mécanisme d'excitation des ions Nd^{3+} dépendant de l'excès de Si a été mis en évidence. Finalement, un guide d'onde à base de SiO_2 enrichie en Si dopé Nd^{3+} a montré un gain net significatif de 0,68 cm^{-1} (2,95 $dB.cm^{-1}$) à 1064 nm.

Mots clefs: Pulvérisation, Recuit thermique rapide, Nanoparticules, Couches minces, Photoluminescence, Silicium, Néodyme, Guide d'ondes

Optical properties of Nd-doped Si-based thin films : towards an optical amplifier

Abstract:

This thesis focuses on the development and the study of Si-based materials dedicated to silicon photonics applications such as optical amplifier or laser. Si-rich SiO_2 and Si-rich Si_3N_4 matrices containing Nd^{3+} rare earth ions were studied. In such matrices, Nd^{3+} ions benefit from energy transfer from defects states and/or Silicon nanoparticles present in the host resulting in an efficient indirect excitation of Nd^{3+} on a broad UV-VIS spectral range. Thus, remarkable emissions of Nd^{3+} ions at 920, 1064, and 1300 nm have been observed. In order to develop the waveguide active guiding layer from the two matrices and taking the Nd^{3+} ions emission as a figure of merit, the optimization of the Nd-doped layers was carried out. The composition was engineered in terms of Si excess and Nd content by magnetron sputtering methods. Both matrices were annealed by classical or rapid thermal annealing processes in order to tune the layers' microstructures. Investigations of factors influencing the Nd^{3+} ions emission and sensitization mechanisms have been carried out in both matrices. In Si-rich SiO_2, several kinds of Si-based sensitizers towards the Nd^{3+} ions have been evidenced. While in Si-rich Si_3N_4 an excitation mechanism of Nd^{3+} ions dependent on silicon excess has been shown. Finally, waveguide based on Si-rich SiO_2:Nd^{3+} layer has shown a significant net gain of 0.68 cm^{-1} (2.95 $dB.cm^{-1}$) at 1064 nm.

Keywords: Sputtering, Rapid thermal processing, Nanoparticles, Thin films, Photoluminescence, Silicon, Neodymium, Waveguide